Eulerian multi-fluid models : modeling and numerical methods

Marc Massot[a,*],
email: marc.massot@em2c.ecp.fr

Stéphane de Chaisemartin[a,c],
email: stephane.de_chaisemartin@em2c.ecp.fr

Lucie Fréret[a,d],
email: lucie.freret@em2c.ecp.fr

Damien Kah[a,b],
email: damien.kah@em2c.ecp.fr

Frédérique Laurent[a]
email: frederique.laurent@em2c.ecp.fr

[a] Laboratoire EM2C - CNRS UPR 288, Ecole Centrale Paris, France

[b] Institut Français du Pétrole, 1 et 4 avenue de Bois Préau 92852 Rueil Malmaison, France

[c] present address : Institut Français du Pétrole,
1 et 4 avenue de Bois Préau 92852 Rueil Malmaison, France,
stephane.de-chaisemartin@ifp.fr

[d] present address : Laboratoire LIP - CNRS UMR 7623,
Université Pierre et Marie Curie, Paris, France, lucie.freret@umpc.fr

[*] corresponding author

August 19, 2009

Contents

1 Abstract

In this contribution we propose a general presentation of Eulerian multi-fluid modeling and numerical methods for the simulation of polydisperse evaporating sprays. By spray, we denote a cloud of spherical liquid droplets of various sizes ranging from submicronic scales up to several hundred microns which interact with the carrier gaseous phase and among themselves. We deal with sprays for which the physics of such a two-phase flow is governed at the "kinetic" level, also called mesoscopic level, by a Williams-Boltzmann spray equation, where the elementary phenomena such as evaporation, heating, coalescence and secondary break-up can be described properly. Our objective is to provide a hierarchy of models of Eulerian type with two main criteria : 1- to take into account accurately the polydispersion of the spray, that is the large size spectrum, as well as size-conditioned dynamics, evaporation and heating, 2- to keep a rigourous link with the Williams-Boltzmann spray equation at the mesoscopic level of description. We start with the original multi-fluid model where the polydispersion is resolved by discretizing the size phase space into intervals, also called sections in relation to the original work of Greenberg and Tambour. We present the fundamentals of the model, the associated precise set of related closure assumptions as well as its implication on the mathematical structure of solutions. We provide robust numerical methods able to cope with the potential presence of singularities and a set of validations showing the efficiency of the model and of the related numerical methods. This approach is very robust but encounters two difficulties : 1- in order to accurately resolve evaporation and size conditioned dynamics in phase space, it requires a high number of size intervals, 2- for finite Stokes numbers and large Knudsen numbers, it fails to reproduce droplet crossing trajectories since it relies on a hydrodynamic local velocity equilibrium. We thus present recent studies based on high order moment methods which allow to overcome these two difficulties. Then, the models are validated by comparisons with experimental measurements in the configuration of pulsated free jets with polydisperse spray injection, a dedicated well-controled environment with coupled Laser diagnostics. We conclude this lecture with a chapter on the computational multi-fluid dynamics and prove that the proposed models and related numerical methods and algorithms are well-suited for 2D and 3D simulations. They prove to be very accurate versus a Lagragian approach and eventually involve a small mount of numerical diffusion as a consequence of a precise choice of algorithms. Their ability for high performance computing on parallel architecture with dedicated algorithms is also demonstrated. In the framework of this Lecture Series, it provides a set of very interesting tools for the purpose of simulating nanoparticles in fluid flows.

2 Introduction

These Lecture Notes are devoted to the modeling and numerical methods used in the numerical simulation through Eulerian multi-fluid models of polydisperse evaporating sprays in gaseous flows. The main background application is two-phase combustion. Indeed, in many industrial combustion applications such as Diesel engines, fuel is stocked in condensed form, injected as a disperse liquid phase in a gaseous flow and burned once it has evaporated. Two phase effects as well as the polydisperse character of the droplet size distribution, since the droplets dynamics depend on their inertia and are conditioned on size, can significantly influence flame structure. Consequently, it is important to have reliable models and numerical methods in order to be able to describe precisely the physics of two-phase flows where the disperse liquid phase is constituted of a cloud of particles of various sizes that can evaporate, coalesce or aggregate, break-up and also have their own inertia and size-conditioned dynamics or heating properties.

Even if crucial in combustion applications, such a physics is also encountered in solid propel-

lant rocket boosters, where the cloud of alumina particles experiences coalescence and become polydisperse in size, thus determining its global dynamical behavior [1, 2]. The coupling of dynamics, conditioned on particle size, with coalescence or aggregation as well as with evaporation can also be found in the study of fluidized beds [3] and planet formation in solar nebulae [4, 5]. In fact such models and methods are also used for submicronic particles like aerosols (see [6] and references therein) and soots (see [7, 8]); in such cases, the particles only have a very small inertia, experience Brownian motion and usually satisfy a Population Balance Equation (PBE) for the particle size distribution describing various phenomena (aggregation, breakage, growth, oxidation...). In fact, we aim at describing the whole range of particle sizes from inertial to non-inertial particles, droplets or aerosols and nanoparticles as long as a "kinetic" description is available and reproduces reasonnably well the physics of the involved phenomenon. The purpose of these notes is to provide modeling and numerical tools for such scenarios. Since our main area of interest is combustion, we will work with sprays throughout this paper, keeping in mind the broad application fields related to this study.

By spray, we denote a disperse liquid phase constituted of droplets carried by a gaseous phase. Even with this seemingly precise definition, two approaches corresponding to two levels of description can be distinguished. The first, associated with a full direct numerical simulation of the process, provides a model for the dynamics of the interface between the gas and liquid, as well as the exchanges of heat and mass between the two phases using various techniques such as the Volume Of Fluids (VOF) or Level Set methods (see for example [9, 10, 11, 12]). This "microscopic" point of view is very rich in information on the detailed properties at one droplet level concerning, for example, the resulting drag exerted on one droplet depending on its surroundings flow or the details of one event of droplet break-up following the geometry of the interface between the phases. The second approach, based on a more global point of view thus called "mesoscopic", describes the droplets as a cloud of point particles for which the exchanges of mass, momentum and heat are described using a statistical point of view and the details of the interface behavior, angular momentum of droplets, detailed internal temperature distribution inside the droplet, etc., are not predicted. Instead, a finite set of global properties such as size of spherical droplets, velocity of the center of mass, temperature are modeled and denoted internal variables. Because it is the only one for which numerical simulations at the scale of a combustion chamber or in a free jet can be conducted, this "mesoscopic" point of view will be adopted in the present notes. The proposed methods will be valid as far as such a description is available.

The principal physical processes that must be accounted for are (1) transport in physical space, (2) droplet heating and evaporation, (3) acceleration of droplets due to drag, and (4) coalescence and break-up of droplets leading to polydispersity. Spray models, where a spray is understood as a disperse phase of liquid droplets, i.e. with a liquid volume fraction much smaller than one, have a common basis at the mesoscopic level (also called "the kinetic level" by analogy to the kinetic theory of gases), under the form of a number density function (NDF) satisfying a Boltzmann type equation, the so-called Williams-Boltzmann equation [13, 14]. This equation is also called the Population Balance Equation (PBE), Generalized Population Balance Equation (GPBE) or General Dynamic Equation (GDE) in the chemical engineering community [15, 16]. The Williams-Boltzmann equation implies several underlying assumptions, the major one being associated to the possibility of closing the equation in the "one-particle" probability density function (PDF) from the Liouville equation in the multi-particle joint PDF [17]. The reader who is not familiar with the kinetic theory of gases approach will find a precise adapted version to the present subject in [15]. The internal variables characterizing one droplet are size, velocity and temperature, so that the total phase space is usually high-dimensional. Such a transport equation describes the evolution of the NDF of the spray due to evaporation, to the drag force of the gaseous phase, to the heating of the droplets by the gas and finally to the droplet-droplet

interactions, such as coalescence and break-up phenomena [1, 18, 19, 20, 21, 22, 23]. The spray transport equation is then coupled to the gas phase equations. The two-way coupling of the phases occurs first in the spray transport equations through the rate of evaporation, drag force and heating rate, which are functions of the gas phase variables and second through exchange terms in the gas phase equations.

There are several strategies in order to solve the liquid phase and the major challenge in numerical simulations is to account for the strong coupling between all the involved processes. A first choice is to approximate the NDF by a sample of discrete numerical parcels of particles of various sizes through a Lagrangian–Monte-Carlo approach [1, 18, 19, 20, 24]. It is called Direct Simulation Monte-Carlo method (DSMC) by [25] and is generally considered to be the most accurate for solving Williams-Boltzmann equation; it is especially suited for Direct Numerical Simulations (DNS) since it does not introduce any numerical diffusion, the particle trajectories being exactly resolved. This approach has been widely used and has been shown to be efficient in a number of cases. Its main drawback, that has shown recently to be a major one with the development of new combustion chambers leading to combustion instabilities (Lean Premixed Prevaporized combustor with spray injection), is the coupling of a Eulerian description for the gaseous phase to a Lagrangian description of the disperse phase, thus offering limited possibilities of vectorization/parallelization and implicitation [26]. Besides, it brings another difficulty associated with the repartition of the evaporated mass at the droplet location onto the Eulerian grid for the gas description. Moreover for unsteady computations of polydisperse sprays, a large number of parcels in each cell of the computational domain is generally needed, thus yielding large memory requirement and computational cost.

This drawback makes the use of a Eulerian formulation for the description of the disperse phase attractive, at least as a complementary tool for Lagrangian solvers, and leads to the use of moments methods since the high dimension of the phase space prevents the use of DNS on the NDF equation with deterministic numerical methods like finite volumes or finite difference methods. The use of moments methods leads to the loss of some information but the cost of such methods is usually much lower than the Lagrangian ones for two reasons. The first one is related to the fact that the number of unknowns we solve for is limited; the second one is related to the high level of optimization one can reach when the two phases are both described by a Eulerian model. One of the key issue is then to chose a set of moments in order to capture the dynamics in the internal variables and a second one, related and not the easiest, is to close the set of equations in the model.

In the simple situation for which size is the only internal variable, there exists mainly two options. For submicronic particles like aerosols and soots the numerical solution of the PBE for the particle size distribution can be obtained by choosing a relevant set of global moments in size and by using a quadrature method of moments (QMOM in [27, 28]) or a direct quadrature method of moments (DQMOM in [29]), or other methods presented in the other Notes of this Lecture Series. This method is very efficient in the univariate case. The alternative is to discretize the size phase space into size interval called “sections” or “classes”, thus leading to a finite volume-like numerical method [30, 31] sometimes called a multi-fluid model. Let us underline that most of the time, we want to solve the evolution of the particle size distribution and the use of a presumed NDF approach encounters severe stability problems [**?**]. The reasons is that, for evaporating droplets or soots, the structure of the particle size distribution is strongly influenced by both the drift velocity in the size variable due to evaporation and growth/oxidation as well as by the aggregation-breakage phenomena and is far from being self-similar.

Thus, when we extend the set of internal variables and consider the multivariate case, we can either stick to a general moment method or particularize the size variable and consider a moment method conditioned on size for the other variables. In the context of inertial droplets,

for which the inertia determines the dynamical behavior, the first method was used in [32]. A set of global moments in both size and velocity was considered; however, the question of the choice of moments is still an open question and the multidimensional quadrature does not rely on firm mathematical grounds such as in the univariate case. The other possibility is to take moment methods in other internal variables conditioned on droplet size and then to use a multi-fluid approach, that is a discretization of the size phase space into intervals. As an example, for inertial droplets, let us consider the droplet size and velocity as the internal variables (the temperature and other variables lead to the same kind of reasonning). The question of choosing the velocity moments for a given size has been studied extensively in the kinetic theory literature [17, 33, 22, 23, 34], we refer to [35] for further reading and will come back to this issue. We thus divide the size phase space into intervals and use classical velocity moment methods and closures conditioned on each size interval. In the present notes, we choose the second approach and particularize the size variable.

A first attempt at deriving a fully Eulerian model for sprays polydisperse in size in laminar configurations with droplets having their own inertia and which was able to capture the dynamics of droplets with various size, whatever the profile of the NDF, was developed in [30] with the so-called sectional method. The idea was to consider the disperse phase as a set of continuous media : "fluids", each "fluid" corresponding to a statistical average in a size interval between two fixed droplet sizes, the section. The sprays were then described by a set of conservation equations for each "fluid". Greenberg in [30] noticed that such a model has also its origin at the kinetic level, trying to make the link with the Williams-Boltzmann spray equation. However, they only provided a partial justification, the complete derivation for the conservation of mass and number of droplets, the momentum and energy equations being out of the scope of their paper since the set of rigorous closure assumptions of the conservation equations was not provided. Finally, their coalescence model did not take into account the relative velocity of colliding particles, thus making the model only suited for very small particles like soots such as in [7].

The purpose of the present contribution is to present the class of methods called the Eulerian multi-fluid approach initiated in [23], which was inspired by the sectional approach and extended to coalescence in [36, 37], to break-up in [38, 39], to turbulent flows in [34, 40, 41] and to multi-dimensional configurations in [42, 43]. The basis idea behind such a class of models is to build a model meeting the following criteria : 1- Eulerian description of the disperse liquid phase, 2- preservation of the link with the kinetic level of description, 3- ability of capturing the polydispersion in size of evaporating sprays, 4- ability of capturing the dynamics of the evaporating droplets conditioned on size. The key ingredient in order to obtain such a model is to preserve the droplet size as an internal variable, but to use a moment approach as far as velocity and eventually temperature are concerned. For the sake of legibility, the derivation of the various level of modeling will be conducted within the framework of simplified droplet models, since it is straightforward to extend it to richer droplet modeling for which we provide precise references. Even if it is important for combustion application (see section 5), we will neglect the heating of the droplets and illustrate the proposed model in the case where the internal variables are only the size and the droplet velocity. We refer to the two Ph.D. Theses of F. Laurent, G. Dufour and S. de Chaisemartin where detailed models can be found [44, 39, 43].

The first model to meet the proposed criteria is the original multi-fluid model as developped in [44, 23]. The first Chapter of the Notes is devoted to this model. From the Williams-Boltzmann equation, we derive a semi-kinetic model, that is, we preserve the size as a continuous internal variable but introduce a velocity and eventually a temperature moment closure in order to obtain a set of partial differential equations. It is equivalent to the original Williams-Boltzmann equation under the assumption that there exists a single mean characteristic velocity for a given droplet size, at a given space location and for a given time, around which a generalized

Maxwellian velocity distribution is to be found thus leading to a possible closure of the set of equations. In the laminar case or in the framework of DNS, it corresponds to the so-called monokinetic velocity distribution, i.e. no dispersion around the mean, which is a generalization of the usual concept of Maxwellian distribution (a common assumption of zero temperature used in astrophysics [45] for example). Even if the whole droplet sizes range is covered, the support of the droplet number distribution in the velocity phase space is restricted to a one-dimensional sub-manifold of $\mathbb{R}^d$, parametrized by droplet size [23], d being the spatial dimension. We will successively present the semi-kinetic model for polydisperse dense evaporating sprays experiencing break-up and coalescence. However, we will not tackle the case of turbulent flows for which some scales are not resolved but modeled in these Notes; it corresponds to a usual Maxwellian distribution for which the dispersion becomes a variable of the problem : the droplet agitation "internal energy". We refer to [41] and references therein. The set of assumptions we have identified allows to relate the obtained model in the laminar case to the pressureless gas dynamics studied in [45, 46]. Consequently, the mathematical structure of the resulting conservation equations leads to identified singularities. The second section is devoted to an illustration of typical singularity formation and we characterize critical Stokes number associated with it. It will be very helpful in understanding the physics behind such mathematical behavior, as well as in designing optimal and robust numerical methods which can reproduce such singularities. From the knowledge of the semi-kinetic model and of its structural behavior, we design the numerical tools in order to simulate such a model in a third section. This semi-kinetic model is then discretized in the size variable using a finite volume-like technique [47]. It yields the multi-fluid model for which we can preserve some level of information about the size distribution with a reasonable and adaptive computational cost. If a good level of precision is required about the size distribution, the computational cost is going to be lower but comparable to the Lagrangian one (however the optimization of the solver through the fully Eulerian description of the two phases leads to a substantial gain in CPU time as presented in Chapter 6). The method is still able to capture the behavior of the spray with a coarse discretization in the size phase space [48] and thus a low computational cost, a definitive advantage in comparison with the Lagrangian methods. The question of the computational efficiency of such Eulerian approaches is a key question since these methods are intended to be used in more realistic unsteady configurations as an alternative to the too costly Lagrangian methods for polydisperse sprays. We have already studied this question in [37, 42, 43] where the Eulerian multi-fluid approach was shown to offer a good precision with a relative low cost. Finally the fourth section is devoted to the numerical illustration and validation of the multi-fluid model in several test-cases where the simulations are compared to Lagrangian simulations. Three representative configurations are chosen for the gaseous flow with one-way coupling in order to compare the results obtained by Lagrangian and Eulerian models for the spray : Taylor-Green vortices, two-dimensional axi-symmetric jets and coalescence in a conical nozzle. Two-dimensional Taylor-Green configuration is a very interesting benchmark which allows us to prove the computational efficiency and the good behavior of the multi-fluid for multi-dimensional configurations [42].

Starting from this fundamentals, we focus on the two main limitations of the original multi-fluid model. First, the method is based on a one mass-moment preservation in each section, which amounts to considering constant distribution functions in one section or size interval. Thus, in order to capture the details of the size distribution function as well as size conditioned dynamics and heating, we have to provide a large amount of sections as explained also in the coalescence case in the first chapter. Besides, the closure in velocity distribution conditioned on size is based on a one node quadrature, the monokinetic assumption, and is equivalent to a hydrodynamical equilibrium closure. However, in the context of an infinite Knudsen limit, that is, if the spray is dilute enough and the droplet small enough in such a way that collisions can

completely be neglected, two groups of droplets can cross and produce a multi-modal velocity distribution which can not be reproduced by the original assumption of the multi-fluid and leads to singularities as described in Chapter 1. Based on high order moment methods and related algebra tools we provide in a second chapter possibilities to overcome these two difficulties. This work is based on the ongoing work of D. Kah in his Thesis [49] and corresponds to several publications [50, 51**?** , 52]. We present a synthesis of these results and the related tools in Chapter 4.

The third Chapter is devoted to validations through comparisons with experimental measurements in the configuration of pulsated free jets with polydisperse spray injection, a dedicated well-controled environment with coupled diagnostics. This work has been the subject of a Symposium paper [53]. We have designed the experimental set-up and the related diagnostics in order to be able to capture the size conditioned-dynamics of a polydisperse spray in a laminar periodic unsteady gaseous flow with strong vortical structures. This is an ideal validation test-case for the methods we are developing and shows that we are able to reproduce numerically the physics of such flows for both non-evaporating and evaporating sprays.

Finally, once we have obtained the models and numerical methods and validated them, we demonstrate in a fourth chapter, that such models and methods are very accurate and well suited for parallel architectures in order to conduct 3D simulations. In the context of two configurations related to the work conducted in the 2008 Summer Program of the Center for Turbulence Research at Stanford University and to the thesis of S. de Chaisemartin, we propose detailed comparisons with Lagrangian simulations. These configurations are a 2D free jet and a 3D homogeneous tubulence; thus we show the ability of the Eulerian multi-fluid models to capture the details of the dynamics with a very limited amount of numerical diffusion as a result of a precise use of various algorithms and with a nice scalability on parallel architecture. It foresees the capability of such methods for more complex 3D configurations and justifies the choices we have made in terms of models, numerical methods and algorithms.

3 Multi-fluid fundamentals

3.1 Modeling Fundamentals in a simplified framework

For the purpose of the legibility of the paper, we will present the derivation of the Eulerian multi-fluid model for polydisperse evaporating sprays which experience coalescence and secondary break-up from a simplified Williams-Boltzmann equation at the kinetic level of description.

3.1.1 Williams-Boltzmann transport equation

Let us define the number distribution function $f^{a,b}$ of the spray, where $f^{a,b}(t,\mathbf{x},\phi,\mathbf{u})\,\mathrm{d}\mathbf{x}\,\mathrm{d}\phi\,\mathrm{d}\mathbf{u}$ denotes the averaged number of droplets (in a statistical sense), at time t, in a volume of size $\mathrm{d}\mathbf{x}$ around $\mathbf{x}$, with a velocity in a $\mathrm{d}\mathbf{u}$-neighborhood of $\mathbf{u}$ and with a size in a $\mathrm{d}\phi$-neighborhood of ϕ. The droplets are considered to be spherical and their sizes are characterized by $\phi = a\,r^b$, where r is the radius of the droplet; ϕ can be the radius ($a = 1$ and $b = 1$; $\phi = r$), the surface, ($a = 4\pi$ and $b = 2$; $\phi = s$) or the volume ($a = \frac{4}{3}\pi$ and $b = 3$; $\phi = v$). The associated evaporation rate will be denoted R_ϕ. We will work mainly with the volume and the surface in the following. Within this section, we will use the volume and $f^{\frac{4}{3}\pi,3}$ will be noted f.

For the sake of simplicity and for the purpose of this paper, we are going to consider that the evaporation process is described by a d^2 law without convective corrections, that the drag force is given by a Stokes law, and finally that the unstationary heating of the droplets does not need to be modeled so that the evaporation law coefficient does not depend on the heating status

of the droplet. This simplifications are only for the sake of clarity of the presentation have no consequences on the generality of the proposed approach. We refer to [54], [1] and [23] for more detailed droplet models for which the derivation can be easily extended and the reader will find the details in the three theses we have dedicated to the development of our model [44, 39, 43].

The evolution of the spray is then described by the Williams-Boltzmann transport equation :

$$\partial_t f + \mathbf{u}\cdot\partial_{\mathbf{x}} f + \partial_v(R_v\, f) + \partial_{\mathbf{u}}.(\mathbf{F}\, f) = \Gamma_{\text{coll}} + \Gamma_{\text{bu}}, \tag{1}$$

where $R_v(t,\mathbf{x},v,\mathbf{u})$ denotes the d^2 law evaporation rate $R_v = \frac{1}{2}\left(\frac{3v}{4\,\pi}\right)^{1/3} R_\phi$, where R_ϕ is a constant, $\mathbf{F}(t,\mathbf{x},v,\mathbf{u})$ is the Stokes drag force due to the velocity difference with the gaseous phase, $\mathbf{F} = \frac{\mathbf{U}_{gas}(t,\mathbf{x})-\mathbf{u}}{\tau_p}$, $\mathbf{U}_{gas}$ being the gaseous velocity and $\tau_p(s)$, the dynamical time of the droplet, $\tau_p(s) = \frac{\rho_l\, s}{18\,\pi\mu_{\text{gas}}}$, where ρ_l is the density of the liquid assumed constant and μ_{gas} the viscosity of the gas; Γ_{coll} is the collision operator leading to coalescence and Γ_{bu} the operator modeling the secondary break-up. These quantities have the following dependence $(t,\mathbf{x},\mathbf{u},v)$ (except for Γ_{coll} and Γ_{bu} which are integral operators depending on f); in general, they depend on the local gas composition, velocity and temperature and this dependence is implicitly written in the $(t,\mathbf{x})$ dependence.

It has to be noticed that the refinement of the drag, evaporation and heating models, can not go beyond a given limit in the context of a kinetic description. The added mass effect in the aerodynamical forces can be described only through the addition of a new variable in the phase space which is the time derivative of the velocity of the particle; in the applications we are considering, it is going to be negligible. Actually, the history terms such as the Basset forces or the inner temperature distribution of a droplet in the effective conductivity model by [54] can not be easily modeled in the context of a kinetic description of the spray, as already discussed in [23]. As a conclusion, the derivation presented in the following on a simplified model, can be extended to more refined droplet models as long as they do not include history terms.

3.1.2 Modeling of coalescence

The kinetic model for the collision operator leading to coalescence is taken from [55] and we neglect the influence of the impact parameter on the probability of rebound of two collisional partners :

[Co1] We only take into account binary collisions (small volume fraction of the liquid phase).

[Co2] The mean collision time is very small compared to the intercollision time.

[Co3] Every collision leads to coalescence of the partners.

[Co4] During coalescence, mass and momentum are conserved.

Thus $\Gamma_{\text{coll}} = Q^-_{\text{coll}} + Q^+_{\text{coll}}$, where Q^-_{coll} and Q^+_{coll} respectively correspond to the quadratic integral operators associated with creation and destruction of droplets due to coalescence :

$$Q^-_{\text{coll}} = -\int_{v^*}\int_{\mathbf{u}^*} f(t,\mathbf{x},v,\mathbf{u})\, f(t,\mathbf{x},v^*,\mathbf{u}^*)\, B(|\mathbf{u}-\mathbf{u}^*|,v,v^*)\,\mathrm{d}v^*\mathrm{d}\mathbf{u}^*, \tag{2}$$

$$Q^+_{\text{coll}} = \frac{1}{2}\int_{v^*\in[0,v]}\int_{\mathbf{u}^*} f(t,\mathbf{x},v^\diamond(v,v^*),\mathbf{u}^\diamond(v,v^*,\mathbf{u}))\, f(t,\mathbf{x},v^*,\mathbf{u}^*)\, B(|\mathbf{u}^\diamond-\mathbf{u}^*|,v^\diamond,v^*)\, J\,\mathrm{d}v^*\mathrm{d}\mathbf{u}^*, \tag{3}$$

where $v^\diamond$ and $\mathbf{u}^\diamond$ are the pre-collisional parameters, $v^\diamond(v,v^*)=v-v^*$ and J is the Jacobian of the transform $(v,\mathbf{u})\rightarrow(v^\diamond,\mathbf{u}^\diamond)$, at fixed $(v^*,\mathbf{u}^*)$: $J=(v/v^\diamond)^d$, with d the dimension of the velocity phase space ([1, 55]) and where $B(|\mathbf{u}-\mathbf{u}^*|,v,v^*)=\beta(v,v^*)\,|\mathbf{u}-\mathbf{u}^*|$ with

$$\beta(v,v^*)=\pi\left(r(v)+r(v^*)\right)^2, \qquad r(v)=\left(\frac{3v}{4\pi}\right)^{\frac{1}{3}} \qquad \mathbf{u}^\diamond=\frac{v\mathbf{u}-v^*\mathbf{u}^*}{v-v^*}, \tag{4}$$

where $v^\diamond$ and $\mathbf{u}^\diamond$ are the pre-collisional parameters, $v^\diamond(v,v^*)=v-v^*$ and J is the Jacobian of the transform $(v,\mathbf{u})\rightarrow(v^\diamond,\mathbf{u}^\diamond)$, at fixed $(v^*,\mathbf{u}^*)$: $J=(v/v^\diamond)^d$ ([1, 55]).

Remark 1. The assumption that all collisions lead to the coalescence of the partners is not realistic, especially if the colliding droplets have comparable sizes ([56] [57]). In such situations the probability E_{coal}, that coalescence really occurs from the collision of two droplets has to be taken into account; the expression of B then becomes $B(|\mathbf{u}-\mathbf{u}^*|,v,v^*)=E_{\text{coal}}(|\mathbf{u}-\mathbf{u}^*|,v,v^*)\,\beta(v,v^*)\,|\mathbf{u}-\mathbf{u}^*|$. It is possible to treat the coalescence efficiency factor within the proposed model and the reader is referred to [37] for the details. Nevertheless, in the following, for the sake of simplicity, we will assume $E_{\text{coal}}(|\mathbf{u}-\mathbf{u}^*|,v,v^*)=1$, which is equivalent to assumption [Co3].

3.1.3 Modeling of secondary break-up

Similarly the modeling of secondary break-up relies on a statistical approach and can be taken from [1, 39] :

$$\Gamma_{\text{bu}}(f)(v,\mathbf{u})=-\nu^{\text{bu}}f+\int_{v^*>v}\int_{\mathbf{u}}\nu^{\text{bu}}(v^*,\mathbf{u}^*)h(v,v^*,\mathbf{u},\mathbf{u}^*)f(v^*,\mathbf{u}^*)\mathrm{d}v^*\mathrm{d}\mathbf{u}^* \tag{5}$$

- ν^{bu} is the mean break-up frequency of the droplets which is defined through experimental correlations on the mean break-up time of a droplet from [58, 59]. Following [60] (a thorough discussion of this issue is to be found in [39]), for Weber numbers beyond the critical one, we take :

$$\nu^{\text{bu}}(v,\mathbf{u})=\frac{\|\mathbf{U}_{gas}-\mathbf{u}\|}{10\,r(v)}\sqrt{\frac{\rho_l}{\rho_{gas}}}, \tag{6}$$

  where ρ_{gas} is the density of the gas, but the mean break-up frequency can be also a function of both the Weber and the Ohnsorge numbers as in [59].

- $h(.,.,v^*,\mathbf{u}^*)$ denotes the daughter distribution in terms of size and velocity $(v^*,\mathbf{u}^*)$. This distribution must satisfy the mass conservation constraint :

$$\int_{\mathbf{u}}\int_{v=0}^{v^*}v\,h(v,\mathbf{u},v^*,\mathbf{u}^*)\mathrm{d}v\mathrm{d}\mathbf{u}=v^*, \tag{7}$$

  and must be further defined. We take $h(v,\mathbf{u},v^*,\mathbf{u}^*)=g_u(v,\mathbf{u},v^*,\mathbf{u}^*)g_v(v,v^*,\mathbf{u}^*)$, where $g_u(v,v^*,\mathbf{u},\mathbf{u}^*)=\delta(\mathbf{u}-\mathbf{u}^{\text{bu}}(v,v^*,\mathbf{u}^*))$, with

$$\mathbf{u}^{\text{bu}}(v,v^*,\mathbf{u}^*)=\mathbf{U}_{gas}+\frac{\mathbf{u}^*-\mathbf{U}_{gas}}{1+C_{We}\left(\sqrt{\frac{\rho_{gas}}{\rho_l}}\frac{r(v^*)}{r(v)}\right)^{2/3}} \tag{8}$$

  from [60] and $g_v(v,v^*,\mathbf{u}^*)$ is the droplet size distribution after break-up.

There is not a single and standard way of modeling the statistics of the daughter droplets; O'Rourke and Amsden in [61] for example take an exponantially decreasing function of droplet radius with the use of a correlation for the Sauter mean radius r_{smd} in terms of Weber number : the Wert correlation [62]. Since most of the time, for evaporation sprays, the number density function as a function of droplet radius linearly approaches zero at zero droplet radius, [39] rather introduced, using :

$$r_{\text{smd}} = \left(\frac{3}{4\pi}\right)^{1/3} \frac{\displaystyle\int_0^{v^*} v\, g_v \,\mathrm{d}v}{\displaystyle\int_0^{v^*} v^{2/3} g_v \,\mathrm{d}v}; \qquad (v^*)^3 = \int_0^{v^*} v^3 g_v \mathrm{d}v, \tag{9}$$

a profile of the droplet size distribution which he assumed exponentially descreasing as a function of droplet surface :

$$g_s(s, v^*, \mathbf{u}^*) = \frac{\eta}{8\,\pi} \exp\left(-\frac{\gamma}{4\,\pi}\, s\right), \quad g_s(s, v^*, \mathbf{u}^*)\mathrm{d}s = g_v(v, v^*, \mathbf{u}^*)\mathrm{d}v, \tag{10}$$

where the two functions $\eta(v^*, \mathbf{u}^*)$ and $\gamma(v^*, \mathbf{u}^*)$ are determined from the above equalities. The reader will find the details of the calculation of these two coefficients in [39].

3.1.4 Eulerian semi-kinetic model

In this section, we will recall the first step of the formalism and the associated assumptions introduced in [23] in order to derive the Eulerian multi-fluid method and explain how this formalism can be extended in order to treat the coalescence phenomenon between droplets having their own inertia governed by their size. It is worth noticing that we do take into account the mean velocity difference of the droplets in the coalescence process as opposed to the model proposed in [30] which is mainly suited for very small particles such as soots.

The key idea is to reduce the size of the phase space and to consider only the moments of order zero and one in the velocity variable at a given time, a given position and for a given droplet size. The obtained conservation equations, called the semi-kinetic model for the two fields $n(t, \mathbf{x}, v) = \int f \,\mathrm{d}\mathbf{u}$ and $\bar{\mathbf{u}}(t, \mathbf{x}, v) = \int f\, \mathbf{u}\, \mathrm{d}\mathbf{u} \,/ n(t, \mathbf{x}, v)$, are only in a close form under a precise assumption on the support of the original NDF in the whole phase space : the velocity distribution at a given time, given location and for a given droplet size is a Dirac delta function [23].

However, this assumption is not directly compatible with the coalescence phenomenon, since there is no reason for a droplet created by the coalescence of two droplets of various sizes, which is deduced from momentum conservation, to exactly match the velocity corresponding to its new size. We first relax the assumption of zero dispersion and assume Gaussian velocity dispersion and handle the whole positive real line for the possible sizes so that all the collisions can be described by the model : $(v, \mathbf{u}) \in (0, +\infty) \times \mathbb{R}^d$. The semi-kinetic system of conservation laws is then obtained by taking the limit of zero dispersion in the source terms coming from coalescence, uniformly in $(t, \mathbf{x}, v)$. Summarizing, we obtain the semi-kinetic model in the limit of zero dispersion of a more general problem where dispersion is allowed and "project" the original NDF at the kinetic level onto a one-dimensional sub-manifold of velocity phase space parametrized by droplet size [23].

Proposition 2. *Let us make the following assumptions on the spray distribution function:*

[H1] *For a given droplet size, at a given point $(t, \mathbf{x})$, there is only one characteristic averaged velocity $\bar{\mathbf{u}}(t, \mathbf{x}, v)$.*

[H2] *The velocity dispersion around the averaged velocity* $\bar{\mathbf{u}}(t,\mathbf{x},v)$ *is zero in each direction, whatever the point* $(t,\mathbf{x},v)$.

[H3] *The droplet number density* $n(t,\mathbf{x},v)$ *is exponentially decreasing at infinity as a function of* v *uniformly in* $(t,\mathbf{x})$.

Assumptions [H1] *and* [H2] *define the structure of* f *:* $f(t,\mathbf{x},v,\mathbf{u}) = n(t,\mathbf{x},v)\,\delta(\mathbf{u}-\bar{\mathbf{u}}(t,\mathbf{x},v))$ *and the semi-kinetic model is given by two partial differential equations in the variables* $n(t,\mathbf{x},v)$ *and* $\bar{\mathbf{u}}(t,\mathbf{x},v)$ *which express respectively, the conservation of the number density of droplets and their momentum, at a given location* $\mathbf{x}$ *and for a given size* v *:*

$$\partial_t n + \partial_{\mathbf{x}}\cdot(n\bar{\mathbf{u}}) + \partial_v(n\overline{R_v}) = \mathcal{G}^n_{\text{coll}} + \mathcal{G}^n_{\text{bu}} \tag{11}$$

$$\partial_t(n\,\bar{\mathbf{u}}) + \partial_{\mathbf{x}}\cdot(n\,\bar{\mathbf{u}}\otimes\bar{\mathbf{u}}) + \partial_v(n\,\overline{R_v}\bar{\mathbf{u}}) - n\overline{\mathbf{F}} = \mathcal{G}^{nu}_{\text{coll}} + \mathcal{G}^{nu}_{\text{bu}}. \tag{12}$$

where $\overline{\mathbf{F}} = \overline{\mathbf{F}}(t,\mathbf{x},v)$ *and* $\overline{R_v} = \overline{R_v}(t,\mathbf{x},v)$ *are the drag force and the evaporation rate taken at* $\mathbf{u}=\bar{\mathbf{u}}$*, and with :*

$$\mathcal{G}^n_{\text{coll}} = -n(v)\int\limits_{v^*\in[0,+\infty)} n(v^*)\beta(v,v^*)I^-_n\mathrm{d}v^* + \frac{1}{2}\int\limits_{v^*\in[0,v]} n(v^\diamond(v,v^*))n(v^*)\beta(v^\diamond(v,v^*),v^*)I^+_n\mathrm{d}v^*, \tag{13}$$

$$\mathcal{G}^{nu}_{\text{coll}} = -n(v)\int\limits_{v^*\in[0,+\infty)} n(v^*)\,\beta(v,v^*)I^-_u\mathrm{d}v^* + \frac{1}{2}\int\limits_{v^*\in[0,v]} n(v^\diamond(v,v^*))\,n(v)\,\beta(v^\diamond(v,v^*),v^*)I^+_u\mathrm{d}v^*, \tag{14}$$

where the partial collisional integrals I^-_n*,* I^+_n*,* I^-_u *and* I^+_u *are functions of* $(t,\mathbf{x},v,v^*)$ *and take the following expressions :*

$$I^-_n = |\bar{\mathbf{u}}(v)-\bar{\mathbf{u}}(v^*)|, \quad I^-_u = \bar{\mathbf{u}}(v)|\bar{\mathbf{u}}(v)-\bar{\mathbf{u}}(v^*)|, \tag{15}$$

$$I^+_n = |\bar{\mathbf{u}}(v^*)-\bar{\mathbf{u}}(v-v^*)|, \quad v\,I^+_u = ((v-v^*)\bar{\mathbf{u}}(v-v^*)+v^*\bar{\mathbf{u}}(v^*))\,|\bar{\mathbf{u}}(v^*)-\bar{\mathbf{u}}(v-v^*)|. \tag{16}$$

The source terms associated to secondary break-up reads, noting $\overline{\nu}^{\text{bu}}(v) = \nu^{\text{bu}}(v,\overline{\mathbf{u}}(v))$ *:*

$$\mathcal{G}^n_{\text{bu}} = -\overline{\nu}^{\text{bu}}(v)n(v) + \int\limits_{v^*>v} \overline{\nu}^{\text{bu}}(v^*)g_v(v,v^*,\overline{\mathbf{u}}(v^*))n(v^*)\mathrm{d}v^*, \tag{17}$$

$$\mathcal{G}^{nu}_{\text{bu}} = -\overline{\nu}^{\text{bu}}(v)n(v)\overline{\mathbf{u}}(v)) + \int\limits_{v^*>v} \overline{\nu}^{\text{bu}}(v^*)\,g_v(v,v^*,\overline{\mathbf{u}}(v^*))n(v^*)\overline{\mathbf{u}}(v^*)\mathrm{d}v^*. \tag{18}$$

We refer the reader to the thesis of [39] for the extension of the presented coalescence and break-up operators to sprays with the temperature as another internal variable which describes the unsteady heating of the droplets by the gaseous carrier phase.

The proof can be found in [37] and [39]. The validity of the assumption on the velocity distribution conditioned by size will be discussed in a more general framework in Section 3.2, whereas its applicability for polydisperse sprays with evaporation and coalescence to a nozzle test case will be treated in Section 3.4.

Remark 3. It has to be noticed that the coalescence source terms obtained in the equations do not conserve the global kinetic energy of the droplets. However, for the velocity and the temperature range we are interested in, the change in the temperature of the droplets due to the dissipation of the kinetic energy lost in the coalescence process is totally negligible. Besides, due to the statistical treatment of break-up, mass is conserved by the corresponding source terms, however, momentum is not.

3.1.5 Discretization in the size phase space

We choose a level of discretization for the droplet size phase space and we average the obtained semi-kinetic system of conservation equations over some fixed size intervals, each "fluid" corresponding to the set of droplets in each size interval. It can be interpreted as a finite volume discretization in the size variable, the order of which has been studied in [47] as far as the evaporation is concerned. The coalescence phenomenon, when taken into account, results in quadratic source terms in the Eulerian multi-fluid conservation equations for the mass and momentum of each "fluid". The coefficients involved in these source terms are collisional integrals; they do not depend on t, $\mathbf{x}$ or on the droplet size but only on the given droplet size discretization. Consequently, they can be pre-calculated before the resolution of the system of conservation laws is conducted.

The Eulerian multi-fluid model, is based on the reduction of a continuous semi-kinetic equation (11-12) as a function of size, to a finite number of degrees of freedom. This reduction is performed by averaging, in fixed size intervals : the sections (the k^{th} section being defined by $v_{k-1} \leq v < v_k$), of the semi-kinetic model. As a fundamental assumption, the form of n as a function of the geometry is supposed to be independent of t and $\mathbf{x}$ in a given section. Thus the evolution of the mass concentration of droplets $m^{(k)}$, in a section k, is decoupled from the repartition in terms of sizes $\kappa^{(k)}(v)$ inside the section ([30]) :

$$n(t,\mathbf{x},v) = m^{(k)}(t,\mathbf{x})\kappa^{(k)}(v), \qquad \int_{v_{k-1}}^{v_k} \rho_l\, v\, \kappa^{(k)}(v)\,\mathrm{d}v = 1. \tag{19}$$

The sections have fixed sizes, which is a major difference compared to a sampling method; however, they are not independent from each other, they exchange mass and momentum. The choice of the discretization points v_k, $k \in [1, N]$ has been studied in [48]; consequently we choose the $(N+1)^{\text{th}}$ section to be $[v_N, +\infty)$ in order to be able to describe the whole size spectrum. The final model is then obtained in the next proposition.

Proposition 4. *Besides assumptions* [H1]-[H3] *associated to the derivation of the semi-kinetic model, we make the following assumption on the velocity distribution inside a section :*

[H4] *In each section, the averaged velocity* $\bar{\mathbf{u}}(t,\mathbf{x},v)$ *does not depend on* v, $\bar{\mathbf{u}}(t,\mathbf{x},v) = \bar{\mathbf{u}}^{(k)}(t,\mathbf{x})$, *for* $v_{k-1} \leq v < v_k$.

We obtain the multi-fluid system of $2(N+1)$ *conservation equations :*

$$\partial_t m^{(k)} + \partial_{\mathbf{x}} \cdot (m^{(k)}\bar{\mathbf{u}}^{(k)}) = -(E_1^{(k)} + E_2^{(k)})m^{(k)} + E_1^{(k+1)}m^{(k+1)} + C_{\text{coll}}^{m\,(k)} + C_{\text{bu}}^{m\,(k)} \tag{20}$$

$$\begin{aligned}\partial_t(m^{(k)}\bar{\mathbf{u}}^{(k)}) + \partial_{\mathbf{x}} \cdot (m^{(k)}\bar{\mathbf{u}}^{(k)} \otimes \bar{\mathbf{u}}^{(k)}) = &-(E_1^{(k)} + E_2^{(k)})m^{(k)}\bar{\mathbf{u}}^{(k)} + E_1^{(k+1)}m^{(k+1)}\bar{\mathbf{u}}^{(k+1)} \\ &+m^{(k)}\overline{\mathbf{F}}^{(k)} + C_{\text{coll}}^{mu\,(k)} + C_{\text{bu}}^{mu\,(k)}\end{aligned} \tag{21}$$

where $E_1^{(k)}$ *and* $E_2^{(k)}$ *are the "classical" pre-calculated evaporation coefficients [23, 30] :*

$$E_1^{(k)} = -\rho_l\, v_k\, \overline{R_v}(t,\mathbf{x},v_k)\,\kappa^{(k)}(v_k), \quad E_2^{(k)} = -\int_{v_{k-1}}^{v_k} \rho_l\, \overline{R_v}(t,\mathbf{x},v)\,\kappa^{(k)}(v)\,\mathrm{d}v, \tag{22}$$

where $\overline{\mathbf{F}}^{(k)}$ *is the mean drag force :* $\overline{\mathbf{F}}^{(k)}(t,\mathbf{x}) = \int_{v_{k-1}}^{v_k} \rho_l\, v\, \overline{\mathbf{F}}(t,\mathbf{x},v)\,\kappa^{(k)}(v)\,\mathrm{d}v$, *and where the source terms associated with the coalescence phenomenon ,* $C_{\text{coll}}^{m\,(k)}$ *and* $C_{\text{coll}}^{mu\,(k)}$ *in the mass and momentum equation respectively of the* j^{th} *section are quadratic in the variables* $\left(m^{(k)}\right)_{k\in[1,N+1]}$ *and include the velocity difference between droplet of various sections* $V_{kj} = \left\|\bar{\mathbf{u}}^{(k)} - \bar{\mathbf{u}}^{(j)}\right\|$ *as well*

as collisional integrals $\mathcal{Q}_{kj}$, $k=[1,N+1], j=[1,N+1], k\neq j$, $\mathcal{Q}^{\diamond}_{ki}$, $\mathcal{Q}^{*}_{ki}$, $j=[2,N+1], i=[1,I^{(k)}]$, *the expression of which can be found in [36, 37]. The source terms associated with secondary break-up are to be found from the semi-kinetic model in [39]; they are linear in the variables* $\left(m^{(k)}\right)_{k\in[1,N+1]}$. *The source terms due to coalescence conserve mass and momentum, whereas the source term due to break-up only conserve mass, since the daughter droplets all relax to one single after-break-up velocity :*

$$\sum_{k=1}^{N+1} C_{\text{coll}}^{m\,(k)} = 0, \qquad \sum_{j=1}^{N+1} C_{\text{coll}}^{m\,(k)} = 0, \qquad \sum_{k=1}^{N+1} C_{\text{bu}}^{m\,(k)} = 0. \tag{23}$$

Let us mention that this model does not predict any coalescence between droplets of the same section since they have the same velocity and their probability of colliding is zero.

Finally, the coefficients used in the model, either for the evaporation process or the drag force $E_1^{(k)}$, $E_2^{(k)}$ and $\overline{\mathbf{F}}^{(k)}$, $k=[1,N+1]$ in (20-21), or the collisional integrals for evaluating the coalescence can be pre-evaluated from the choice of the droplet size discretization and from the choice of $\kappa^{(k)}$ since the collision integrals do not depend on time nor space. The algorithms for the evaluation of these coefficients are provided in [37] for coalescence and in [39] for break-up.

It has to be noted that such an approach can be extended to turbulent flows where some scales are modeled and not resolved, as opposed to the presented approach where all scales are resolved and which corresponds to DNS or laminar flows. Even if many strategies exists (see for example the recent theses [63, 64, 65] where ensemble averages for the particles are first taken for a given gaseous flow realization and then LES spatial averaging is introduced, we rather take ensemble average over turbulent realization of the gaseous flow at the "kinetic level" and then conduct the same kind of semi-kinetic modelling and finally sectional/multi-fluid size description as introduced in [66] and the following papers. The details of such an approach and validation can be found in [34, 40, 41, 67]

3.1.6 Non-dimensional equations

For the purpose of the next section devoted to the mathematical characterization of the system of partial differential equations, it will be easier to work with a dimensionless form of the equations. Once again, we restrict ourselves to a d^2 evaporation law, to a Stokes drag and neglect the heat exchange between the droplets and the gas in order to conduct this characterization. We introduce a characteristic gas velocity u^0, a characteristic length L and the corresponding time $\tau_{gas}=L/u^0$. Furthermore s^0 is a characteristic droplet surface, $\tau_{ev}^0=s^0/\left|R_s^0\right|$, a characteristic evaporation time based on a typical evaporation rate $\left|R_s^0\right|$; we use the two non-dimensional numbers $\mathrm{St}=\tau_p^0/\tau_{gas}$ the ratio of the typical droplet dynamical response time τ_p^0, based on s^0, over the gas characteristic time, called the Stokes number, as well as $\mathrm{E_v}=\tau_{gas}/\tau_{ev}^0$, the ratio of the gas time over the evaporation time based on s^0, which allows to define the non-dimensional evaporation rate $K=R_s/\left|R_s^0\right|$. In fact, it was convenient to work with the volume which is the natural size variable for the multi-fluid formulation since the only moment of the distribution function inside one section which is conserved is mass proportional to the droplet volume. Within the next section, we will deal with dynamics and evaporation which are easily defined in terms of surface so that is it easier to consider the evolution equations using s; in fact the Stokes number is proportional to droplet surface and the evaporation rate of a d^2 law is a constant as a function of surface indicating that the surface regression is affine versus time.

The non-dimensional evolution equations for an individual droplet then read :

$$\mathrm{d}_t\mathbf{x}_p=\mathbf{u}_p, \qquad \mathrm{d}_t\mathbf{u}_p=\frac{\mathbf{U}_{gas}(t,\mathbf{x}_p)-\mathbf{u}_p}{\mathrm{St}\,s_p}, \qquad \mathrm{d}_t s_p=\mathrm{E_v}\,K, \tag{24}$$

where $\mathbf{x}_p$ is the position of the droplet at time t, $\mathbf{u}_p$ its velocity and s_p its surface. The system of equations (24) can also be described through what is called the fine-grained phase space distribution function, defined by:

$$W(t,\mathbf{x},\mathbf{u},s) = \delta(\mathbf{x}-\mathbf{x}_p(t))\ \delta(\mathbf{u}-\mathbf{u}_p(t))\delta(s-s_p(t)), \tag{25}$$

which is therefore an Eulerian quantity, taking different values from one realization to another. The single particle PDF, P, is then defined as the ensemble average of the fine-grained (see [68]) distribution function $P(t,\mathbf{x},\mathbf{v},s) = \langle W \rangle$ which satisfies, as well as $f(t,\mathbf{x},\mathbf{u},s)$, the corresponding NDF (the summation over all single particle PDF's), the kinetic Williams-Boltzmann equation in non-dimensional form :

$$\partial_t f + \mathbf{u}.\partial_{\mathbf{x}} f + \partial_{\mathbf{u}} \cdot \left(\frac{\mathbf{U}_{gas}-\mathbf{u}}{\mathrm{St}\, s} f \right) - \mathrm{E_v}\, \partial_s (K\, f) = 0. \tag{26}$$

The initial conditions on the NDF are deduced from the distribution function of particles at time $t = 0$. If no other alea is introduced in the system, that is, for example, if $\mathbf{U}_{gas}(t,\mathbf{x}_p)$ is deterministically determined, the ensemble average mentioned above is only the expectation over the probability space associated with the initial distribution in the phase or sample space. It allows a particle-based definition of the NDF and provide a derivation of the Williams-Boltzmann equation when the forces acting on the particle are localized in phase space. It will be useful in order to make the link between Eulerian and stochastic Lagrangian descriptions of the liquid phase [42].

3.2 Mathematical Issues - Singularities

The assumptions formulated at the kinetic and at the macroscopic level while deriving the Eulerian model, lead to several mathematical difficulties. Indeed we obtain a peculiar system of conservation equations without any pressure term leading to singularities called "δ-shocks". These singularities occur when the monokinetic assumption of the multi-fluid model ceases to be valid and introduces some artificial velocity averaging. The key issue is thus to characterize the appearance of such singularities and to relate it to the physics of droplet dynamics. This will have two consequences, first we will be able to choose comparison configurations which are within the validity limit of the multi-fluid model; second, since the configurations of interest frequently involve flow location which can be a little beyond the validity limit and still can be accurately described by the multi-fluid model, we aim at developing a numerical method robust enough to cope with these singularities in case they do occur.

3.2.1 Mathematical peculiarities of Multi-fluid modeling

This multi-fluid system of equations contains a peculiar transport term similar to the pressureless gas system studied for example in [46]. Indeed, it is similar to an Euler gas dynamics system of equations, but without any pressure term in the momentum equation; that is, if we consider a single section and focus on the left hand side of the system of equations, it corresponds to the limit of zero temperature of the gas dynamics equations :

$$\left\{ \begin{array}{rcl} \partial_t(m^{(1)}) + \partial_{\mathbf{x}} \cdot (m^{(1)}\bar{\mathbf{u}}^{(1)}) & = & 0, \\ \partial_t(m^{(1)}\bar{\mathbf{u}}^{(1)}) + \partial_{\mathbf{x}} \cdot (m^{(1)}\bar{\mathbf{u}}^{(1)} \otimes \bar{\mathbf{u}}^{(1)}) & = & 0. \end{array} \right. \tag{27}$$

This system can be found for example in astrophysics, when describing the formation of large scale structures in the universe or in the modeling of sticky particles [45]; it has also been presented in [69] for bubbles. It has the peculiarity to be weakly hyperbolic and can generate

"δ-shocks" (that is a discontinuity in velocity which leads to Dirac delta function concentration in density) or create vacuum zones. Note that it is important to be able to cope efficiently with vacuum zones since they represent areas of the flow where no droplet is to be found and are commonly encountered in most applications. In fact the equation on the velocity itself is decoupled from the conservation of mass and takes the form of the Burger's classical equation :

$$\partial_t \bar{\mathbf{u}}^{(1)} + \bar{\mathbf{u}}^{(1)} \cdot \partial_x \bar{\mathbf{u}}^{(1)} = 0. \tag{28}$$

A shock may then arise, leading to the concentration of density at its interface. This shock occurs for example when droplets cross each-other : indeed we have at the same space and time location two velocities. In the resolution of the whole problem, as formulated in Equations (20,21), the drag term will decrease the occurrence of such crossings, attracting droplet velocity towards gas velocity. Nevertheless, for droplets inertial enough, influence of drag is weaker and crossings may still occur. As we already mentioned in the assumption [H1], Section 3.1, we only have one averaged velocity at a given point, preventing the description of droplet crossings of the same size. In the two-fluid model, also based on one averaged velocity, the same problem occurs and droplet crossings can neither be described. Nevertheless, the multi-fluid model can use multiple sections for the description of polydispersity and thus allows crossing of droplets which do not belong to the same size interval. Nevertheless, equally-sized droplet crossings are out of the limits of the multi-fluid model and can not be described.

This observation has three consequences. First we want to be able to control droplet dynamics for a given gaseous flow. Indeed for turbulent flows or even for laminar flows with contra-rotative vortices or impinging jets, equally-sized droplet crossings may occur. We would like to be able, through a limitation on the Stokes number of the droplets, to foresee these crossings and prevent them to occur inside a standard multi-fluid model. Second we want to develop a numerical method robust enough to cope with the velocity discontinuities and density concentration arising if equally-sized droplet crossings do still occur at rare occasions in the flow. Finally, for Stokes numbers high enough such that crossing will be essential and has to be described, we have to switch to more complex model which will be presented in the second part of these Notes.

A specific numerical method is consequently needed for the multi-fluid model, requiring :

- to stand high gradients even up to the situation where all the mass density would be concentrated in one cell;
- to preserve the positivity of mass density;
- to reproduce a discrete maximum principle on the velocity.

Furthermore, we also want an order of accuracy high enough as well as limited numerical diffusion in cases of regular distribution to limit the number of cells needed. It will be essential in order to treat multi-dimensional configurations. The development of such a numerical method is presented in Section 3.3.

3.2.2 Detailed analysis of multi-fluid limits

The peculiar structure of the multi-fluid system and the set of associated assumptions require a precise analysis of droplet dynamics description. The purpose of this paragraph is to provide the key ideas of the analysis yielding the definition of a critical Stokes number, St_c, below which the assumptions of the multi-fluid are valid. We first introduce the fundamentals of the analysis in a typical one dimensional problem defining a critical Stokes number. We then extend this

definition to two-dimensional problems in the context of Taylor-Green vortices for the gaseous flow. The extension to a more general framework for more complex flow field is then considered. Finally we perform Lagrangian numerical applications in these configurations, to study the validity of the theoretical criterion introduced.

1-D model problem and critical Stokes number - The purpose of the present section is to identify the critical point for the appearance of "δ-shocks" [46, 70], that is, the eventual concentration up to infinity of the density field related to the creation of a discontinuous velocity field. Such an event corresponds to the crossing of characteristic curves in the physical space [71] and to the limit of the monokinetic character of the NDF at the kinetic level, i.e. the velocity distribution at given location becomes multi-valued. These characteristic curves are defined, for both the kinetic equation (1) and the system of conservation laws (11,12), in the case of non-evaporating droplets, by a set of ordinary differential equations (ODE) and initial conditions :

$$\left\{ \begin{array}{rclcrcl} \mathrm{d}_t x_p & = & u_p & & x_p(0) & = & x_p^0 \\ \mathrm{d}_t u_p & = & \dfrac{U_{gas}(t,x_p)-u_p}{\mathrm{St}} & , & u_p(0) & = & u_p^0 \end{array} \right. , \tag{29}$$

with $u_p^0 = \bar{u}^{(1)}(0, x_p^0)$ since the initial distribution is monokinetic. It should be noticed that the non-linear coupling between the two fields is contained in the fact that the gaseous velocity field U_{gas} is only sampled by the droplet trajectory at x_p. Thus, the characteristic curves are the integral curves of the vector field defined by Equations (29), parametrized by the initial spatial coordinate so that we will adopt the notation $(x_p, u_p)^t(t, x_p^0)$. Under some standard conditions on the regularity of the field U_{gas}, the characteristic curves exist and are well-defined for all time and spatial initial conditions. However, as soon as some characteristic curves cross each other in the only spatial projection of the characteristic diagram (x, t), the distribution ceases to be monokinetic and the equivalence between the macroscopic and kinetic descriptions is not valid any more. In fact the characteristics never cross each other in the (x, u) phase space so that the distribution admits multiple velocities at a point where the spatial projection of the characteristics cross each-other. For the sake of simplicity the generic example of steady gaseous flow field is given by a spatial harmonic oscillation $U_{gas}(x) = \sin(2\pi\, x)$, with periodic boundary condition on the spatial interval $[0, 1]$. The initial condition for the spray is a uniform zero velocity distribution $\bar{u}^{(1)} = 0$, as well as a constant density distribution $m^{(1)} = 1$. The characteristic first crossing point can be shown to be at $x = 1/2$ since this is the point of maximal strain. In order to characterize the limit we linearize the original system of ODEs Equation (29) at $x = 1/2$ for which the eigenvalues of the associated matrix are real, if and only if $8\pi\,\mathrm{St} \leq 1$. The limiting value of the Stokes number is then $\mathrm{St}_c = 1/(8\pi) \approx 0.0398$. Taking a look at Figure 1 will provide the reader with the intuitive picture of two cases where there is or there is not characteristic crossing. We have represented on the left the trajectories of the particles (that are also the characteristic curves in this pressureless configuration) with the usual convention that the abscissa is the spatial coordinate and the ordinate, the time evolution. We consider thirty equidistributed initial spatial positions and a zero initial velocity. We plotted the evolution of the position versus time for two Stokes numbers which are above and below the critical one. It can be clearly seen that the characteristics cross at $x = 0.5$ for $\mathrm{St} = 0.3$ at time around $t = 0.5$ which corresponds to the first time when the velocity distribution at $x = 0.5$ becomes multi-valued as shown in the position-velocity phase plane on the top-right of Figure 1. On the contrary, such a scenario never occurs for $\mathrm{St} = 0.03$ for which the characteristic curves never cross and the velocity field as a function of position always remain monokinetic as presented in Figure 1-bottom.

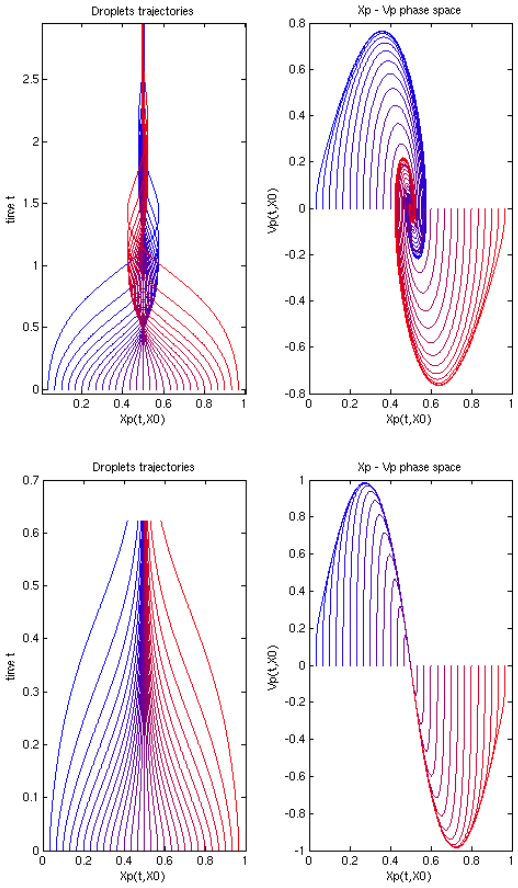

Figure 1: (top) : St = 0.3, St > St_c, characteristic crossing in the (x, t) plane (left) and phase plane dynamics (x, v) (right) for 30 initial conditions equally distributed in space with zero initial velocity; (bottom) : St = 0.03, St < St_c, no characteristic crossing in the (x, t) plane (left) and phase plane dynamics (x, v) (right) for 30 initial conditions equally distributed in space with zero initial velocity.

For Stokes numbers beyond the critical limit, let us underline the fact that, even for the Williams-Boltzmann equation at the kinetic level, there is a singularity at the time when the characteristics are crossing in the (x,t) diagram. At this exact time, the zeroth order moment of the NDF, that is the number density of droplets, becomes infinite at $x = 1/2$ and the original modeling at the kinetic level can cease to be valid if the initial droplet number density is high enough for the collision term to become important in the neighborhood of the axis of symmetry where the singularity occurs. Even if this singularity is spatially integrable, the original modeling on the NDF should then involve a collision term or a "granular pressure". For an interesting study of the influence of the initial number density of droplets on the influence of the collisional term in the NDF equation in a different framework, we refer to the work of Volkov and collaborators (see [72] and references therein) as well as the study we have conducted during the Summer Program 2008 for finite Knudsen number crossing jets involving collisions [51].

This will prove to be symptomatic of what happens in multi-dimensional configurations with more complex flows.

Taylor-Green vortices - In the two-dimensional version of the steady spatially oscillating gaseous flow field, we consider a steady solution of the incompressible Euler equations with periodic boundary conditions. We use the following notations $\mathbf{U}_{gas} = (U,V)^t$ for the two components of the gaseous velocity field and it reads in the non-dimensional setting $U = \sin(2\,\pi\,x)\,\cos(2\,\pi\,y)$ for the horizontal velocity, and $V = -\cos(2\,\pi\,x)\,\sin(2\,\pi\,y)$ for the vertical one, $(x,y) \in [0,1] \times [0,1]$. The structure of the flow field is presented in Figure 2 through the stream lines.

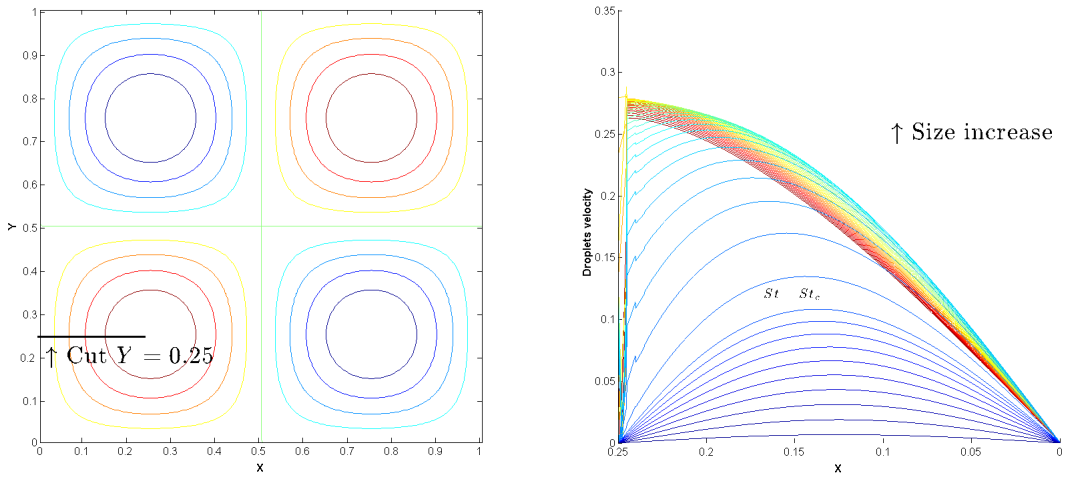

Figure 2: (left) Stream lines of the Taylor-Green vortices and position of the cut for the study of normal ejection velocity, (right) Structure of the invariant droplet velocity manifold versus Stokes number in term of the velocity component orthogonal to the gas flow.

In order to analytically characterize the critical Stokes number, we focus on the behavior of the system around the central point $(1/2, 1/2)$. The characteristics in their non-dimensional

form are then linearized at this point and it yields :

$$\begin{cases} \mathrm{d}_t x_p &= U_p, \quad \mathrm{d}_t U_p &= \dfrac{2\,\pi\, x_p - U_p}{\mathrm{St}}, \\ \mathrm{d}_t y_p &= V_p, \quad \mathrm{d}_t V_p &= \dfrac{-2\,\pi\, y_p - V_p}{\mathrm{St}}. \end{cases} \tag{30}$$

The system in the two directions then decouples and the eigenvalues in the x direction are always real, whereas one recovers the same analysis in the y direction as in the 1D case, with the same critical value of the Stokes number St. It can be shown that, for the considered initial monokinetic velocity distribution, the first point of characterics crossing is at the center point $(1/2, 1/2)$ which is again the point of maximum rate of strain. Besides, as shown in [42], the droplet velocity field is rapidly attracted, within a few Stokes number, to an invariant velocity manifold which is smooth only if the non-dimensional Stokes number is below its critical value and becomes discontinuous beyond this threshold, thus allowing the droplets to go from one vortex to its neighbors. This phenomenon is presented in Figure 2-right where the invariant droplet velocity normal to the stream lines of the gaseous velocity field is plotted. Beyond the obtained Stokes critical value, the droplets are ejected from the vortices and encounter the droplets coming from the other vortices, since the original number density or droplets is symmetrical. Consequently, for Stokes numbers below this critical value, we are sure that the multi-fluid assumptions will be valid in the sense that the kinetic modeling and the fluid modeling provide identical descriptions. We will then be able to conduct thorough comparisons with a Lagrangian solver as in [42]. For Stokes numbers beyond this critical value, the multi-fluid model and the kinetic model are not coherent any more. The Williams-Boltzmann spray equation also encounters a singularity if no collision model or granular interaction is added. The Eulerian semi-kinetic and multi-fluid models both lead to infinite density concentrations and discontinuous velocity fields as presented in Figure 2.

Relation to mathematical studies - In fact, in the non-dimensional gas velocity variables, the maximal value of the strain for both 1D and 2D cases is 2π at the symmetry point. From [73] it can be shown that system (11,12) is equivalent to the kinetic Williams-Boltzmann equation for monokinetic initial velocity distributions under two conditions on both the initial velocity field $\bar{u}^{(1)}(0,\dot{)}$ and on the maximum $a^{\max}$ of the derivative of the steady gaseous velocity field. The variable $a^{\max}$ denotes the maximal rate of strain of the gaseous flow field. In non-dimensional variables, the conditions can be written $a^{\max}\,\mathrm{St} < 1/(4\,d)$ and $|\partial_{\mathbf{x}} \bar{u}^{(1)}(0,\mathbf{x})|_\infty\,\mathrm{St} < 1/(2\,d)$. Since in the preceeding case, $a^{\max} = 2\,\pi$, one recovers the obtained condition on the critical Stokes number in the one-dimensional setting. These two conditions thus insure, from a mathematical point of view that the kinetic NDF will remain monokinetic, if it was originally so, for all times. In this context this provides a rigorous basis in order to insure the validity of the semi-kinetic and multi-fluid model.

However, it has to be underlined that the complete study for unsteady gaseous flows is far more challenging and should be studied. The diversity of the possible scenarios is much richer and requires a dedicated study which will not be presented in these Notes.

3.3 Eulerian multi-fluid specific numerical method

The numerical method designed for the multi-fluid method must deal with the complex mathematical structure of the governing system of equations, described and illustrated in the previous section. Furthermore, the numerical scheme has to present the best compromise between precision and cost, in order to tackle more complex 2-D jet or 3-D configurations (see section 6). In

order to treat efficiently the different difficulties of the multi-fluid system, that are a complex transport term and stiff source terms, we use an operator splitting, [74, 75, 76]. It allows to design efficient numerical methods for each contribution. Furthermore, one takes advantage of the structured grids used in this study to introduce a dimensional splitting to treat multi-dimensional configurations, leading to a high efficiency. One has to note that this choice is not restrictive since extension to unstructured grids have been proposed in the literature.

3.3.1 General Scheme

Phenomena involved in our problem are of two different types: transport induces an evolution in the physical space without leading to any interaction between the sections, whereas transport in internal coordinate space, i.e., size and velocity through evaporation, drag, heat transfer and collisions, induces an evolution without any coupling with the spatial coordinates. It is then interesting to separate them using an operator-splitting method. The multi-fluid system, Equations (20,21), is then split into two systems, for the physical space and for the phase space. On one hand, the evolution in physical space for the multi-fluid size section k reads:

$$\left\{ \begin{array}{rcl} \partial_t\ m^{(k)} + \partial_{\mathbf{x}} \cdot \left(m^{(k)}\ \bar{\mathbf{u}}^{(k)} \right) & = & 0, \\ \partial_t\ \left(m^{(k)} \bar{\mathbf{u}}^{(k)} \right) + \partial_{\mathbf{x}} \cdot \left(m^{(k)}\ \bar{\mathbf{u}}^{(k)} \otimes \bar{\mathbf{u}}^{(k)} \right) & = & 0. \end{array} \right. \tag{31}$$

On the other hand, the phase space evolution, in internal coordinate space, reads for section k:

$$\left\{ \begin{array}{rcl} \mathrm{d}_t\ m^{(k)} & = & -\left(E_1^{(k)} + E_2^{(k)} \right)\ m^{(k)} + E_1^{(k+1)}\, m^{(k+1)}, \\ \mathrm{d}_t\ \left(m^{(k)} \bar{\mathbf{u}}^{(k)} \right) & = & -\left(E_1^{(k)} + E_2^{(k)} \right)\ m^{(k)} \bar{\mathbf{u}}^{(k)} + E_1^{(k+1)}\, m^{(k+1)} \bar{\mathbf{u}}^{(k+1)} + m^{(k)}\ \overline{\mathbf{F}}^{(k)}. \end{array} \right. \tag{32}$$

The operator-splitting method consists in solving alternatively these simpler problems (31) and (32) in order to approximate the solution of the full problem (20,21). We choose a Strang splitting which is second order in time provided all the steps are second order in time, with the following structure, see [76]:

- Phase space transport: solve system of equations (31) during $\Delta t/2$,
- Physical space transport: solve system of equations (32) during Δt,
- Phase space transport: solve system of equations (31) during $\Delta t/2$.

This approach has the great advantage to preserve the properties of the schemes we use for the different contributions, as for example maximum principle or positivity. If we assume that the involved phenomena evolve at roughly similar time scales, this Strang splitting algorithm guaranties a second order precision in time provided that each of the elementary schemes has at least a second order time accuracy.

As mentioned in [71], this Strang splitting can also be obtained with an algorithm based on a Lie splitting. The Lie splitting is composed of two steps of length Δt. The Strang splitting is constructed with this two steps but it alternates the order in which they are performed:

1. iteration 2n
   - Phase space transport: solve system of equations (31) during Δt,
   - Physical space transport: solve system of equations (32) during Δt,
2. iteration 2n+1

- Physical space transport: solve system of equations (32) during Δt,
- Phase space transport: solve system of equations (31) during Δt.

This form is in fact a classical Strang splitting with a splitting timestep $2\Delta t$. The error due to the splitting increases, but all the steps are of length Δt and this will be important in terms of the global accuracy of the scheme. There is no CFL reduction in the physical space transport. Furthermore, to advance the solution of Δt we need to perform only two steps and not three, and it leads to a benefit in the computational efficiency of the algorithm.

3.3.2 Physical space transport resolution

Let us recall that the transport term in physical space for both the semi-kinetic model and the each section is the pressureless gas system ([46]) and reads for example for the first section :

$$\left\{ \begin{array}{rcl} \partial_t(m^{(1)}) + \partial_{\mathbf{x}} \cdot (m^{(1)} \bar{\mathbf{u}}^{(1)}) & = & 0, \\ \partial_t(m^{(1)} \bar{\mathbf{u}}^{(1)}) + \partial_{\mathbf{x}} \cdot (m \bar{\mathbf{u}}^{(1)} \otimes \bar{\mathbf{u}}^{(1)}) & = & 0. \end{array} \right. \tag{33}$$

A specific numerical method is needed in order to cope with discontinuous velocity fields, "δ-shocks" as well as with vacuum. We need a method which strictly preserves the positivity of the density field, allows the concentration of all the density in one cell without leading to an instability of the method, and guarantees the maximum principle on the velocity. This is quite a constraint, however, we still at least require a second order in order to limit the numerical diffusion as well as the level of discretization requires for a precise calculation. Bouchut in [70] developed second order kinetic schemes, which are finite volume schemes based on the equivalence between a macroscopic and a microscopic level of description for the pressureless gas equations. For the purpose of the exposition, we will work in one dimension and will forget about the superscript :

$$\partial_t f + u\, \partial_x f = 0 \iff \left\{ \begin{array}{rcl} \partial_t(m) + \partial_x \cdot (m\bar{u}) & = & 0 \\ \partial_t(m\bar{u}) + \partial_x \cdot (m\bar{u}^2) & = & 0 \end{array} \right. \tag{34}$$

with :

$$f(t,x,u) = m(t,x)\delta(u - \bar{u}(t,x)). \tag{35}$$

The values of m and $\bar{u}$ are then recovered from f by the formula :

$$\left(\begin{array}{c} m \\ \bar{u} \end{array} \right)(t,x) = \int_{\mathbb{R}} \left(\begin{array}{c} 1 \\ u \end{array} \right) f(t,x,u) du. \tag{36}$$

This is precisely the same framework as the one we encountered for the semi-kinetic model and will apply to the multi-fluid model.

The principle of such a method is a finite volume method giving approximations m_j^n and $q_j^n = m_j^n u_j^n$ of the following averaged values on each cell $[x_{j-1/2}, x_{j+1/2}]$ of m and $m\bar{u}$ at each discrete time t^n :

$$m_j^n \simeq \frac{1}{\Delta x} \int_{x_{j-1/2}}^{x_{j+1/2}} m(t^n,x)dx, \qquad q_j^n = m_j^n u_j^n \simeq \frac{1}{\Delta x} \int_{x_{j-1/2}}^{x_{j+1/2}} m(t^n,x)\bar{\mathbf{u}}(t^n,x)dx. \tag{37}$$

First, at time $t = t^n$, a distribution function $f^n(x,u)$ is reconstructed from the averaged values m_j^n and q_j^n. This comes from Equation (35) and, for example, a piecewise linear reconstruction of $m(t^n,x)$ and $\bar{u}(t^n,x)$ with adequate slope limiters will work. Second, the kinetic equation is solved analytically between t^n and t^{n+1} : $f(t,x,u) = f^n(x - \bar{u}(t-t^n), u)$. Finally, a projection

of $f(t^{n+1-}, x, u)$ is conducted in order to find m_j^{n+1} and q_j^{n+1}, which corresponds to the average on each cell of (36) at $t = t^{n+1-}$. This leads to the following scheme :

$$m_j^{n+1} = m_j^n - \frac{\Delta t}{\Delta x}\left(\mathcal{F}^m_{j+1/2} - \mathcal{F}^m_{j-1/2}\right), \tag{38}$$

$$q_j^{n+1} = q_j^n - \frac{\Delta t}{\Delta x}\left(\mathcal{F}^q_{j+1/2} - \mathcal{F}^q_{j-1/2}\right), \tag{39}$$

with the numerical fluxes :

$$\boldsymbol{\mathcal{F}}_{j+1/2} = \begin{pmatrix} \mathcal{F}^m_{j+1/2} \\ \mathcal{F}^q_{j+1/2} \end{pmatrix} = \frac{1}{\Delta t}\int_{t^n}^{t^{n+1}} \int_{\mathbb{R}} \begin{pmatrix} 1 \\ u \end{pmatrix} u f^n(x_{j+1/2} - \bar{u}(t-t^n), u) du dt. \tag{40}$$

The obtained fluxes rely, through Equation (35), on the reconstructions of $m^n(x) = m(t^n, x)$ and $\bar{u}^n(x) = \bar{u}(t^n, x)$ from the discrete values m_j^n and u_j^n. Different type of reconstructions are proposed in [70] and we have chosen the one which gives good results without being too complex, a piecewise linear reconstruction. The detailed expressions of the fluxes and the adapted version of the scheme to our case can be found in [42, 43].

For the 2D and 3D cases we are dealing with, in the framework of cartesian meshes, the same type of numerical method is written in [70]. However, it is hard to find a good slope limiter which does not induce too large a numerical diffusion. That is why we rather use a dimensional splitting of the 1D scheme previously described, with a Strang type splitting to preserve the second order of the method as indicated in [71]. Finally, the algorithm has been extended to 2D-axisymmetrical configurations using the same dimensional splitting; it uses a radial version of the 1D algorithm designed in [77, 53]. Besides, such an approach is very competitive as far as computational cost and level of accuracy is concerned, since it as a very performing way of limiting numerical diffusion.

3.3.3 Phase space transport resolution

We need to solve, in the phase space transport step, the ODE system (32). The polydispersion resolution leads to a multi-scale problem. Indeed, droplets of different sizes have different response time to the physical phenomena. The ODE integrator must then be carefully chosen.

The Runge-Kutta implicit methods are particularly well suited for stiff problems, see for example [78]. Among them, the implicit Runge Kutta method based on Radau quadrature is called Radau IIA. We choose a 5^{th} order version of this integrator, obtained with a three-stage Radau quadrature of order 5. This method is shown to be A-stable in [78]. Furthermore, this method is L-stable, that allows a very fast convergence, with a fast high frequency absorption. This property is of importance for multi-fluid simulation as low inertia droplet velocity relaxes very rapidly to gas velocity, under drag force effect. An important limitation of this method, is the difficulty to obtain an efficient implementation of its algorithm. However, this Radau IIA method is implemented in the program RADAU5, written by Hairer, see [78]. It offers a very efficient algorithm, solving very efficiently the nonlinear systems involved.

3.3.4 Conclusion on the algorithm optimality

The scheme we have designed then offers the ability to treat delta-shocks and vacuum. It guaranties a maximum principle on the velocity as well as the positivity of the density in the transport of physical space. Moreover, it is second order accurate in space and time and, with the precise splitting structure we have chosen, it leads to limited numerical diffusion, a key issue for Eulerian models and numerical methods. It is important at this level to insist on

the structure of the algorithm and the implications on the numerical diffusion of the obtained scheme; we will come back on these issues when comparing Eulerian and Lagrangian solvers in terms of accuracy.

3.4 Numerical validations

We present first precise and quantitative comparisons between the Lagrangian and the Eulerian descriptions for the Taylor-Green vortices where the analytical gaseous velocity field as well as the polydisperse spray initial condition provide a challenging test case and are representative of the main problems we will encounter in more complex configurations. The first ingredient is to define a procedure to be able to compare the accuracy of both methods; we then use it for both a non-evaporating and an evaporating case. We will then present the results we obtained concerning comparisons in an Isotropic Homogeneous Turbulence configuration. Finally we will show the size-conditionned dynamics comparisons realized in a 2D axisymmetric free jet with evaporating polydisperse spray injection.

3.4.1 Taylor-Green configuration

Comparison procedure - To evaluate differences between the two spray solutions, given a gaseous velocity field, we need to reconstruct Eulerian fields from the statistical information provided by the Lagrangian treatment. We thus need to define an Eulerian grid to perform this reconstruction. Furthermore, as we want to compare the Lagrangian results to the multi-fluid ones, we want to perform comparisons for various droplet sizes in order to study the ability of the Eulerian method to capture dynamics of droplets of various sizes. In our two-dimensional Taylor-Green case, we need a three-dimensional grid to account for space and size discretizations. We have chosen in this case a $100 \times 100 \times 10$ grid, to have a sufficiently detailed description of the fields : 100×100 for the space discretization, and 10 size intervals to be able to study polydispersity. Let us recall that we work with non-dimensional quantities on the space and size cube $[0,1] \times [0,1] \times [0,1]$.

The initial spatial and size distributions are presented in Figure 3. As a matter of fact, this distribution will allow to analyze numerical diffusion of the method, and to determine the spatial refinements needed. Indeed its gradients are important as we can see in Figure 3 (left) where we realized a three dimensional plot to represent the droplet number density in the domain. The droplets are introduced in the computational domain with a zero initial velocity in both cases.

Computing errors on this grid means :

- reconstructing the Eulerian fields for the mass densities in the size intervals from the Lagrangian statistics on this grid;
- averaging, if necessary, the Eulerian multi-fluid results on this very grid.

An example of such a reconstruction is to be found in Figure 4 where a zoom is presented (we have focused on a quarter of the computational domain, which is the zone of interest).

We evaluate on this grid the global error at the time $t = 1.5$ (i.e. the dimensional time is 1.5 times the gaseous flow field time, which is the ratio of the characteristic period of the Taylor-Green lattice over the maximum of the velocity field; roughly, it corresponds to one and a half eddy turn over time). The constant by pieces error field for a generic quantity Q, which in the following will be mainly the droplet mass density in one section, is defined for an Eulerian computation by:

$$E_Q^{1.5}(x,y) = Q_{\mathrm{e}}^{1.5}(x,y) - Q_{\mathrm{l-ref}}^{1.5}(x,y), \tag{41}$$

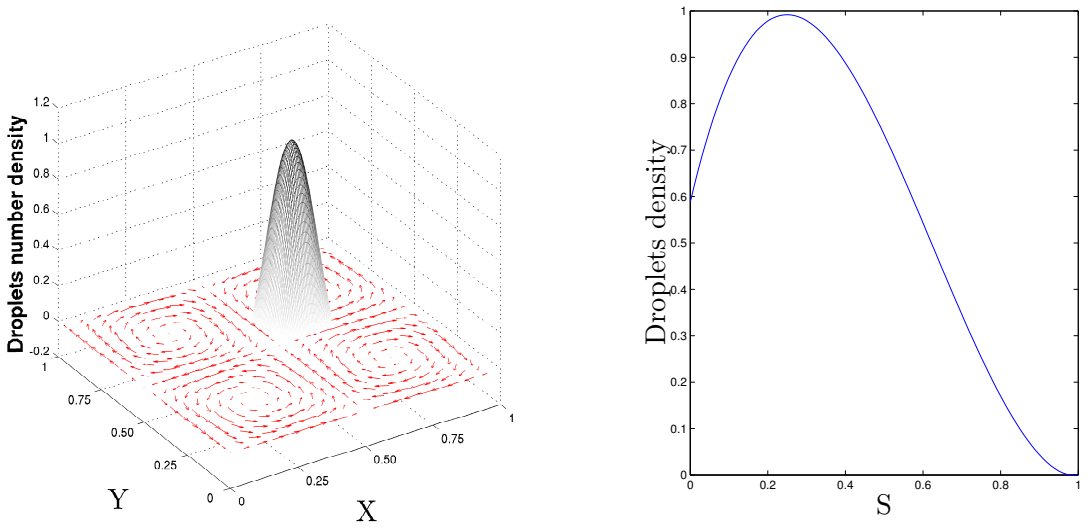

Figure 3: Initial droplet distribution : (left) non uniform spatial repartition, three-dimensional plot with number density as the third coordinate; (right) non-dimensional polydisperse size distribution.

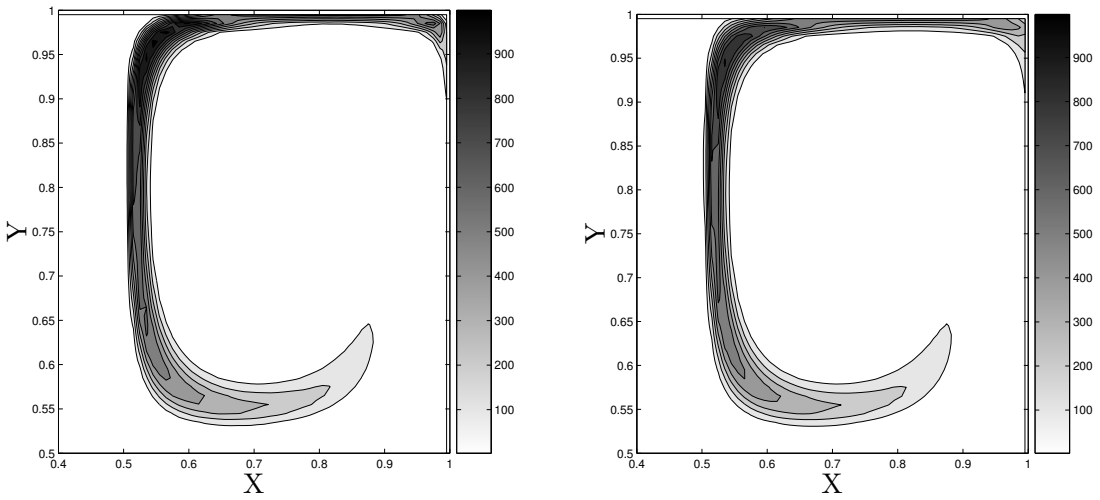

Figure 4: Zoom on the top-right quarter of the periodic computational domain of the total mass density of droplets at time $t = 1.5$, projected on the comparison grid $100 \times 100 \times 10$: (left) Lagrangian reference solution, (right) Eulerian with a $400 \times 400 \times 10$ grid.

where the fields are taken to be constant inside a cell of the comparison grid. The right-hand-side corresponds to the averages over the associated cell of both the Eulerian simulation (subscript e) and the Lagrangian reference simulation with 16 Million particles (subscript $\mathrm{l}-\mathrm{ref}$), respectively.

To have an estimate of the relative error over the whole grid, we study the L^1 norm of the relative error on the grid :

$$||E_Q^{1.5}||_1 = \frac{\int_0^1 \int_0^1 |Q_{\mathrm{e}}^{1.5}(x,y) - Q_{\mathrm{l-ref}}^{1.5}(x,y)|\mathrm{d}x\mathrm{d}y}{\int_0^1 \int_0^1 |Q_{\mathrm{l-ref}}^{0}(x,y)|\mathrm{d}x\,\mathrm{d}y}. \tag{42}$$

The denominator is taken at the initial time, but this has no impact on the non-evaporating case since the global mass as well as the mass in the sections are preserved throughout the calculation. For the evaporating case, this has however an impact and allows to quantify the error relative to the initial amount of mass, which is the one with the main physical sense.

Non Evaporating spray - To illustrate comparisons between the Eulerian and the Lagrangian methods previously described, we present a study of the error between the Lagrangian reference case with 16 Million particles and the Eulerian cases, to show that both methods converge towards the same results. The chosen time for the comparison is $t = 1.5$, for which the total mass density is presented in Figure 4. It exhibits a high concentration of the inertial droplets around the vortex and creates very high gradient areas. It is thus a really challenging test case as far as Eulerian models are concerned, irrespective of the evaporation process. We now discuss the error plots presented in Figures 5 to 7 where the details of the comparisons are conducted for three representative sections illustrating the influence of the droplets inertia on their behavior. With respect to the critical Stokes number St_c introduced in the previous section. This critical Stokes identify the critical point for the apparition of equally-sized droplet crossings, and then of δ-shock singularities, as detailed in [79]. The Figures 5 to 7 represent the evolution of the logarithm of the relative error between Eulerian multi-fluid cases and the reference Lagrangian computation versus the logarithm of the space discretization step of the Eulerian computation. For convenience, we have presented the actual values of the error and of the space discretization step on the two axis, but the points on these axis correspond to the logarithms of these values. As we mentioned in the previous report [79], the numerical method used for the multi-fluid model is second order in space, explaining the line with a slope equal to two in all the pictures. The plots show three different levels of space refinements for the Eulerian computation : 100×100, 200×200 and 400×400. In order to see the influence of the refinement in size of the multi-fluid model, we plot three curves in each Figure, showing three size discretizations : 10, 20 and 30 sections.

Concerning the droplets of intermediate size presented in Figure 6, the Eulerian computation converges towards the Lagrangian reference case with almost second order. Furthermore, ten sections are enough for the size discretization since the size refinement does not have any impact on the global error. The effect of the size discretization step refinement in this non-evaporating case is purely a finer description of the velocity distribution as a function of droplet size for a given location and time. Consequently, in the range of Stokes number associated to these droplets of intermediate size, the size-dependence of the velocity field is not strong enough to require a finer discretization and the dynamics of the droplets are correctly reproduced by the 10 sections case. For more inertial droplets, Figure 7, the order of convergence is weaker and it is not improved by the refinement in section. As a matter of fact, this is due to the high gradient appearing for this class of droplets; indeed the inertial droplets are quickly ejected from the vortex and form high concentration regions and therefore very high gradients (most of the mass is concentrated in a few cells). In this case, the numerical method reduces its order of precision

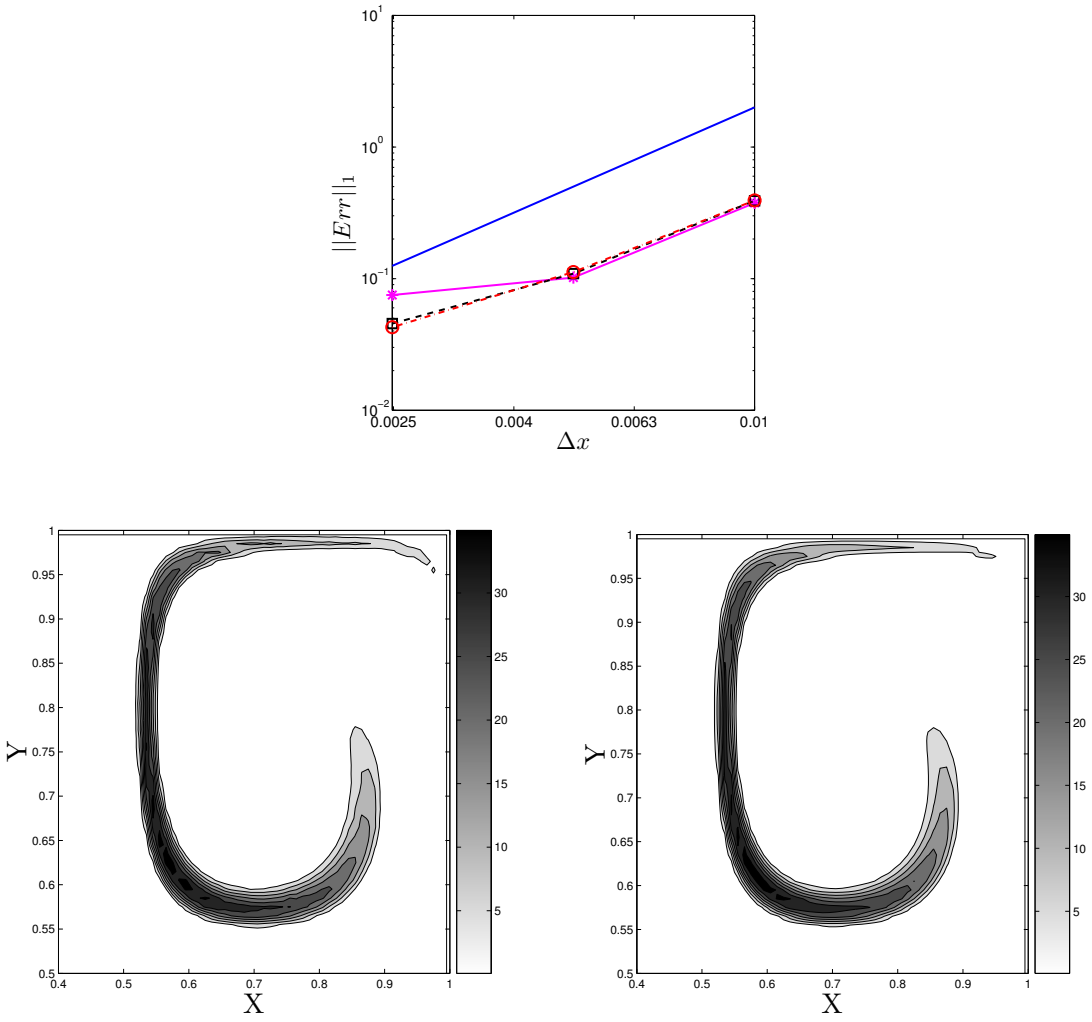

Figure 5: (top) Logarithm of L^1 norm of the error between Eulerian simulation for small droplets (second section $\mathrm{St} = 0.14\,\mathrm{St}_c$) for various Δx and the Lagrangian reference solution at time $t = 1.5$, projected on the comparison grid $100 \times 100 \times 10$: slope two line (blue solid line), 10 sections (magenta solid line), 20 sections (dashed line) and 30 sections (dotted-dashed line). (bottom) Corresponding droplet mass density with 10 iso-contours from 0 up to 1.44-time the maximum of the initial mass density in the second section : (left) Lagrangian reference solution, (right) Eulerian computation with a $400 \times 400 \times 10$ grid.

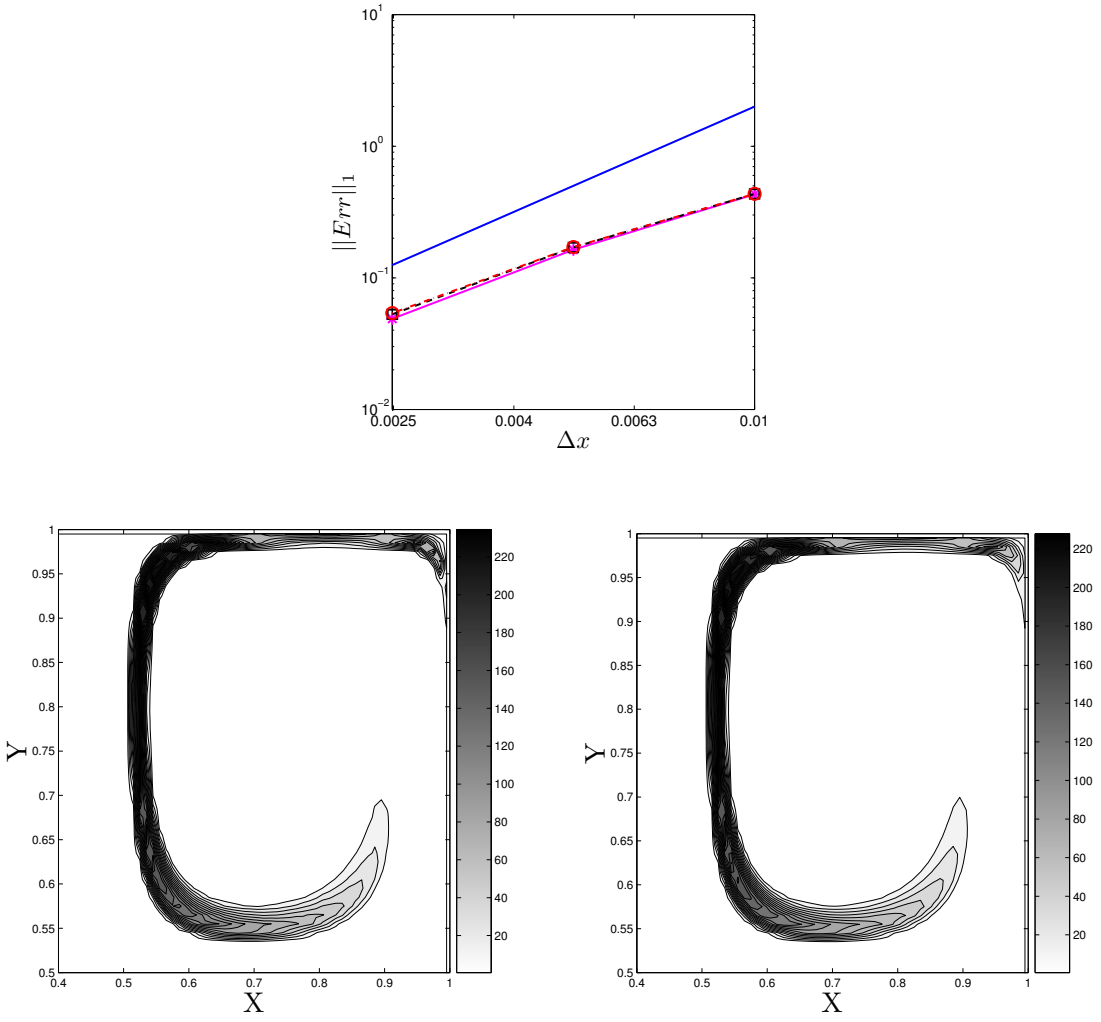

Figure 6: (top) Logarithm of L^1 norm of the error between Eulerian simulation for medium size droplets (fifth section $\mathrm{St} = 0.41\,\mathrm{St}_c$) for various Δx and the Lagrangian reference solution at time $t = 1.5$, projected on the comparison grid $100 \times 100 \times 10$: slope two line (blue solid line), 10 sections (magenta solid line), 20 sections (dashed line) and 30 sections (dotted-dashed line). (bottom) Corresponding droplet mass density with 10 iso-contours from 0 up to 1.44-time the maximum of the initial mass density in the fifth section : (left) Lagrangian reference solution, (right) Eulerian computation with a $400 \times 400 \times 10$ grid.

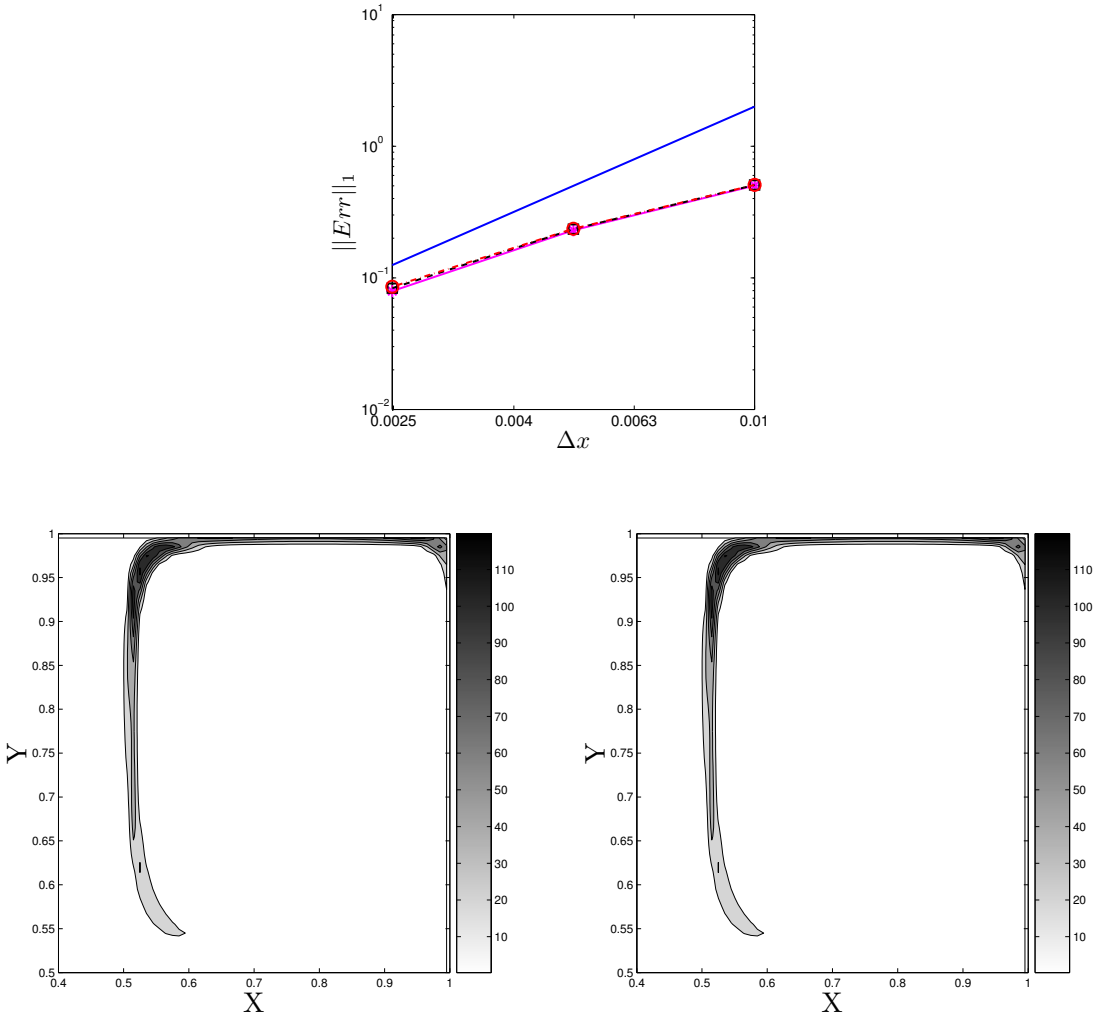

Figure 7: (top) Logarithm of L^1 norm of the error between Eulerian simulation for inertial droplets (ninth section $\mathrm{St} = 0.78\,\mathrm{St}_c$) for various Δx and the Lagrangian reference solution at time $t = 1.5$, projected on the comparison grid $100 \times 100 \times 10$: slope two line (blue solid line), 10 sections (magenta solid line), 20 sections (dashed line) and 30 sections (dotted-dashed line). (bottom) Corresponding droplet mass density with 10 iso-contours from 0 up to 2.43-time the maximum of the initial mass density in the ninth section : (left) Lagrangian reference solution, (right) Eulerian computation with a $400 \times 400 \times 10$ grid.

to first order to deal with such concentrations and associated gradients, thanks to the use of a slope limiter, as detailed in [79]. When we increase the number of points we decrease these gradients and we therefore increase the order of the method, as represented in the Figure 7.

As far as the small droplets are concerned, Figure 5, the behavior is different from the previous ones. Indeed we notice an important influence of the droplet size refinement in the rate of convergence. In this case with droplets of low inertia, the build up of the overall droplet mass density spatial gradients does not build up too strongly so that the change in order is not due to excessive gradients created by the droplet rapid ejection from the vortices; **Mal dit** nevertheless the droplet velocity is close to the gas one, but the velocity difference between spray and gas can be shown to be linear, in first approximation, with respect to the Stokes number and, thus one can guess that the velocity conditioned by droplet size is a linear function of droplet surface around zero. The assumption of the multi-fluid, explained in [79], imposes a velocity which is constant as a function of size inside a section and thus it is not able to capture this effect. Then we have to switch to 20 sections to properly predict the dynamics of droplets with very low inertia. Once refined in size, the Eulerian computation converges towards the Lagrangian reference with an order of about 2.

Both descriptions are thus presenting a very good agreement as we can see quantitatively by analyzing the error levels. The L^1 norm of the error is around a few percent for an Eulerian simulation with a $400 \times 400 \times 10$ discretization as summarized in Table 1. Such an error can be thought of as rather high. It can be explained in the following way : we have chosen to present the relative error in reference of the initial total mass introduced in the numerical simulation, we have a small amount of mass concentrated in a narrow region of the domain which gets even more concentrated due to the ejection process by the vortex and finally, we have extreme gradients in order to test the influence of the numerical diffusion of the second order in space numerical method. If, however we decided to plot the absolute error only considering that the mass density of droplets is reaching one at its maximum, we would end up with an error of about one per a thousand. Such a statement can be observed more qualitatively, plotting the iso-contours of the mass density for the three sections studied in Figures 5, 6 and 7. Dynamics of the droplet of various sizes are very well predicted, even if the chosen test case is extremely challenging and leads to the presented level of errors.

Droplet size	Global error norm $\|\|E_m^{1.5}\|\|_1$
$\mathrm{St} = 0.14\,\mathrm{St}_c$	8%
$\mathrm{St} = 0.41\,\mathrm{St}_c$	5%
$\mathrm{St} = 0.78\,\mathrm{St}_c$	8%

Table 1: Computation of $\|\|E_m^{1.5}\|\|_1$, norm of the global error at time $t = 1.5$, for the mass density of three sections of droplets in size : small droplets ($\mathrm{St} = 0.14\,\mathrm{St}_c$), medium size droplets ($\mathrm{St} = 0.41\,\mathrm{St}_c$) and inertial droplets ($\mathrm{St} = 0.78\,\mathrm{St}_c$).

Evaporating case - Our interest being in combustion applications, we perform similar comparisons in the evaporating case. In order to focus on the numerical method, the evaporation is described by a d^2 law in both Eulerian and Lagrangian descriptions . We still refer to a Lagrangian computation with 16 Million particles. We consider a low evaporation speed to preserve a relatively high number of particles in our reference computation, that is $\mathrm{E_v} = 1/15$ and $K = -1$, thus if we look at non dimensional time $t = 1.5$, 10% of the mass will be evapo-

rated. We present in this case the errors already defined for the non-evaporating case between Lagrangian and Eulerian descriptions. We study the same mesh refinements for the Eulerian method, in space as well as in size, and we study the behavior of various droplet sizes. We see

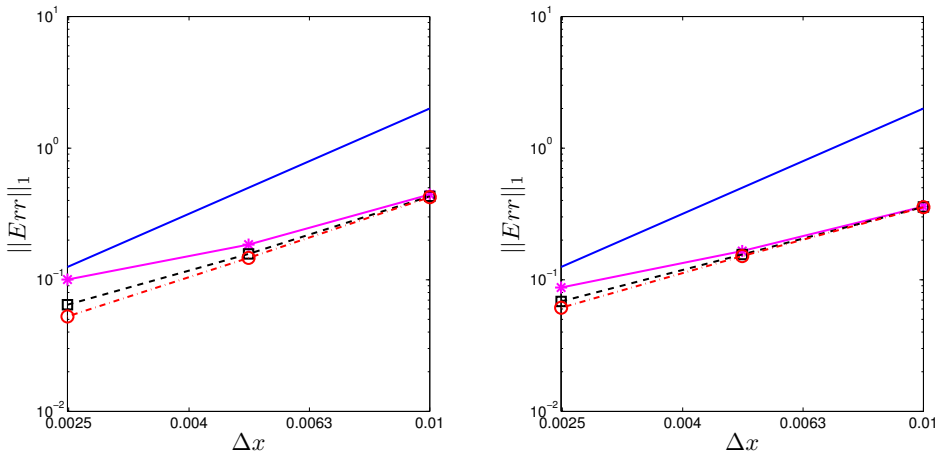

Figure 8: Logarithm of L^1 norm of the error between Eulerian simulation (left) for small droplets (second section $\mathrm{St} = 0.14\,\mathrm{St}_c$), (right) for medium size droplets (fifth section $\mathrm{St} = 0.41\,\mathrm{St}_c$) for various Δx and the Lagrangian reference solution at time $t = 1.5$, projected on the comparison grid $100 \times 100 \times 10$ in the evaporating case : slope two line (blue solid line), 10 sections (magenta solid line), 20 sections (dashed line) and 30 sections (dotted-dashed line).

in the Figure 8 that the behavior of small and medium size droplets is the same as in the non-evaporating case : the Eulerian method converges towards the Lagrangian reference solution with the expected second order. On the other hand, for the inertial droplets, the refinement in space nearly does not change the error value, only modified by the refinement in sizes, as we can see in Table 2.

$1/\Delta x$	Error 10 Sections	Error 20 Sections	Error 30 Sections
100	25%	14%	10.5%
200	25%	15%	11%
400	25%	15%	11%

Table 2: Evolution of L^1 norm of the relative error between the reference Lagrangian solution and Eulerian multi-fluid for various refinements in space and size, projected on the comparison grid $100 \times 100 \times 10$, and for inertial droplets ($\mathrm{St} = 0.78\,\mathrm{St}_c$). The results are presented at time $t = 1.5$

The multi-fluid model for evaporation is only first order accurate in the size discretization step [47]. This explains why we do not see the effect of the physical space refinement, the error being driven by the droplet size refinement. Indeed, if we plot the evolution of the error with the number of sections, as done in Figure 9, we see the same error evolution with Δs for different physical space discretizations. This drawback of the multi-fluid method was already noticed in [37] and can be partially avoided by using a second order method to describe the evaporation as

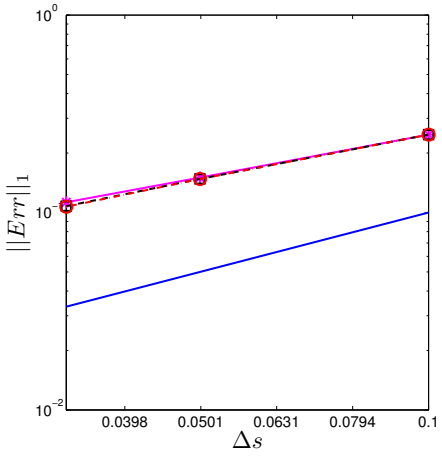

Figure 9: Logarithm of L^1 norm of the error between Eulerian simulation for inertial droplets (ninth section $\mathrm{St} = 0.78\,\mathrm{St}_c$) for various ΔS at fixed Δx and the Lagrangian reference solution at time $t = 1.5$ projected on the comparison grid $100 \times 100 \times 10$ in the evaporating case : slope one line (blue solid line), $\Delta x = 1/100$ (magenta solid line), $\Delta x = 1/200$ (dashed line) and $\Delta x = 1/400$ (dotted-dashed line).

described in [47]. These techniques are not presented in this report because new methods based on a breakthrough from classical multi-fluid have been developed [80] and yield a very efficient description of the evaporation process. As a conclusion, we have shown in both the evaporating and non-evaporating cases the ability of the multi-fluid model to accurately approximate the Lagrangian reference solution, and thus the dynamics of droplets of various sizes coupled to the evaporation process. Even if some improvement of the description of the evaporation process is to come, we can still define an equivalent level of accuracy for both descriptions and thus come up with a relevant information as far as computational cost is concerned.

3.4.2 Two-dimensional axisymmetric jets

In order to assess the Eulerian method in a more realistic configuration, we tackle a 2D axisymmetric free jet. A polydisperse spray is injected over all the core of the jet width. This test case was done with the code developed at CORIA and EM2C coupling a gas solver to a Lagrangian solver (code ASPHODELE developed at CORIA) and to an Eulerian multi-fluid solver (code MUSES3D - developped at EM2C).

Configuration - As far as the gas phase is concerned, we used a 2D axisymmetric low mach number dilatable solver. The gas jet is computed on a 400×200 grid. In order to destabilize the jet, we inject turbulence through a Klein method with 5% of fluctuations. The Reynolds number based on the geometry is 1000. We plot the results at the dimensionless time $t = 15$. The gas vorticity is presented in Figure 10. Concerning the Eulerian liquid phase, we developed a specific pressureless gas numerical scheme, for 2D axisymmetrical configuration; see [77] for the complete derivation of the numerical method. We use the same grid for the gas phase and for the Eulerian liquid phase. As far as the Lagrangian liquid phase is concerned, we decided, to be closer to industrial concern, to realize a Discrete Particle Simulation with 10000 to 40000 numerical particles depending on the cases. As mentioned in the introduction, one can see this DPS as a realization driven by steoichiometry of a statistical Lagrangian description (DMSC) and thus compare it to the Eulerian multi-fludi model, derived from a statistical spray description.

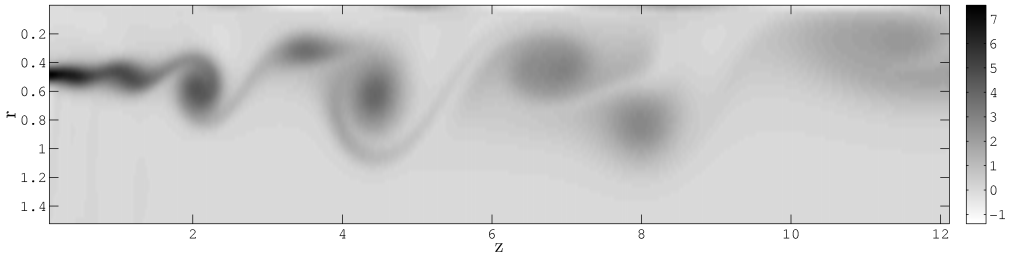

Figure 10: Gaseous vorticity at time t=15, obtained with a low mach number dilatable solver on a 400×200 grid.

In this test case we provide comparisons between the Eulerian and Lagrangian methods plotting the Lagrangian numerical particle positions versus the Eulerian number density. Thanks to the multi-fluid polydispersion resolution, we will perform the comparisons for different ranges of sizes and thus for different inertia, in the evaporating and non-evaporating cases. In order to present such comparisons, we realized, as far as the Lagrangian is concerned, a Discrete Particle Simulation with 10 000 to 40 000 particles in the computational domain depending on the cases.

Non-evaporating free jet test case - For this test case we used 5 sections for the Eulerian multi-fluid simulation. We have 40 000 Lagrangian particles in the computational domain. We first present the results for the whole spray, regardless of the droplet sizes. These results are plotted on Figure 11. The global droplets dynamics are very well reproduced by the Eulerian

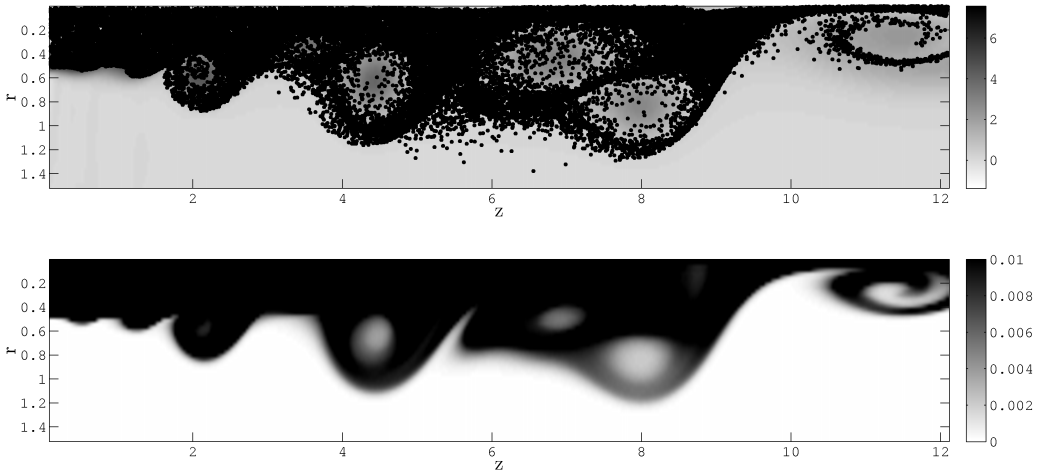

Figure 11: **Non-evaporating polydisperse spray**, Stokes 0.003 to 4.45 corresponding to diameters $d = 4\,\mu m$ to $d = 150\,\mu m$, at time t=15, : (top) Lagrangian particle positions with 40000 particles, (bottom) Eulerian total number density with a $400 \times 200 \times 5$ grid.

multi-fluid method. We move then to size-conditionned dynamics. We found a very good agreement for the droplets with low intertia, for Stokes from 0.003 to 0.18 corresponding to diameters from $4\mu m$ to $30\mu m$, as shown in Figure 12. This shows the ablity of the multi-fluid method to simulate the dynamics of a spray where few crossings occur, the droplet dynamics being close to the gas one, therefore in its validity domain. For higher Stokes number, the

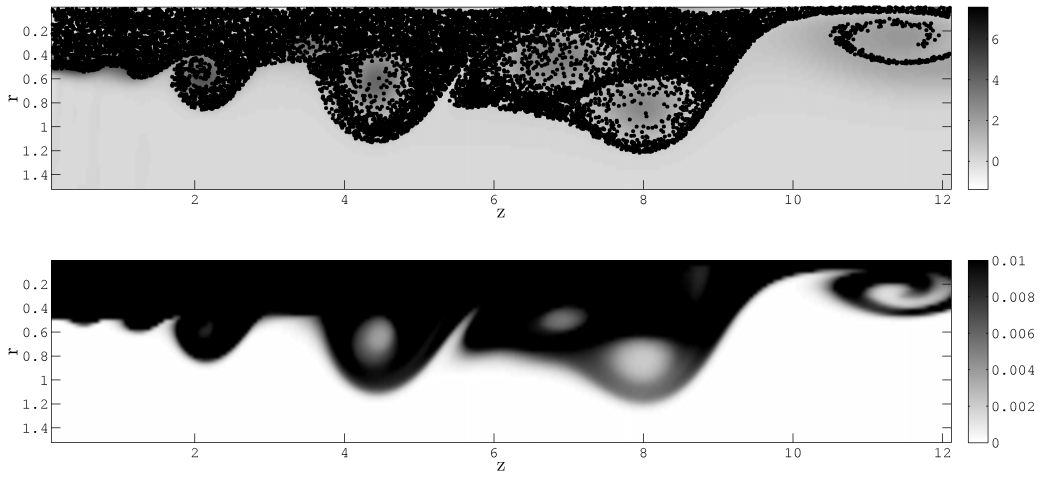

Figure 12: **Non-evaporating polydisperse spray, low inertia droplets**, Stokes 0.003 to 0.18 corresponding to diameters $d = 4\,\mu m$ to $d = 30\,\mu m$, at time t=15 : (top) Lagrangian particle positions with 40000 particles, (bottom) Eulerian number density with a $400 \times 200 \times 5$ grid.

droplets are ejected from the vortices and crossing trajectories are likely to occur, breaking the monokinetic multi-fluid assumption. Nevertheless, the dynamics is still very well reproduced for higher Stokes number. The results are plotted in Figure 13 for Stokes number from 0.71 to 4.45 corresponding to diameters from $60\,\mu m$ to $150\mu m$. One can notice that the number density is concentrated in a few cells in this case and the numerical method does not encounter any problem to capture it, illustrating again its robustness.

Evaporating free jet test case - This weakly turbulent free jet is also assessed with an evaporating spray. As in the previous test cases, we chose a simple d-square law model in order to focus on the comparisons of the numerical methods. We took then a constant splading number : $B_M = 0.1$. The results are presented the way choosen for the non-evaporating case. In order to describe correctly the evaporation process, we took 10 sections for the Eulerian multi-fluid simulation. 10 000 Lagrangian particles are present in the domain at the considered time. As in the non-evaporating case, we found a very good agreement between the Eulerian multi-fluid and the Lagrangian descriptions, see Figure 14. The size-conditionned dynamics are still very well predicted by the multi-fluid method as well for low Stokes number shown in Figure 15, as for high Stokes number shown in Figure 16.

This polydisperse evaporating axisymmetric free jet shows the ability of the multi-fluid method to treat more complex case, closer to industrial configuration. These first comparisons with Lagrangian computations show the ability of the Eulerian method to capture the size-conditionned dynamics in this case and are very encouraging. Further results conerning polydisperse spray Eulerian/Lagrangian comparisons, for example regarding gaseous fuel mass fraction, have been obtained during the last CTR Summer Programm at Stanford [50].

3.4.3 Coalescence for dense sprays in a conical nozzle

In this subsection, the break-up of the droplets is not taken into account. We want to, firstly, validate the multi-fluid model with a reference Lagrangian solver which uses an efficient and already validated stochastic algorithm for the description of droplet coalescence ([2]). We need a

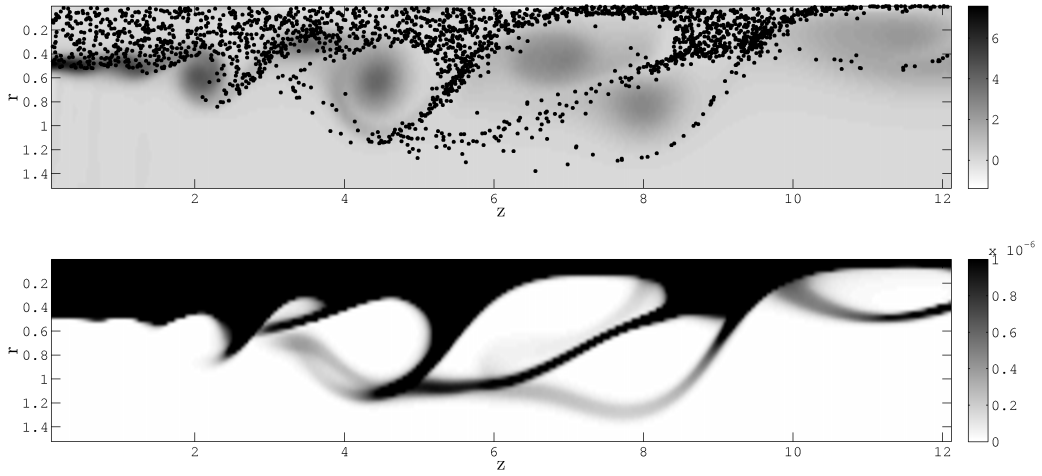

Figure 13: **Non-evaporating polydisperse spray, high inertia droplets**, Stokes 0.71 to 4.45 corresponding to diameters $d = 60\,\mu m$ to $d = 150\,\mu m$, at time t=15 : (top) Lagrangian particle positions with 40000 particles, (bottom) Eulerian total number density with a $400 \times 200 \times 5$ grid.

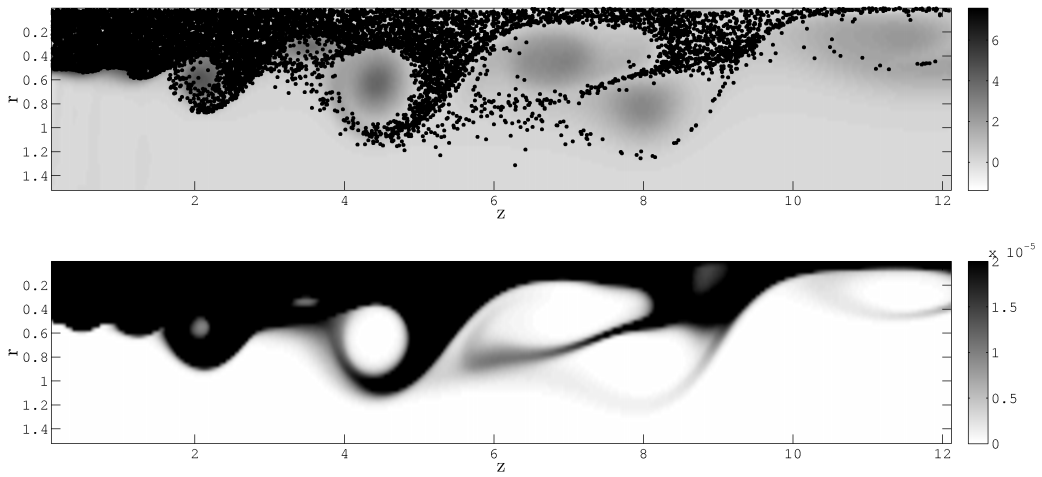

Figure 14: **Evaporating polydisperse spray**, Stokes 0.003 to 4.45 corresponding to diameters $d = 4\,\mu m$ to $d = 150\,\mu m$, at time t=15, : (top) Lagrangian particle positions with 40000 particles, (bottom) Eulerian total number density with a $400 \times 200 \times 5$ grid.

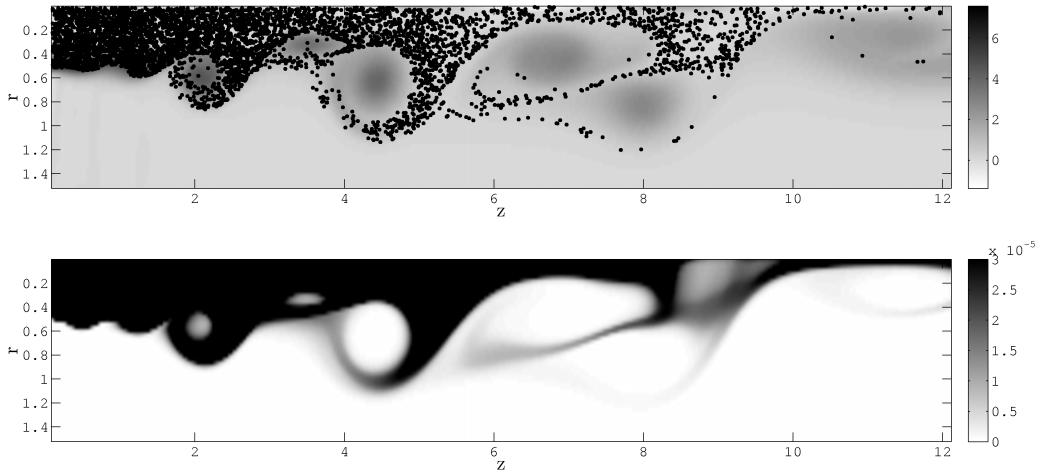

Figure 15: **Evaporating polydisperse spray, low inertia droplets**, Stokes 0.003 to 0.18 corresponding to diameters $d = 4\,\mu m$ to $d = 30\,\mu m$, at time t=15 : (top) Lagrangian particle positions with 40000 particles, (bottom) Eulerian number density with a $400 \times 200 \times 5$ grid.

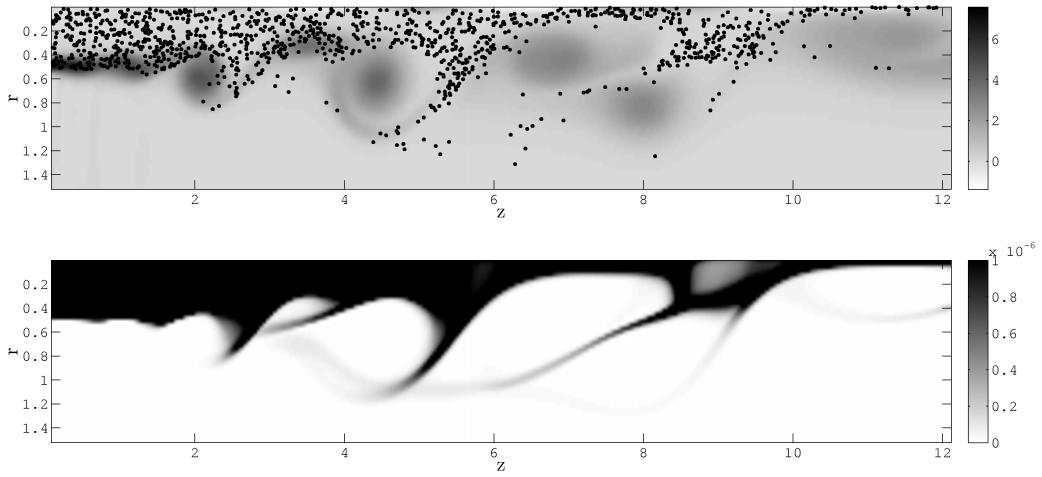

Figure 16: **Evaporating polydisperse spray, high inertia droplets**, Stokes 0.71 to 4.45 corresponding to diameters $d = 60\,\mu m$ to $d = 150\,\mu m$, at time t=15 : (top) Lagrangian particle positions with 40000 particles, (bottom) Eulerian total number density with a $400 \times 200 \times 5$ grid.

well-defined configuration, both of stationary and unstationary laminar flows where evaporation, coalescence and the dynamics of droplets of various sizes are coupled together. Secondly, we want to evaluate the validity of the assumption underlying the model and the computational efficiency of this new approach as compared to the Lagrangian solver. The chosen test-case is a decelerating self-similar 2D axisymmetrical nozzle. The deceleration generates a velocity difference between droplets of various sizes and induces coalescence. The temperature of the gas is taken high enough in order to couple the evaporation process to the coalescence one. The configuration is stationary 2D axisymmetrical in space and 1D in droplet size. It is described in detail, along with the Lagrangian solver, in [37]. Hence, only its essential characteristics are given here. The influence of the evaporation process on the gas characteristics is not taken into account in our one-way coupled calculation. It is clear that the evaporation process is going to change the composition of the gas phase and then of the evaporation itself. However, we do not attempt to achieve a fully coupled calculation, but only to compare two ways of evaluating the coupling of the dynamics, evaporation and coalescence of the droplets. It has to be emphasized that it is not restrictive in the framework of this study, which is focused on the numerical validation of Eulerian solvers for the liquid phase.

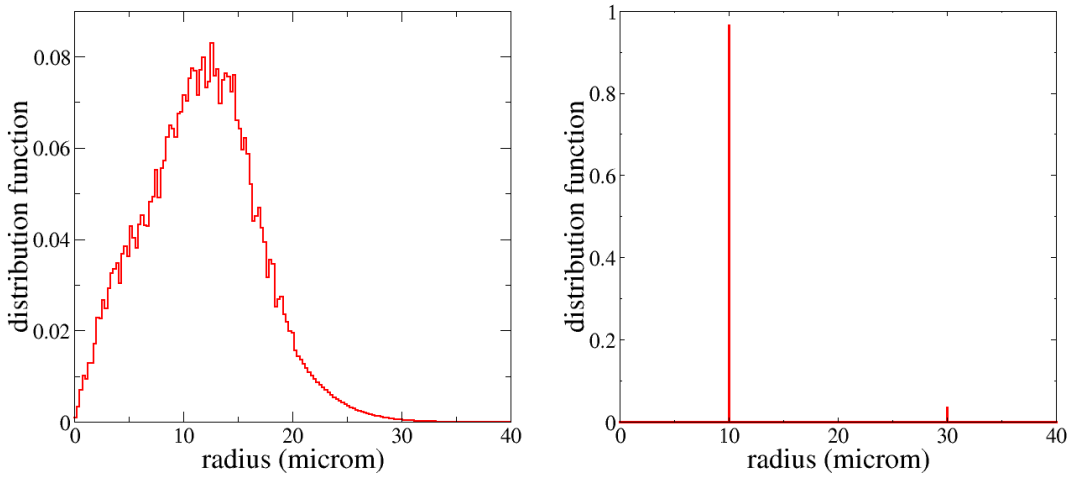

Figure 17: (left) Monomodal distribution function from experimental measurements, (right) Bimodal distribution function.

Let us finally consider two droplet distribution functions. The first one, called monomodal, is composed of droplets with radii between 0 and 35 microns, with a Sauter mean radius of 15.6 microns and a variance of $D_{10} = 24$ microns. It is represented in Figure 4 and is typical of the experimental condition reported in [48]. The droplets are only constituted of liquid heptane, their initial velocity is the one of the gas, their initial temperature, fixed at the equilibrium temperature 325.4K (corresponding to an infinite conductivity model), does not change along the trajectories. The second distribution is called bimodal since it involves only two groups of radii respectively 10 microns and 30 microns with equivalent mass density. This bimodal distribution function is typical of alumina particles in solid propergol rocket boosters ([1]). It is represented in Figure 17 and is probably the most difficult test case for an Eulerian description of the size phase space.

The initial injected mass density is then taken at $m_0 = 3.609$ mg.cm^{-3} so that the volume fraction occupied by the liquid phase is 0.57% in the stationary case. Because of the deceleration of the gas flow in the conical nozzle, droplets are going to also decelerate, however at a different

rate depending on their size and inertia. This will induce coalescence. For the problem to be one-dimensional in space, conditions for straight trajectories are used and are compatible with the assumption of an incompressible gas flow. This leads to the following expression for the gaseous axial velocity U_z and the reduced radial velocity U_r/r:

$$U_z = V(z) = \frac{z_0^2 V(z_0)}{z^2}, \quad \frac{U_r}{r} = \frac{V(z)}{z} = \frac{z_0^2 V(z_0)}{z^3} \quad \text{for } z \geq z_0 \tag{43}$$

where $z_0 > 0$ is the coordinate of the nozzle entrance and the axial velocity $V(z_0)$ at the entrance is fixed. The trajectories of the droplets are also assumed straight since their injection velocity is co-linear to the one of the gas. This assumption is only valid when no coalescence occurs. However, even in the presence of coalescence, it is valid in the neighborhood of the centerline. The deceleration at the entrance of the nozzle is taken at $a(z_0) = -2V(z_0)/z_0$; it is chosen large enough so that the velocity difference developed by the various sizes of droplet is important. In the stationary configuration, we have chosen a very large value as well as a strong deceleration leading to extreme cases : $V(z_0) = 5$m/s, $z_0 = 10$cm for the monomodal case and $V(z_0) = 5$m/s, $z_0 = 5$cm for the bimodal case. It generates a very strong coupling of coalescence and dynamics and induces an important effect on the evaporation process.

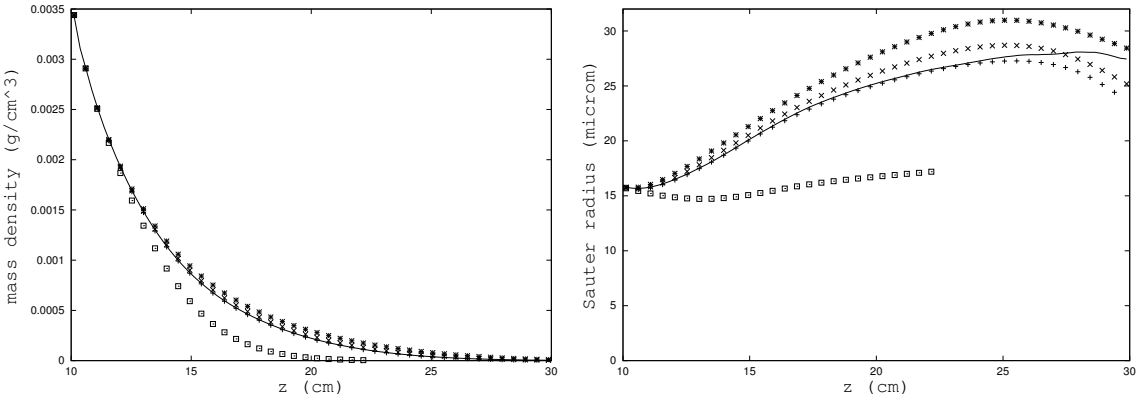

Figure 18: (left) Evolution of the mass density of liquid for the Lagrangian reference solution (solid line) and for various discretizations with the Eulerian multi-fluid model (+ : 90 sections, × : 30 section, ∗ : 15 sections, □ : 90 sections without collision). (right) Sauter mean radius for the Lagrangian reference solution (solid line) and for various discretizations with the Eulerian multi-fluid model (+ : 90 sections, × : 30 section, ∗ : 15 sections, □ : 90 sections without collision).

As mentioned previously, the strength of such multi-fluid models, is to be able to reproduce the global behavior of the spray with a limited number of sections. Consequently, calculations with various numbers of sections were performed : 90, 60, 30 and 15. For completeness, we have also represented, both in Figure 18 left and right, the solution without coalescence calculated with 90 sections. The conclusion to be drawn from these figures is that the multi-fluid is able to predict fairly well, even in the case of 15 sections for which the computational cost is very reasonable, the global coupling of the various phenomena occurring in the nozzle. One crucial point is related to the localization of the evaporation front for pollutant formation purposes and even with 15 sections, the evaporation front is precisely computed.

It is particularly interesting to note that the average dynamics are correctly reproduced with 90 sections. Concerning the Sauter mean radius of the distribution, it is extremely well-predicted by the 90 section solution, fairly well-reproduced by the 30 section one and the difference gets bigger when we use 15 sections, even if the mass difference does not grow beyond two percent of the initial one.

If the monomodal distribution is well-suited for the Eulerian multi-fluid approach, the bimodal one can be considered as the most difficult task; the method can be shown to be of first order in the size discretization step [47]. In such a situation, the numerical diffusion is introducing some artificial coupling at the dynamical level since only one velocity is prescribed per section.

However, the results presented in Figure 19 show that the mass evolution is very well captured, the difference with the reference solution stays below 1%. The evolution of the Sauter mean radius in Figure 19-right is also well-captured. However, once 93% of the initial mass has evaporated, there is a little difference in the mass density decrease which seems to be due to a difficulty to correctly reproduce the dynamics and size distribution of the spray.

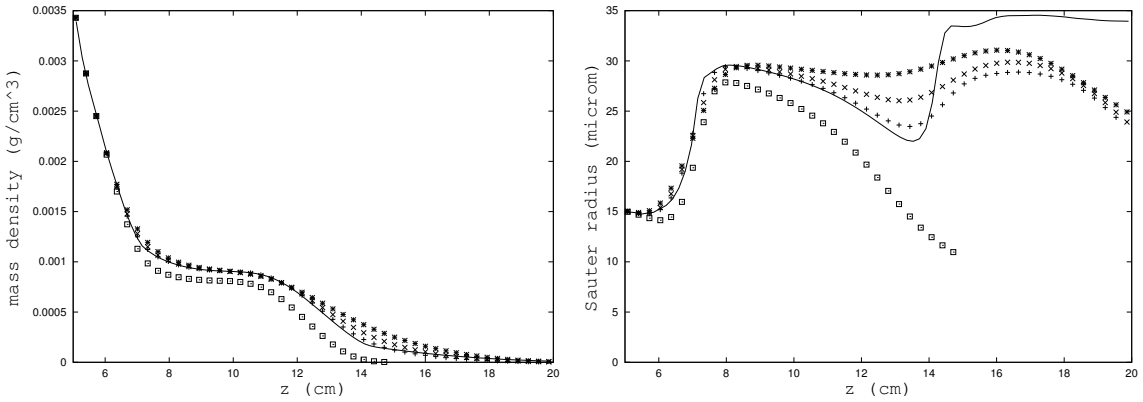

Figure 19: (left) Evolution of the mass density of liquid for the Lagrangian reference solution (solid line) and for various discretizations with the Eulerian multi-fluid model (+ : 100 se ctions, × : 50 section, ∗ : 25 sections, □ : 100 sections without collision). (right) Sauter mean radius for the Lagrangian reference solution (solid line) and for various discretizations with the Eulerian multi-fluid model (+ : 100 sections, × : 50 section, ∗ : 25 sections, □ : 100 sections without collision).

In order to have a more precise idea of what is happening, we have observed the mass distribution function at the point $z = 10.53$ cm as well as the velocity distribution as a function of the droplet size at this point. It appears very clearly that the numerical diffusion, if too high, can smooth out the mass distribution function and consequently the velocity distribution function because of the assumption, the Eulerian multi-fluid model relies on. In the 25 sections case, the peaks of the distribution have disappeared and the velocity distribution function has become monotone. This example allows to understand what will be the limits of such an approach. However, the simulation with 100 sections allows to predict very accurately the various peaks of the mass distribution function, as well as their dynamics, except for the very "big" droplets, the velocity of which is becoming higher thus causing the difference to be observed in Figure 19-right on the Sauter mean radius. This discrepancy can be attributed to the numerical diffusion ([47]) which acts on a size distribution function which is very singular and remains so through the coalescence phenomenon.

The computational efficiency of the model is presented in details in [37] where an unsteady series of computations are conducted in a challenging configuration for both Eulerian and Lagrangian methods. If a good level of accuracy in the size phase space is required, the cost is lower than the Lagrangian method but not much lower thus showing that, in such a case, the improvement through the use of the Eulerian model is going to be achieved with the optimization of the solver coupling the two Eulerian description. However, the Eulerian model is going to allow the user to perform several levels of accuracy for the size phase space discretization without having

any trouble with the smoothness of the calculated solution (an essential point for combustion applications), a feature which is not present with the Lagrangian solver. We show that a coarse discretization allows to obtain a good qualitative description of the phenomenon; it proves to be very computationally efficient compared to the reference Lagrangian solution and still allows to take into account the polydisperse character of the spray. The level of code optimization that can be obtained from a global Eulerian description has already been demonstrated in the case of two-fluid models, but the detailed study in the framework of Eulerian multi-fluid models is in progress and beyond the scope of the present paper. Finally, the assumption that the velocity dispersion around its mean at a given time, for a given space location and a given droplet size is zero, the Eulerian multi-fluid model relies on, is investigated by considering the results from the Lagrangian solver and we prove that this assumption is fullfilled.

We then have validated the Eulerian multi-fluid model by showing the good correspondence with the reference solution when the size phase space is finely discretized. It is also shown that the behavior of the spray is correctly captured even if a limited number of "fluids" is used for the Eulerian model corresponding to a coarser discretization in the size phase space.

4 Beyond the original limitations : higher order methods

The multi-fluid model, presented in Section 3, is a fully Eulerian model describing the disperse liquid phase while preserving the link with the kinetic level of description. It is able to capture the polydispersion of evaporating sprays, and the dynamics of the evaporating droplets conditioned by size. It represents a good alternative to Lagrangian models when it comes to simulate polydispersion. However, the multi-fluid model faces two important limitations. The first one lies in the order in size in a section of the method. In [39], Dufour has devised a second order multi-fluid model, no one has gone further for a multi-fluid model. There is a theorical as well as a practical interest in going beyond this limit. From a mathematical point of vue, there is a challenge in devising a more powerful model to combine the sectional approach with a high order description of the distribution function in each section. Moreover, for industrial purposes, it can be sometimes impossible to increase the number of sections to reach a better accuracy for polydispersion, as the computational cost can turn out to be too important. Therefore, there is a need to obtain a high accuracy with a reduced number of sections (2 or 3), or even just with one section, to be able to describe polydispersion in a two-fluid formalism.

The second limitation, mentioned in Section 3.2, concerns the droplets dynamics. It has been shown (see Section 3.2 or [81] and references therein) that the semi-kinetic model, from which the multi-fluid model is derived by a discretization in size, is equivalent to the kinetic description in the case of small Stokes numbers. For particles beyond a critical Stokes number, some characteristic curves cross each other in the diagram (x, t). The distribution ceases to be mono-kinetic and the equivalence between the macroscopic and kinetic descriptions is not valid any more. Our aim is to be able to simulate these droplet crossings for high Stokes number particles.

High order moment methods are used to address these two issues. High order size moments are considered for the description of polydispersion, in the context of evaporation, and transport of particles with their own velocity. The property of the equation system as well as the mathematical and numerical tools to insure the system stability are provided. When it comes to the simulation of charateristic crossing, high order velocity moments are considered. We first consider a monodisperse flow and show how to close the system with QMOM in the spirit of [82]. In a third part, both the aforementioned models are coupled in a model describing polydispersion and droplet crossing in the context of an evaporating spray. The fourth part is dedicated to results and validation.

4.1 Multi-Moment transport and evaporation

The starting point is the semi-kinetic equations (11,12). In this part, our purpose is to explain high order moment methods for the description of polydispersion in the context of evaporation and transport. Notice that it is not a restrictive condition. Indeed, because each operator (transport, evaporation, drag) has its own structure, different from the other, we use a Strang splitting algorithm, as explained in Section 3.3. The semi-kinetic equation system of interest writes :

$$\partial_t n + \partial_{\mathbf{x}}(n\bar{\mathbf{u}}) + \partial_s(nR_s) = 0 \tag{44}$$

$$\partial_t(n\,\bar{\mathbf{u}}) + \partial_{\mathbf{x}}(n\,\bar{\mathbf{u}}\otimes\bar{\mathbf{u}}) + \partial_s(n\,R_s\bar{\mathbf{u}}) - \overline{\mathbf{F}} = 0. \tag{45}$$

In the manner of the multi-fluid model, we apply a finite volume discretization in the size variable, averaging the semi-kinetic system of conservation equations over some fixed size intervals. We make the same assumptions on the spray distribution function : $f(t,\mathbf{x},s,\mathbf{u}) = n(t,\mathbf{x},s)\,\delta(\mathbf{u}-\bar{\mathbf{u}}(t,\mathbf{x},s))$. The evaporation process is described by a d^2 law. The fundamental difference is that we consider $N+1$ size moments of the distribution function for each section, from the 0^{th} to the $(N-1)^{th}$ moment. A size moment is defined by : $m_i^{(k)} = \int_{s_{k-1}}^{s_k} s^i n\,\mathrm{d}v$, where $[s_{k-1}, s_k]$ is the k^{th} section.

The equation system reads, for the k^{th} section :

$$\begin{aligned}
\partial_t m_0^{(k)} + \partial_{\mathbf{x}}\left(m_0^{(k)}\bar{\mathbf{u}}^{(k)}\right) &= R_s n^{(k)}(s_{k-1}) - R_s n^{(k+1)}(s_k),\\
\partial_t m_1^{(k)} + \partial_{\mathbf{x}}\left(m_1^{(k)}\bar{\mathbf{u}}^{(k)}\right) &= R_s m_0^{(k)} + R_s s_{k-1} n^{(k)}(s_{k-1}) - R_s s_k n^{(k+1)}(s_k),\\
\partial_t m_2^{(k)} + \partial_{\mathbf{x}}\left(m_2^{(k)}\bar{\mathbf{u}}^{(k)}\right) &= 2R_s m_1^{(k)} + R_s s_{k-1}^2 n^{(k)}(s_{k-1}) - R_s s_k^2 n^{(k+1)}(s_k),\\
&\vdots\\
\partial_t m_N^{(k)} + \partial_{\mathbf{x}}\left(m_N^{(k)}\bar{\mathbf{u}}^{(k)}\right) &= N R_s m_{N-1}^{(k)} + R_s s_{k-1}^{N-1} n^{(k)}(s_{k-1}) - R_s s_k^{N-1} n^{(k+1)}(s_k),\\
\partial_t\left(m_0^{(k)}\bar{\mathbf{u}}\right) + \partial_{\mathbf{x}}\left(m_0^{(k)}\bar{\mathbf{u}}^{(k)}\otimes\bar{\mathbf{u}}^{(k)}\right) &= R_s n^{(k)}(s_{k-1})\bar{\mathbf{u}}^{(k)} - R_s n^{(k+1)}(s_k)\bar{\mathbf{u}}^{(k+1)},
\end{aligned} \tag{46}$$

where the dependance in $(t,\mathbf{x})$ of each variable is implicit.

The description of polydispersion is enriched here by working with four moments, whereas the multi-fluid model only considers the mass moment $m^{(k)}$. High order reconstruction in size is now possible, and polydispersion can be accounted for within only one section, which is not possible with the multi-fluid model. However, with the introduction of a moment vector of a distribution function $\boldsymbol{m}_N^{(k)} = (m_0^{(k)},\cdots,m_{N-1}^{(k)})^t$, we are to face a major issue consisting in keeping the integrity of the moment sequence $\boldsymbol{m}_N^{(k)}$, in either the evaporation and the transport steps. Indeed, [83] showed that independent transport of moments with algorithms of order greater than one in space, can result in the generation of invalid moment sets. That means that there is no distribution function $n(s)$ which can be reconstructed from the moment sequence such as $\int_{s_{k-1}}^{s_k} s^i n(s)\,ds = m_i^{(k)}$. Vectors which verifies this condition belong to the moment space, denoted by $\mathcal{M}_N$. What makes it difficult to preserve is the fact that not all the vectors of $\mathbb{R}^N$ belong to the moment space.

To study some interesting properties of the moment space in order to preserve it, let us introduce some quantities derived from the moments : the normalized moments and the canonical moments. We define normalized moments as follows :

$$c_i = \frac{m_i}{m_0} \tag{47}$$

where m_0 is the total number density of particles. The vector $\mathbf{c}_N = (c_1, \ldots, c_N)^t$ is the vector of normalized moments of the distribution function. For $\mathbf{c}_N \in \mathcal{M}_N$, we denote by $P(\mathbf{c}_N)$ the set of all mesures $\mu \in P$ with moments up to the order N equal to $\mathbf{c}_N$, and

$$c_{N+1}^+(\mathbf{c}_N) = \max_{\mu \in P(\mathbf{c}_N)} c_{N+1}(\mu), \;\; c_{N+1}^-(\mathbf{c}_N) = \min_{\mu \in P(\mathbf{c}_N)} c_{N+1}(\mu) \tag{48}$$

If $\mathbf{c}_N$ belongs to the interior of $\mathcal{M}_N$, then $c_i^- < c_i^+$ for all $i \leq N+1$ and $P(\mathbf{c}_N)$ is infinite [84]. A canonical moment sequence $(p_i)_{i \leq N+1}$ can then be defined by :

$$p_i = \frac{c_i - c_i^-(\mathbf{c}_{i-1})}{c_i^+(\mathbf{c}_{i-1}) - c_i^-(\mathbf{c}_{i-1})} \tag{49}$$

The algorithm to find the canonical moment from the moment can be found in [84]. The expression of the first canonical moment can be found in [80]. The canonical moments have two major properties which make them attractive to work with. First, according to the definition (49), each canonical moment of a moment vector belonging to the interior of $\mathcal{M}_N$ independently lies in the interval $]0,1[$. And if, for a certain value of i, $p_i = 0$ or 1, then $\forall j > i$, the canonical moments are not defined, and the distribution is a sum of Dirac distributions. It is thus immediate to figure out if a canonical moment set belongs to the moment space. Secondly, the canonical moments remain invariant under linear transformation of the distribution, i.e $\forall i \geq 1, p_i(f) = p_i(f_{s_{k-1},s_k})$, where f_{s_{k-1},s_k} denotes the distribution induced by the linear transformation $s = s_{k-1} + (s_k - s_{k-1})x$ of $[0,1]$ onto $[s_{k-1}, s_k]$ (refer to [84] for proof). That is the reason why we can work on the size interval $[0,1]$ without loss of generality.

System (46) is split into two systems, for transport in phase space (evaporation) and transport in physical space.

4.1.1 Evaporation

We present the evaporation system in the simple case where $R_s = -1$. We extract the equations on size moments of system (46), the equation on momentum being solved in a second time. The evolution of the system through evaporation reads :

$$\mathrm{d}_t \boldsymbol{m}_N^{(k)} = -A\boldsymbol{m}_N^{(k)} - \phi_- + \phi_+ \tag{50}$$

$$\boldsymbol{m}_N^{(k)} = \begin{pmatrix} m_0^{(k)} \\ \vdots \\ m_N^{(k)} \end{pmatrix}, \qquad A = \begin{bmatrix} 0 & & & & 0 \\ 1 & 0 & & & \\ & 2 & \ddots & & \\ & & \ddots & \ddots & \\ 0 & & & N & 0 \end{bmatrix}. \tag{51}$$

$$\phi_- = n^{(k)}(t, \mathbf{x}, s_{k-1})(1, s_{k-1}, \ldots, s_{k-1}^N)^t \qquad \phi_+ = n^{(k+1)}(t, \mathbf{x}, s_k)(1, s_k, \ldots, s_k^N)^t \tag{52}$$

The terms $n(t, \mathbf{x}, s_{k-1})$ and $n(t, \mathbf{x}, s_k)$ have to be closed in system (50). They represent the disappearing flux of droplets at time t for each section. The difficulty is that a pointwise value of the distribution function must be found from the data of its N first moments. Moreover, this closure has to preserve the moment space. This is a modeling as well as a numerical issue. Indeed, once a value of n which makes system (50) stable (i.e staying in the moment space) has been determined, the numerical scheme has to preserve this stability. Finding these values amounts to solve the finite Hausdorff moment problem [84] in each section. A closure preserving the moment space is provided using an Entropy Maximisation of the moments [85].

When it comes to the numerical scheme, a pointwise definition of the flux is difficult to evaluate. In [80], some solvers are used for system (50), and all prove to be instable. In order to avoid these instabilities, we construct, like in the kinetic schemes for hyperbolic equations, an integral formulation making use of the underlying kinetic equation. The integral formulation of system (50) reads (the proof can be found in [80]) :

$$\exp(\Delta t\, A)\, \left(\boldsymbol{m}_N^{(k)}\right)^{n+1} = \left(\boldsymbol{m}_N^{(k)}\right)^{n} + \Phi^{(k+1)} - \Phi^{(k)} \tag{53}$$

where

$$\Phi^{(k)} = \int_{s_{k-1}}^{s_{k-1}+\Delta t} n^{(k)}(0, \mathbf{x}, \beta)(1, \beta, \ldots, \beta^N)^t \mathrm{d}\beta \tag{54}$$

Since the following result holds :

$$\exp(t\, A) \begin{pmatrix} \sum_{i=1}^n \omega_\alpha(t) \\ \sum_{i=1}^n \omega_\alpha(t)\, \mathcal{S}_\alpha(t) \\ \vdots \\ \sum_{i=1}^n \omega_\alpha(t)\, \mathcal{S}_\alpha^N(t) \end{pmatrix} = \begin{pmatrix} \sum_{i=1}^n \omega_\alpha(t) \\ \sum_{i=1}^n \omega_\alpha(t)(\mathcal{S}_\alpha(t) + t) \\ \vdots \\ \sum_{i=1}^n \omega_\alpha(t)(\mathcal{S}_\alpha^N(t) + t) \end{pmatrix}, \tag{55}$$

an algorithm using a quadrature is given in three steps in order to compute moments at time $n+1$, which guaranties the conservation of the moment space [80] :

1. In each section $[s_{k-1}, s_k]$, a reconstruction $n^{(k)}$ is done of the distribution from its moments $\left(\boldsymbol{m}_N^{(k)}\right)^n$ by the Maximum Entropy method and the fluxes $\Phi^{(k)}$ are computed by Equation (54).
2. The weights $\omega_\alpha^{(k)}$ and the abscissas $\mathcal{S}_\alpha^{(k)}$, $\alpha \leq 2$, corresponding to the moment vector $\left(\boldsymbol{m}_N^{(k)}\right)^n + \Phi^{(k+1)} - \Phi^{(k)}$ are computed using the QD algorithm.
3. The moments $\left(\boldsymbol{m}_N^{(k)}\right)^{n+1}$ corresponding to the weights $\omega_\alpha^{(k)}$ and the abscissas $\mathcal{S}_\alpha^{(k)} - \Delta t$ are computed.

The updated momentum $m_N^{(k)} \bar{\mathbf{u}}^{(k)}(t^{n+1})$ is then given by :

$$\left(m_N^{(k)} \bar{\mathbf{u}}^{(k)}\right)^{n+1} = \left(m_N^{(k)} \bar{\mathbf{u}}^{(k)}\right)^{n} + \Phi^{(k+1)} \left(\bar{\mathbf{u}}^{(k+1)}\right)^n - \Phi^{(k)} \left(\bar{\mathbf{u}}^{(k)}\right)^n \tag{56}$$

Under the CFL like condition $\Delta t < \Delta s$, this scheme is stable. Such a method has the major advantage, with a very moderate cost, to preserve the moment vector in the singular transport equation with a very stable model for the flux of disapearing droplets. A modification of this algorithm in order to take into account of a more general evaporation law is given in [80].

4.1.2 Transport

The equation system for transport in physical space writes :

$$\begin{aligned} \partial_t m_0^{(k)} + \partial_{\mathbf{x}} \left(m_0^{(k)} \bar{\mathbf{u}}^{(k)}\right) &= 0 \\ \partial_t m_1^{(k)} + \partial_{\mathbf{x}} \left(m_1^{(k)} \bar{\mathbf{u}}^{(k)}\right) &= 0 \\ &\vdots \\ \partial_t m_N^{(k)} + \partial_{\mathbf{x}} \left(m_N^{(k)} \bar{\mathbf{u}}^{(k)}\right) &= 0 \\ \partial_t \left(m_0^{(k)} \bar{\mathbf{u}}^{(k)}\right) + \partial_{\mathbf{x}} \left(m_0^{(k)} \bar{\mathbf{u}}^{(k)} \otimes \bar{\mathbf{u}}^{(k)}\right) &= 0 \end{aligned} \tag{57}$$

This system is already closed. It presents two mathematical issues, the first one being, like in the evaporation step, the preservation of the moment space, and the second one being the pressureless gas formalism explained in Section 3.2. First order schemes are relatively easy to design, provided a time integrated and kinetic based expression for the fluxes in a finite volume formulation. Under CFL condition, this scheme is stable as the updates of the mean values of the moment sets results in a convex some between moment sets of neighboring cells, preserving the moment space which is convex. But our purpose is to design a second order in space and time numerical scheme able to cope with the aformentioned issues. The capacity to build such a scheme limiting diffusion has been a key concern in every field where the modeling work considers the transport of a moment set. It has been a stumbling block for a long time, because conservative transport scheme only guarantees that individual tracers remain positive and conserved. The link between the different moments, with their generally different spatial gradients, is not guaranteed when these are transported separately like chemical species, and thus the moment space is not sure to be preserved. When this is the case, no distribution can be reconstructed from the moment set. The scheme we present has the property to preserve the moment space by itself, i.e just using any extra algorithm.

A key propriety of system (57) is that canonical moments are tranported quantities, which means that they verify the transport equation : $\partial_t p_i + \bar{\mathbf{u}}\partial_{\mathbf{x}} p_i = 0$. Their support is invariant during a timestep. As the canonical moments are independently bounded by 0 and 1, satisfying maximum principles on the canonical moments will insure the robustness of the scheme towards the preservation of the moment space.

Because of the conservative form of system (57), the finite volume method [86] is a natural candidate for its discretization. As we use a dimensional splitting algorithm, we alternatively transport in each space direction with a one-dimensional scheme. As system (57) contains the pressureless gaz formalism, we use the equivalence between the microscopic and the macroscopic levels of description as detailed in Section 3.3.2. However, we have an extended structure for the distribution function which reads : $f(t,x,s,u) = n(t,x,s)\delta(u-\bar{u})$, where n represents the size distribution function.In the following, we omit the exponent refering to the size section, as there is no interaction between the sections.
In the projection step, we can express the moments according to the NDF with the following expression:

$$\begin{pmatrix} m_0(x) \\ \vdots \\ m_{N-1}(x) \\ q \end{pmatrix} = \int_{\mathbb{R}} \int_0^1 \begin{pmatrix} 1 \\ \vdots \\ s^{N-1} \\ u \end{pmatrix} f(t,x,s,u)\,\mathrm{d}s\mathrm{d}u \tag{58}$$

where q represents the momentum, $q = m_0\bar{\mathbf{u}}$.

attention, expliquer pourquoi on se place sur [0,1]!!!

The algorithm of the scheme is the same as exposed in Section 3.3.2. We first consider the mean values of the moments in a cell, which are obtained the same way as in (37). Then, at time $t = t^n$, the distribution function $f^n(x,s,u)$ is reconstructed from the average value of the moments.
The discretized equations are obtained in a conservative form by integrating the kinetic equation over $(t^n, t^{n+1}) \times (x_{j-1/2}, x_{j+1/2}) \times \mathbb{R} \times (0,1)$:

$$U_j^{n+1} = U_j^n - \frac{\Delta t}{\Delta x}(F_{j+1/2} - F_{j-1/2}) \tag{59}$$

where $U_j = (m_{0,j}, \ldots, m_{N-1,j}, q_j)^t$ and $F_{j+1/2}$ is the flux vector and writes :

$$F_{j+1/2} = \frac{1}{\Delta t}\int_0^{\Delta t}\int_{\mathbb{R}}\int_0^1 \begin{pmatrix} 1 \\ s \\ \vdots \\ s^{N-1} \end{pmatrix} u f^n(x_{j+1/2} - u\Delta t, u, s)\,\mathrm{d}s\mathrm{d}u\mathrm{d}t \tag{60}$$

$$\tag{61}$$

$$\tag{62}$$

In addition, one can compute the integrals over $\mathbb{R}^+$ and $\mathbb{R}^-$ separately, and then the numerical flux can be written in the flux vector splitting form: $F_{j+1/2} = F^+_{j+1/2} + F^-_{j+1/2}$, with

$$F^{\pm}_{j+1/2} = \frac{1}{\Delta t}\int_0^{\Delta t}\int_{\pm u\geq 0}\int_{s_{k-1}}^{s_k} \begin{pmatrix} 1 \\ s \\ \vdots \\ s^{N-1} \end{pmatrix} u f^n(x_{j+1/2} - u\Delta t, u, s)\,\mathrm{d}s\mathrm{d}u\mathrm{d}t \tag{63}$$

In order to compute the flux, and as we aim to devise a second order scheme, we use a linear reconstruction. Whereas the choice of m_0 (droplet number) and $\bar{u}$ for reconstructed variables are classical, the other reconstructed variables are the canonical moments. The normalized moments are not reconstructed, as their independant reconstruction does not guarantee to preserve the moment space, contrary to the canonical moment for which a sufficient condition is to lie between 0 and 1 to preserve the moment space. The reconstructions are performed in order that the scheme is conservative. Morevover, slope limiters are introduced in order to respect the positivity of m_0 and the maximum principle of the other variables.

In the following, we choose $N = 3$ (four size moments) in order not to get too heavy expressions. The expression of $F^+_{j+1/2}$, after having used the fact that f is solution of the kinetic equation, takes the final form:

$$F^+_{j+1/2} = \frac{1}{\Delta t}\int_{x^L_{j+1/2}}^{x_{j+1/2}} \begin{pmatrix} m_0^n(x) \\ m_0^n(x)p_1(x) \\ m_0^n(x)p_1[(1-p_1)p_2 + p_1](x) \\ m_0^n(x)p_1[(1-p_1)p_2(1-p_2)p_3 + (p_1 + p_2(1-p_1))^2](x) \end{pmatrix} \mathrm{d}x \tag{64}$$

$x^L_{j+1/2}$ is the abscissa of the last particle reaching the interface at time t^{n+1}.

Using limiters to satisfy a maximum principle on the canonical moments enables to satisfy the realizability condition on the moments at every point of the reonstruction. We have to satisfy a maximum principle as well for velocity, and also a non overlapping condition to get an explicit expression for the fluxes, when we consider inertial particles. Providing a solution to these difficulties leads to a second order in space and time scheme able to advect a moment set preserving the moment space, and supporting singularities when inertial particles are studied. Notice that we do not use any extra algorithm in order to constrain the moment set to a subspace of the moment space as in [83] or [87].

4.2 Quadrature methods for finite Stokes particle : the issue of droplet crossing

In this section, we tackle the second limitation of the multi-fluid model : as particle characteristics cross each other in the diagram (x, t), the equivalence between semi-kinetic and kinetic

description is lost. This not a concern for particles with a small Stokes number (St << 1), as they follow gas molecules trajectories and do not cross. But this is a problem when it comes to finite Stokes particles as they have their own velocity, different from the gas velocity, and are likely to cross each other. Moreover, there are two types of flow regimes depending on the particle Knudsen number. In the dense limit (or Euler limit, for let us say Kn < 0.01), the particles are described by the Euler (when the distribution funtion is a Maxwell-Boltzmann distribution) or Navier-Stokes equations (when perturbations around the Maxwell-Boltzmann distribution are applied for the distribution function). These methods only consider the dynamic of low order (velocity) moments, as the higher order moments are closed since the distribution function is supposed to be an equilibrium distribution. One the other hand, in the case of high Knudsen numbers, the collision rate between particles is too weak to make the distribution function relax to an equilibrium distribution. Thus, no moments are known and equations on high order moments of the kinetic equation are written. In our work , we consider a dilute particle flow in the limit of infinite Knudsen number, so we assume that there is no collision among the particles.

Our purpose here is to explain how this limitation of the multi-fluid model can be overcome, using a high order moment method for velocity moments, combined with Quadrature Method of Moment (QMOM), from the ideas of [82]. A key component of QMOM is the inversion algorithm used to find the weights and abscissas from the moments. A direct non linear solver is poorly conditionned (and gat worse increasing N, the number of moments considered). However, the product-difference (PD) algorithm introduced by McGraw [28] overcomes this difficulty by replacing the nonlinear solver with a computationally efficient eigenvalue-eigenvector problem that is well conditioned even for large N. Besides, even with highly coupled and nonlinear aggregation kernels, good accuracy for the lower-order moments can usually be attained with $N = 4$ nodes [29]. Unfortunately, the PD algorithm only works for uni-variate distribution functions, but not for bi-variate (or higher) NDF where $f(\xi, \eta)$ depends on two (or more) internal coordinates. In order to overcome this limitation, one can work directly with transport equations for the weights and abscissas (DQMOM [88]), which works well when ξ, η represent passive scalars. However, for velocity moments, the DQMOM approach is unstable: in particular it fails at singular points where the velocity abscissas change discontinuously. Remarkably, a quadrature-based moment closure for the velocity distribution function is robust at such points [89]. However, for multi-dimensional velocity distributions, the key challenge of inverting the moments to find the weights and velocity abscissas remains.

In this chapter we investigate moment inversion in succesively one and two dimensions in physical. The internal variable of the distribution function are suppposed to be velocity only. Let us emphasize the fact that we consider, in this section, a monodisperse distribution, and that we are interested in the convection operator. Our starting point is the kinetic equation (26), where we omit the evaporation term.

4.2.1 One-dimensionnal case

Let us first begin with the one dimensional case. The first step is to take the N first velocity moments of the kinetic equation : $m_0 M_k = \int u^k f(t, x, u)\, \mathrm{d}u$. We consider actually the normalized velocity moments M_k. Like in the previous chapter, we set $N = 3$. The dynamic system on the velocity moments then reads :

$$\partial_t W + \partial_x F(W) = 0 \tag{65}$$

where $W = (m_0, m_0 M_1, m_0 M_2, m_0 M_3)^t$, $F(W) = (m_0 M_1, m_0 M_2, m_0 M_3, m_0 M_4)^t$. We focus on the transport operator. This is not a restrictive hypothesis as we use a splitting algorithm to

compute each operator.
System (65) has an unclosed term : M_4, which is determined by the following expression

$$M_4 = n_1 u_1^4 + n_2 u_2^4 \tag{66}$$

where $(n_1, u_1), (n_2, u_2)$ are the weights and abscissas given by the quadrature of the components of W, solution of the system

$$\begin{aligned} M_0 &= n_1 + n_2 \\ M_1 &= n_1 u_1 + n_2 u_2 \\ M_2 &= n_1 u_1^2 + n_2 u_2^2 \\ M_3 &= n_1 u_1^3 + n_2 u_2^3 \end{aligned} \tag{67}$$

(68)

which is solved by the Product-Difference algorithm.

It can be proven that this system is weakly hyperbolic. It has two double eigenvalues which are u_1 and u_2. It allows the crossing of two characteristic through the pressure term (included in M_2, which represents the velocity dispersion). But a singularity (δ-shock) will be created if three characteristics meet at the same point. The structure of system (67) can be seen as two independent pressureless gas systems as long as only two characteristics cross. These systems become coupled when at least three characteristics meet, and leads to the creation of a shock.

The numerical scheme is the same scheme as the one used for the pressureless gas (see Section 3.3). The difference is that, instead of having one local density and velocity, there are two local densities and velocities. Moreover, it is a first order scheme in space in order to preserve the velocity moment space.

4.2.2 Two-dimensionnal case

In the two dimensional case, working with velocity moments up to order 3, the moment vector writes $W = (m_0, m_0 M_{j,l})_{j+l\leq 3}$, where $M_{0,0} = 1$ and $m_0 M_{j,l} = \int\int u_x^j u_y^l f(t, \mathbf{x}, \mathbf{u})\, d\mathbf{u}$. W is a 10-component vector. The resulting system of conservation laws on moments for convection reads:

$$\partial_t m_0 M_{j,l} + \partial_x m_0 M_{j+1,l} + \partial_y m_0 M_{j,l+1} = 0,\ j + l \leq 3 \tag{69}$$

Closures have to be provided for the convective terms for which $j + l = 4$. To achieve that, we will use a quadrature method of moments in the spirit of [82]. Let $\alpha \in 1, \cdots, \mathcal{N}^d$ denote the set of weights and abscissas with a $\mathcal{N}$ quadrature level in one direction. We take here $\mathcal{N} = 2$ and will investigate a $2^d = 4$-node quadrature approximation of f. Higher $\mathcal{N}$ can be considered at the price of much more complex algebra and combinatorics, and for the sake of simplicity and efficiency, we will limit ourselves to the cas $\mathcal{N} = 2$. The velocity moments are then easily related to the quadrature weights ω_α and abscissas $(u_{\alpha,x}, u_{\alpha,y})$ by $m_0 M_{j,l} = \sum_{\alpha=1}^{2^d} \omega_\alpha u_{\alpha,x}^j u_{\alpha,y}^l$. The issue is to evaluate the abscissas and weights from the data of the velocity moment vector of size 10. The correspondance is one-to-one in one space dimension. However, in dimension greater or equal to two, we will transport the whole set of moments but effectively restrict the moment subspace recursively structured from the set of second-order velocity moments for which the correspondence is one-to-one, and insure that the velocity moment vector lives in this subspace. We introduce a linear transformation $\mathbf{L}$ as well as a rotation matrix, R, such that $(R\mathbf{L})^T R\mathbf{L} = (\sigma_{ij}) = \sigma$, $(i \in (x, y), j \in (x, y))$ with $\sigma_{ij} = \int u_i u_j f\, \mathrm{d}\mathbf{u}$, where σ is the covariance matrix.

Up to a rotation, the linear transformation $\mathbf{L}$, which is chosen as a Cholesky decomposition of σ in the rotated set of axes, allows for a natural change of variable. With this choice, we take $\mathbf{A} = (R\mathbf{L})^t$ and introduce the vector $X = [X_1, X_2]$, defined by $\mathbf{X} = \mathbf{A}^{-1}(u - \bar{\mathbf{u}})$, so that $u = \mathbf{A}\mathbf{X} + \bar{\mathbf{u}}$. This variable is a good candidate in order to perform tensorial 1-D quadrature based on the set of reconstructed centered third-order moments in the two new basis directions. There are fundamental grounds for using the Cholesky decomposition rather than the other methods. Defining matrix $\mathbf{A}$ in terms of the eigenvectors of the covariance matrix is a good choice for the passive transport of a distribution function. However, because the velocity is a dynamic variable, the fundamental difficulty comes from the fact that the eigenvectors of σ do not vary smoothly with its components. As a consequence, the fluxes computed from the abscissas are then discontinuous, leading to random fluctuations in the moments. In contrast, the Cholesky matrix $\mathbf{L}$ with $R = \mathbf{I}$ defines $\mathbf{A}$, which varies smoothly with the components of σ and, hence, the fluxes are well-behaved [82].
On the other hand, the disadvantage of using the Cholesky matrix is that it depends on the ordering of the covariance matrix, and is thus different for each of the two permutation (six in three dimensions) of the coordinates corresponding to the two R matrices identity and rotation by $\Pi/2$. It is thus desirable to replace these two linear transforms $\mathbf{A}_x$ or $\mathbf{A}_y$ in the two preceeding choices with a permutation-invariant linear transform. Here we consider the half-angle between these two transforms. This treats each direction in the same manner, and is now independant of the ordering of the covariance matrix. Besides this choice is stable and defines a subspace of the moment space in which the conservative variables live.

4.3 Final model and coupling

The models exposed in the two previous sections are now coupled in a model overcoming the two highlighted limitations of the multi-fluid model. High order moment methods are applied in both size and velocity phase space. We consider a polydisperse flow in this section again. We describe polydispersion and droplet crossing in the context of evaporation (for which we consider a d^2 law) and transport. We consider a mono dimensional case, as the extension to the bi-dimensional case does not bring any additional difficulty.
We make the following hypothesis on the distribution function, assuming that, in a size section, the size and velocity distribution are independent :

$$f(t, \mathbf{x}, s, \mathbf{u}) = n(t, \mathbf{x}, s)\phi(t, \mathbf{x}, \mathbf{u}) \tag{70}$$

This model is able to capture, as the multi-fluid model is, the dynamics of the droplets conditioned by size. But, into one size section, the dynamics of the droplets is independent from their size. The size and velocities moments are tensorial products of the independent size and velocity moments:

$$m_i^{(k)} M_j^{(k)} = \int_{s_{k-1}}^{s_k} \int_{\mathbb{R}} s^i u^j f(t, \mathbf{x}, s, u)\, \mathrm{d}s\mathrm{d}u \tag{71}$$

If we consider $N = 3$ for both size and velocity, the number of unknows is 4 size moments and 4 velocity moments. Given the fact that the 0^{th} order moments are equal and represent the total density of droplets, the system has 7 unknows.

The equation system then writes:

$$\partial_t W^{(k)} + \partial_x F(W^{(k)}) = \phi^{(k+1)} - \phi^{(k)} + AW^{(k)} \tag{72}$$

where $W^{(k)} = (m_0^{(k)}, m_1^{(k)}, m_2^{(k)}, m_3^{(k)}, m_0^{(k)} M_1^{(k)}, m_0^{(k)} M_2^{(k)}, m_0^{(k)} M_3^{(k)})^t$
and $F(W^{(k)}) = (m_0^{(k)} M_1^{(k)}, m_1^{(k)} M_1^{(k)}, m_2^{(k)} M_1^{(k)}, m_3^{(k)} M_1^{(k)}, m_0^{(k)} M_2^{(k)}, m_0^{(k)} M_3^{(k)}, m_0^{(k)} M_4^{(k)})^t$,

A is a 7×7 matrix, whose top left 4×4 submatrix is the matrix showed in (51), and whose the rest is filled with 0.

$$\phi^{(k)} = n^{(k)}(t, \mathbf{x}, s_{k-1})(1, s_{k-1}, \ldots, s_{k-1}^N, M_1^{(k)}, M_2^{(k)}, M_3^{(k)})^t.$$

The numerical scheme is a finite volume scheme, for which each contribution (evaporation, transport) is split. The transport operator is solved using the solver for multi velocity systems, detailed in the previous chapter. It is first order in space in order to preserve both size and velocity moment space. In the same manner, the evaporation operator is solved using the solver for the evaporation of a moment vector, detailed in the first section. The evaporation of the velocity moment vector does not bring any additional difficulty.

Paragraphe a modifier et mieux inserer
The preservation of the moment space is also important during transport in phase space. The local dynamical system defined in equations (32) can be rewritten $\partial_t Y^j = \Phi(Y^j)$, with, in case of the multi-fluid multi-velocity method,

$$Y^j = (m^j, m^j M_{10}^j, m^j M_{01}^j, m^j M_{20}^j, m^j M_{11}^j, m^j M_{02}^j, m^j M_{30}^j, m^j M_{21}^j, m^j M_{12}^j, m^j M_{03}^j).$$

or, in case of multi-fluid method

$$Y^j = (m^j, m^j u_x, m^j u_y).$$

This system is solved using an implicit Runge-Kutta Radau IIA method of order 5 with adaptive time steps. Whereas this resolution in case of multi-fluid method does not yield any difficulty, for the multi-velocity case it can lead to a non realizable set of Y^j. The preservation of the moment space requires working with the centered moments:

$$m^{(k)} \tilde{M}_{j,l}^{(k)} = \int_{S_{k-1}}^{S_k} \rho_l \, S^{3/2} \int_{\mathbf{u}} (u_x - M_{1,0}^{(k)})^j (u_y - M_{0,1}^{(k)})^l \, f(t, \mathbf{x}, S, \mathbf{u}) \mathrm{d}\mathbf{u} \, \mathrm{d}S, \tag{73}$$

for $j + l \geq 2$. Starting from there, even if it leads to additional nonlinear terms in the ODE system, the Radau solver can be adapted and yields a robust solver on the conservative centered moments that strictly preserves the moment space and allows working up to the boundary of the moment space, i.e., the monokinetic velocity distribution.

4.4 Tests and validations

We present some test cases where an analytical solution can easily be provided so that we can compare the analytical solution of the problem with the solution given by the computation of the high order moment model for size or velocity or the coupled model. In these test cases, inertial particles are considered, i.e with a Stokes number >> 1 meaning that they are not affected by the surrounding gas phase. The computations are performed considering only one size section, so we show that this model can describe polydispersion with only one size section, which cannot be done with the multi-fluid model. We are displaying first a one-dimensional case using the high order size moment method, and then coupled with the high order velocity moment method to illustrate droplet crossing. Secondly, droplet crossing will be displayed in a simple two-dimensional case, and the solution given by the high order velocity moment method will be compared with a result given by the multi-fluid model. Then, the solution computed with the coupled high order moment model will be compared with the analytical solution of the problem. Finally we will present the droplet crossing in a two-dimensional configuration.

For the first test case, we consider a a polydisperse droplet cloud with size distribution and initial velocity field are given by the following expressions:

$$f(x,s) = \begin{cases} \alpha(x)\sin(\pi s) + (1-\alpha(x))\exp(-s) & \text{if } x \leq 0.5 \\ 0 & \text{if } x \geq 0.5 \end{cases} \quad (74)$$

$$v(x) = \begin{cases} 0.5 & \text{if } x \leq 0.25 \\ 2 & \text{if } x > 0.25 \end{cases} \quad (75)$$

where $\alpha(x) = 4(0.5-x)^2$.

The analytical solution is the translation of the two parts of the density profile in the physical space, coupled with evaporation following a d^2 law ($R_s = -1$) explaining the lowering of the profiles. We chose the droplet cloud on the right faster than the left one in order to display the ability of the method to handle the vacuum zone engendered by the separation of the clouds. We set periodic boundary conditions on the space interval [0,1]. Thus, the faster droplet cloud will meet the lower one. The CFL number is 1, the number of cells is 400. We display results at two different instants: one before the meeting of the clouds ($t = 0.2$) and one after ($t = 0.4$). The numerical solution is represented by solid lines, and it is compared with the analytical solution represented by symbols.
Figure (20) displays the four analytical size moments, and the size moments at the two instants. We can notice first that the moment space is preserved, and the numerical solution matches the analytical one with great accuracy. Morevover, the vacuum zone created by the velocity difference is perfectly caught by the numerical scheme. At time $t = 0.4$ there is no agreement between the numerical and the analytical solution (which represents the kinetic solution) any more. The shock created is a pure numerical effect and is due to the assumption of a unique velocity conditioned by size. It must be kept in mind that we do not take collisions into account, and the real physical solution would result in a crossing of the clouds. To obtain this result, this method is coupled with the high order velocity moment method, allowing characteristics crossings. The results are shown in Figure (21). The resuls are displayed at $t = 0.4$, same instant as in Figure (20) to see the difference between the two models, and at time $t = 0.7$ to see the effective crossing of the clouds. We can notice the numerical diffusion more important than in the previous case due to the first order in space of this method.

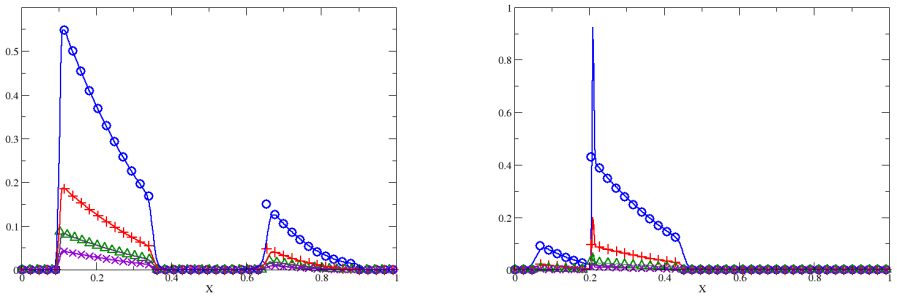

Figure 20: Numerical moments (solid lines) computed with high order moment method for size, compared with the analytical moments (o: zeroth order moment, +: first order moment, Δ: second order moment, *: third order moment), at two instants: $t = 0.2$ (left) and $t = 0.4$ (right)

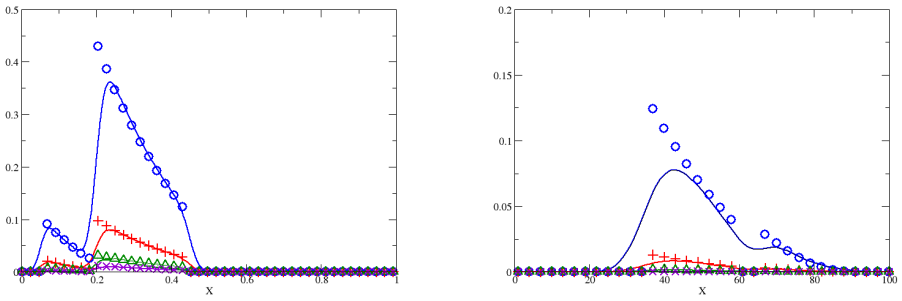

Figure 21: Numerical moments (solid lines) computed with high order moment method for size and high order moment method for velocity, compared with the analytical moments (o: zeroth order moment, +: first order moment, Δ: second order moment, *; third order moment), at two instants: $t = 0.4$ (left) and $t = 0.7$ (right)

The next configuration in a typical two-dimensional configuration for which the Eulerian multi-fluid model predicts an artificial averaging in Figure 22-left when two droplet jets are crossing without drag nor evaporation, for a monodisperse spray. Indeed, at the collision location, there are at the same space and time location two velocities leading two a bi-modal velocity distribution, that is out of equilibrium. The classical multi-fluid model, because of its equilibrium assumption, can not handle this case. The Eulerian multi-velocity model presented in Section 4.2 predicts the exact solution for this simple configuration for which the two jets do not see each other in the chosen infinite Knudsen limit, as it is show in Fig. (22-right).

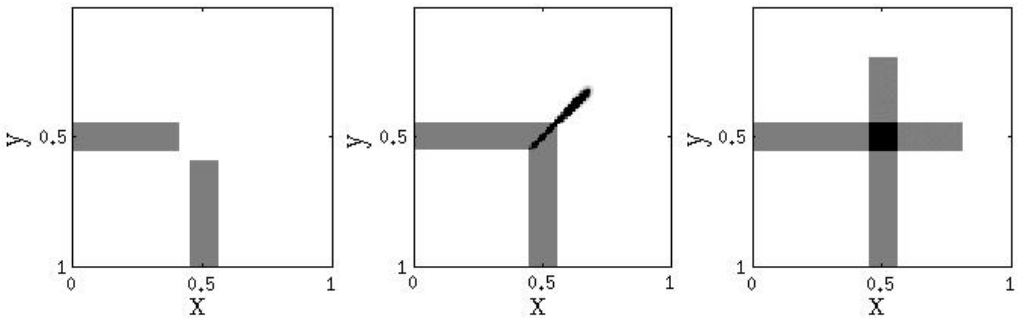

Figure 22: Simulation of crossing jets before collision at time $t = 0.4$ (left) and after collision at time $t = 0.8$, using the multi-fluid model (center) ant the multi-velocity model (right)

The next set of result focuses on two evaporating jets crossing each other. The first jet is injected from the bottom left of the domain the following velocity : $v_x = 1, v_y = 1$. The second jet is injected from the bottom right of the domain the following velocity : $v_x = -1, v_y = 1$. For this computation, we use a 100×100 grid, with a CFL number set as 1 as in the previous cases, with a computation lasting about one hour. We use a dimensional Lie-type splitting. This has the particularity, in the context of the same absolute value for the velocity for all the droplets and in every direction, to bring no numerical diffusion. The dynamics of the jet is represented in Fig 23-left and Fig 23-right. Figure 24-left represent the stationnary state reached

by the configuration, as the total number of droplets is evaporated at $t = 1$. If we consider the principal diagonal of a jet, the analytical solution of the particle number density on this diagonal can be easily found as there is no numerical diffusion. Figure 23-right is a comparison of the particle number density given by the numerical solution and the analytical number density on the principal diagonal of a jet. This result shows the ability of the model to handle the dynamics of the jets, which is less trivial than in the former test case, and its coupling with evaporation.

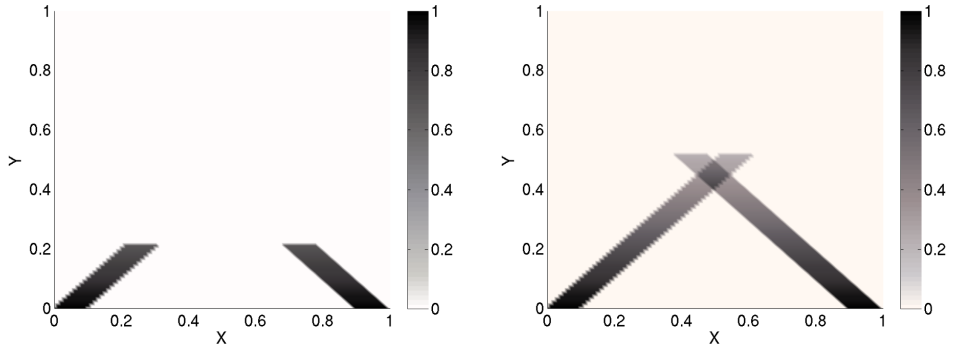

Figure 23: total particle number density of crossing evaporating jets simulated with high order moment methods for size and velocity , at two instants: $t = 0.2$ (left) and $t = 0.5$ (right), on a 100×100 grid

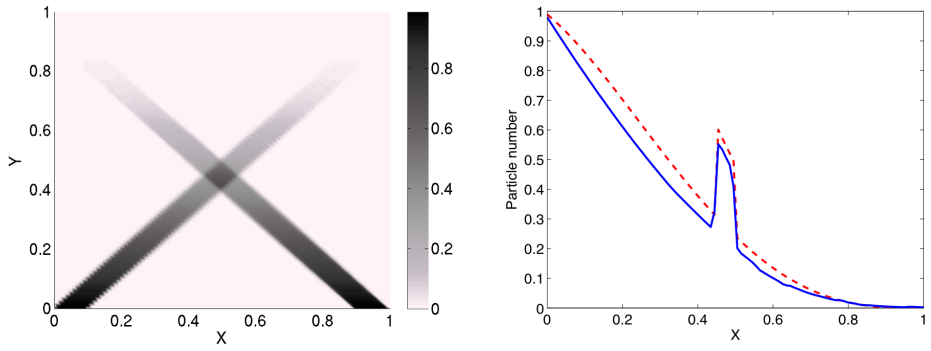

Figure 24: total particle number density of crossing evaporating jets simulated with high order moment methods for size and velocity at $t = 1$ on a 100×100 grid (left) and comparison of the number density of the numerical solution (plain curve) and the analytical solution (dashed curve)

5 Validation versus experimental measurements

The detailed numerical multi-fluid characterization performed in Chapter 3, studying multi-fluid's assumptions and model impact in vortical flows, enables to design configurations where the multi-fluid model is expected to give accurate results in the sense that the assumptions underlying the model are satisfied. We then decide to design an experimental configuration allowing multi-fluid validation through experience/simulation comparisons. For such a validation to be achieved, we need to be able to capture size-conditioned dynamics in the experiment.

We consider acoustically pulsated free jets with a polydisperse spray injection in an axisymmetric configuration. The acoustic excitation creates periodical large vortical structures, which

We end this section with a result dealing with two evaporating and crossing spherical clouds. In this case, the dimensional splitting operator algorithm used is based on the idea of Strang, leading to some numerical diffusion, which makes it different from the previous case. Figure 25 and 26 display the evolution of the clouds with respect to time. The computation is conducted for a 200×200 grid and lasts about two hours. Figure 25-left represents the initial location of the clouds. The top-left cloud is transported with the velocity $v_x = 1, v_y = -1$, the bottom-right cloud is transported with the velocity $v_x = -1, v_y = 1$. In Fig 25-right, the cloud begin to cross, therefore the density at the superposition of the clouds is equal to the sum of the density of each cloud. Figure 26-left, and Fig 25-right represent some further instants for which the clouds are crossing. The decrease of there density is due to the fact that they are being evaporated.
The two last tests enable to show that the numerical scheme for the transport of the velocity moments is independent from the numerical diffusion.

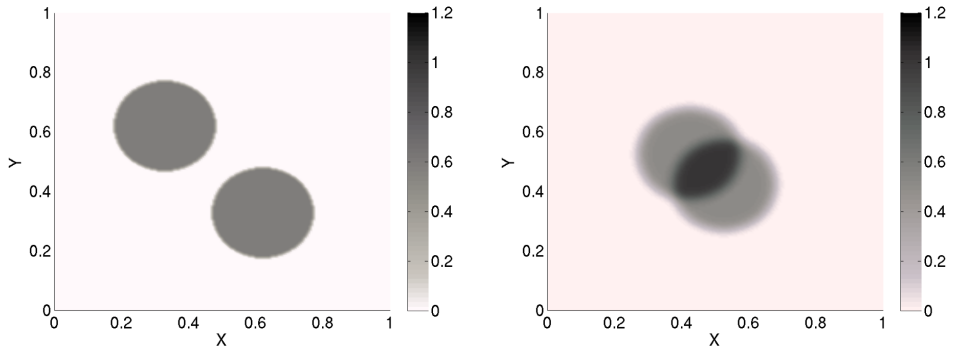

Figure 25: total particle number density of crossing evaporating spherical clouds simulated with high order moment methods for size and velocity , at the initial instant (left) and at $t = 0.1$ (right), on a 200×200 grid

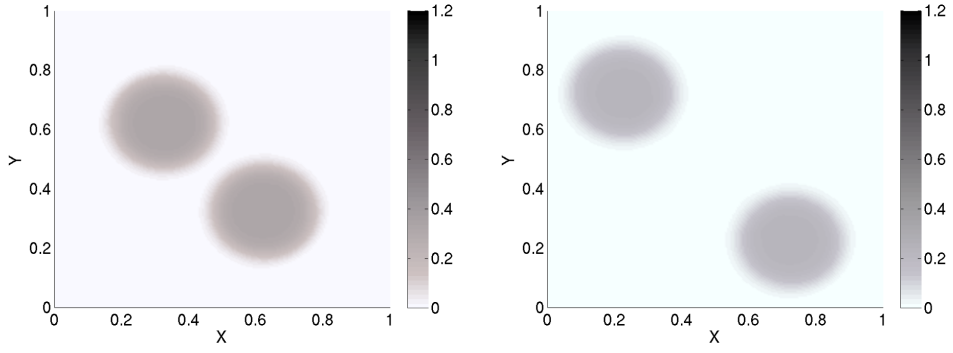

Figure 26: total particle number density of crossing evaporating spherical clouds simulated with high order moment methods for size and velocity , at $t = 0.3$ (left) and at $t = 0.4$ (right), on a 200×200 grid

are representative of the dynamics of gaseous flows in more complex configurations, and a strong interaction with the injected spray. In this context, we provide a series of detailed experimental measurements using laser diagnostics; we analyze droplet size distributions, associated size-conditioned dynamics and evaporation, for three liquids, leading to various droplet preferential concentrations due to the vortices. Besides the achievements in terms of diagnostics, we use the Eulerian multi-fluid model and dedicated robust numerical schemes, provided in Section 3.2, in order to conduct simulations in the chosen configuration. Detailed comparisons between numerical simulations and experimental measurements are provided in terms of spray velocity and number density. Size-conditioned preferential concentration of both non-evaporating and evaporating sprays are observed and reproduced by the numerical simulations, which eventually yields a validation of the proposed model.

The ability to analyze size-conditioned dynamics represents an important novelty, as much from the experimental and the numerical perspective, since a Eulerian method is used. The experiment has been realized by C. Lacour and D. Durox, at EM2C laboratory. Global comparisons were first presented in the 2007 International Conference on Multiphase flows, [77]. The size-conditioned comparisons described in this chapter have been published in the 32$^{\text{nd}}$ International Symposium on Combustion [53].

5.1 Configuration: pulsated free jet with spray injection

Crow and Champagne demonstrated that a circular jet has a natural instability at a frequency corresponding to the preferred mode of the jet [90]. This instability can be characterized by the Strouhal number Sh, defined by $\mathrm{Sh} = fD/U_b$, based on the excitation frequency f, on the jet diameter D and on the mean axial bulk velocity U_b. According to [90, 91], the jet strongly responds to excitations around the preferred mode $\mathrm{Sh} \simeq 0.4$, but is still very sensitive up to $\mathrm{Sh} = 1.5$.

Consequently, such a jet is an ideal candidate for a specific study on the behavior of a spray in a flow exhibiting zones of high vorticity. Thus the retained configuration is similar to the one in [92], in a non-reactive excited jet, laden by droplets. The range of selected Reynolds numbers is of the order of 1000 and yields a laminar gas flow at the nozzle outlet.

In order to allow easy comparisons between numerical simulations and experimental results, we work with dimensional quantities; however, the physics of the problem are governed by two non-dimensional numbers. The reference time $\tau_f = 1/f$ is the acoustic time corresponding to the frequency f imposed to pulsate the jet. The reference velocity u^0 is the mean axial velocity at the nozzle exit. A reference length can be deduced from these two quantities, which is characteristic of the coherent structure displacement. Characteristic droplet surface S_0 is equal to $\pi(60\mathrm{e}^{-6})^2$, where 60 μm corresponds to the diameter of the largest droplets in the spray at the burner outlet. The Stokes number St, is the ratio of the drag relaxation time $\tau_p(S) = (\rho_l S)/(18\pi\mu_g)$ to the acoustic time τ_f, whereas the evaporation number Ev is taken to be the ratio of the evaporation time $\tau_v(S) = S/R_s$ over the acoustic time :

$$\mathrm{St} = \frac{\tau_p(S)}{\tau_f}, \qquad \mathrm{Ev} = \frac{\tau_v(S)}{\tau_f}, \tag{76}$$

where ρ_l is the liquid density, μ_g the dynamic viscosity of the gas and R_s is a characteristic surface evaporation rate. Both numbers are linear functions of the droplet surface S.

Different liquids are used to vary the liquid evaporation rate. Decane is chosen as a reference slowly evaporating liquid, and methanol and heptane are more volatile. The mean size distribution for decane is presented in [77] and is weakly polydisperse as the other distribution, even if the methanol is a little broader (see Table 1). The dynamical response is essentially the same

for the three liquids but droplets of different size can have very different dynamics (see States numbers in Table 1). Conversely, the evaporation numbers are very different from one liquid to another since droplets below 18μm diameter of heptane or methanol have evaporated within one gaseous acoustic time, ie: one vortex eddy turn over.

	D_{10}	D_{32}	Ev(D_{32})	St(D_{32})
decane	26	36	93	0.12
methanol	20	32	3.4	0.13
heptane	20	40	6.8	0.15
	Ev(18)	St(18)	Ev(60)	St(60)
methanol	0.96	0.037	12	0.43

Table 1: mean size distribution and mean Sauter diameter (in μm) of decane, methanol, heptane and their corresponding evaporation numbers. In case of methanol, values of evaporation numbers for diameters of 18μm and 60μm.

5.2 Experimental devices and diagnostics

5.2.1 Experimental setup

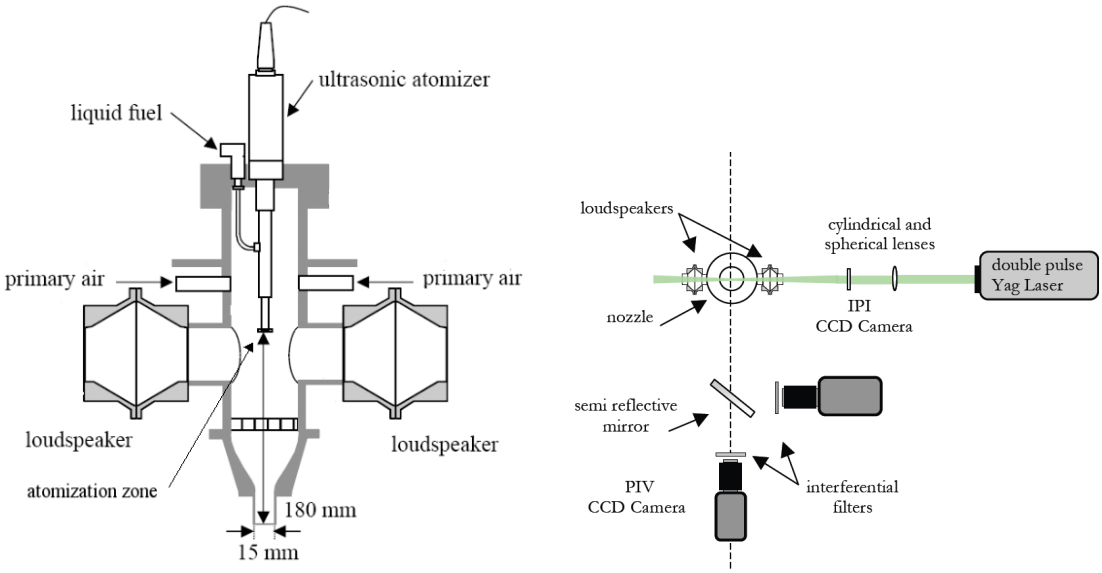

Figure 27: (left) Lateral view of the experimental setup, (right) PIV and IPI experimental set-up.

The experimental facility is presented in Figure 27. The injector is equipped with a converging nozzle with a symmetry of revolution leading to a flow at the nozzle exit with a turbulence level less than 1% of the mean axial velocity u^0=1.15 m.s^{-1}. A spray is generated from an ultrasonic atomizer, which is fed by a syringe [77]. The air jet flowing through this injector is acoustically forced by two loudspeakers placed on the sides of the facility to control the formation and evolution of vortices in the near field of the jet. Air flows through the cylinder into the facility and drags the droplets. In order to obtain a homogeneous flow at the nozzle exit, the distance between the atomizer tip, where volatile liquids start evaporating, and the nozzle exit is 180 mm and corresponds to a droplet residence time of a fraction of a second [92]. To benefit

from the positive effect of gravity on the droplet formation and motion, the facility is put in the downward direction.

The modulation frequency is $f = 50$ Hz so that the Strouhal number is $\mathrm{Sh} = 1.0$ in this study. At this Strouhal number the jet is highly sensitive and the excitation generates large periodic vortices closer to the nozzle exit, than for lower Strouhal numbers corresponding to the most amplified instability mode [91]. High vorticity levels are reached in the core of the vortices (600 s^{-1}) [77]. The full cycle of oscillations is divided into 20 regularly spaced phases.

5.2.2 Measurement techniques: PIV and IPI

The Particle Image Velocimetry (PIV) technique is used to characterize the gas flow and droplet velocities. The set-up consists in a double pulsed Continuum Nd:Yag laser. A laser sheet (500 μm thick) is focused on the central plane of the injector. The particle Mie scattering is collected on a Dantec Hi-Sense CCD camera 1600×1186 pixels^2 equipped with a Nikkor 60 mm lens and an interferential 532 nm filter. Velocity calculations are performed with an iterative cross-correlation algorithm (Dantec FlowManager). An iteratively decreasing interrogation window size is used with final value fixed to 16×32 pixels^2 with an overlap of 50 %.

The Interferometry Particle Imaging (IPI) technique aims at determining the size of transparent droplets, which flow through the light sheet and scatter light towards a camera. This technique is based on the interferences created in a voluntarily defocused image between reflected and refracted light rays, traveling through a transparent droplet. Using the geometrical approach [93, 94], the interference pattern between reflected and first order refracted light ray paths can be expressed by a simple linear relation between N_f the number of fringes and d_p the particle diameter $N_f = \kappa d_p$, where the geometrical factor κ is function of the light source wavelength, the observation and collection angles, and the relative refraction index of the liquid related to the gas. The present experiment is carried out with two CCD cameras collecting the scattered light at 90 deg relatively to the laser light source (see Figure 27). The set up is constituted on the base of the PIV set up described in this paper, with two identical cameras. The PIV camera is not only used for the droplet velocity measurement but for the droplet position detection too and the second one is defocused to generate the interference fringes. Two different configurations have been used to achieve different objectives. Firstly, the global behavior of the excited jet is studied with a full view of the jet with at least three successive vortices (59×44 mm^2), with the same experimental set up as previously detailed in [77]. The maximum measurable droplet diameter by IPI with this set up is about 90 μm, as one fringe has to be 4 pixel wide at least to be detected, and the minimum diameter is 9.6 μm to have more than one fringe in the defocused circle. In order to obtain correct statistics, the image acquisition has been phase-locked by synchronizing the laser and the camera with the loudspeaker excitation signal. For each of the 20 phases, at least 20 phase-locked pairs of images are acquired and treated. Results are then phase-lock averaged. In the present contribution, we intend to provide droplet density results for both a non evaporating and an evaporating situations as well as size-conditioned droplet dynamics. The previous set up was not suitable for such investigations for two reasons: limited droplet diameter range and too low statistics. In order to reproduce the experiment with an evaporating liquid, the measurable diameter range should be shifted towards the smaller droplets. The distance z_l between the laser sheet and the the camera lens, is thus reduced to 180 mm (collection angle $\alpha = 6.8$ deg), leading to a smaller field of view (27×20 mm^2) and a better spatial resolution. The measurable diameter range becomes $[5.2, 97]$ μm. Moreover, the number of phase-locked acquisitions is increased to 120 in order to enhance the statistical resolution.

5.3 Numerical Approach

5.3.1 Numerical Resolution

A multi-fluid spray computation is done, to be compared to these experiments. We use drag and evaporation models with convective corrections and we take into account the gravity. This multi-fluid computation was done, with regard to transport, with a dimensional splitting for 2-D axisymmetric configuration, described in Section 3.2.

5.3.2 Numerical setup

The numerical computation requires two types of input from experiments: 1- boundary condition for the dispersed phase spatially resolved in the radial direction at inlet for droplets mass densities and velocities in each section, 2- the full gaseous velocity field as a function of space and time to which the dispersed phase is coupled to in the numerical simulations.

For the latter, 20 phase-locked velocity fields obtained from PIV measurements are interpolated in time and space following the requirements of the dispersed phase discretization. After noticing in [77] that the slight deviation of the gaseous flow field from the 2D-axisymmetry could lead to peculiar behavior of the spray along the centerline, and in order to be compatible with the spray description, the obtained velocity fields are symmetrized in a symmetry plane. The resulting modification of the gaseous flow field is of the amount of a few percent in L^2 norm and is mainly important far from injection.

The former spray injection boundary condition roughly corresponds to the nozzle exit. For each time step and in each size section (20 sections of 3 μm width in diameter covering the $[0, 60]\mu m$ diameter range), at the inlet axial position, we interpolate spatially the droplet velocities conditioned by size. The injection width of the spray strongly varies in time; at each time and in each section, the number density of droplet is taken to be constant as a function of radial position in agreement with experimental measurements.

In the present contribution, the spray volume fraction are bounded in areas of preferential concentration by 5.10^{-5} and is mainly much below such a value, thus justifying the use of one-way coupling; besides, up to measurement precision, the gaseous velocity field with and without the spray are shown to be the same. The computational domain is discretized in 20 sections in the size phase space, and in 400×400 structured cells in the two spatial directions, thus offering good resolution for the purpose of comparisons with experimental results. Eventually, such a simulation is a quasi three-dimensional (2D in space, 1D in size) unsteady simulation carried out during four periods in order to reach a periodic regime.

5.4 Results and discussion

5.4.1 Global spray behavior

Let us first describe the full view of the configuration which covers the evolution of three vortical structures at least issued from the nozzle exit. One vortex covers the 40mm axial distance in a time of about 80ms that is $4\tau_f$ and the eddy turn over time is about 50ms. If we first concentrate on decane, the evaporation rate is so low at the considered temperature, that the liquid can be considered to be non-evaporating. In Figure 28-top, it is observed from experimental measurements that droplets are essentially absent from the vortex cores, whereas the vortical structures create both successive zones of concentrations along the centerline and large arms preventing the captured droplets from flowing toward the exit of the domain. The absence of the spray from the vortex core is due to the combination of two phenomena: mixing of the spray with the air entrainment associated with the pulsation of the jet and ejection of droplets from the strong

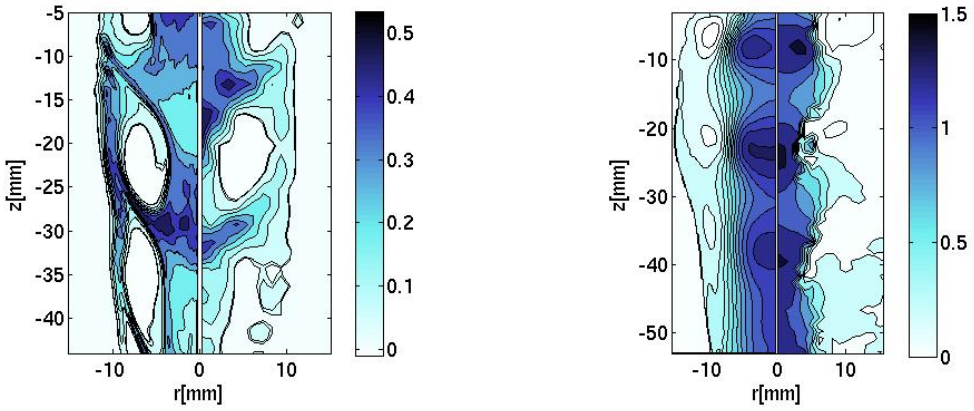

Figure 28: Comparison between experimental measurements - averaged field obtained from 20 instantaneous phase-locked samples (right half) for a 59×44 mm^2 field of view and numerical simulations on a 400×400 grid (left half): decane droplet concentration (droplet/mm^3 - left) and mean droplet axial velocities (m.s^{-1} - right) for the phase $\phi = 0$ (arbitrary reference).

vortical structures due to inertia (see tomographic images of the pulsated spray in [77]). The corresponding axial velocity of the droplets is presented in Figure 28-bottom. Let us underline that, extrapolating the results provided in [95], for the range of Stokes numbers associated with the biggest droplets under consideration, i.e. St = 0.43, an eddy turn over time is enough for an almost complete ejection of such droplets from the vortex present in our configuration, thus explaining the fact that droplets are being ejected after one vortex turn over as observed in the experiments. However, such an ejection of droplets from the vortex core is essentially governed by the size of the droplets and will be different depending on the size. Thus we need to focus on size-conditioned droplet dynamics. Before doing so, let us compare experimental measurements to numerical simulations at a global level.

First, the axial velocity map is presented for both experimental and numerical results in Figure 28-left. In the experimental case, velocities are measured essentially in the central region of the jet, as the droplets are absent in the vortex cores. Along the central axis, the droplets are successively accelerated and decelerated, corresponding to the vortex convection. The zones of maximum droplet velocities in the numerical velocity field are localized at the same position as in the experimental velocity field. Numerical results are thus able to reproduce the droplet axial velocity and such a good agreement is also obtained for radial velocity. Next, we compare droplet number density. It is measured from PIV results by considering the number of droplets in a given volume and is presented in Figure 28-right. The present results are representative of the general spray behavior. Concerning the numerical mean droplet concentration, high concentration zones are located at the head of each vortex. This result shows that the interaction between the high vorticity gas flow and the spray leads to a non uniform distribution of droplets. The vortex cores present voids of decane droplet concentration whereas high droplet concentration appear at the leading edges (head) of the vortices. Droplets are ejected from the high vorticity core and follow the external vortex arms. Consequently, at a global level, the comparisons are very good. Let us underline the progress made in terms of comparisons in reference to [77]; first, because of the coherence in terms of symmetry between the Eulerian spray modeling and the experimental gaseous velocity field, no peculiar behavior on the centerline is to be found. Besides, since we have included the variation of the spray width versus time at the inlet, and since we have greatly improved the experimental statistics, we reach a much more satisfactory level of comparisons.

This level will be denoted "quasi-quantitative"; actually even if some differences appear in the comparisons and even if we can not claim a fully quantitative agreement, up to measurement uncertainty, we reach both the same structure and levels of droplet density and velocity which justify such a denomination.

5.4.2 Size-conditioned dynamics comparisons

In addition, one of the objectives of the present study is to put forward the pulsated jet behavior regarding its polydisperse nature. In order to vary the size distribution width and to have a larger range of droplet diameters in the jet, different liquids are studied on a reduced experimental view (27×20 mm^2). The experimental droplet concentration is obtained from 120 instantaneous image pairs and averaged in windows of 0.66 mm^2. Figure 29 presents the total concentration

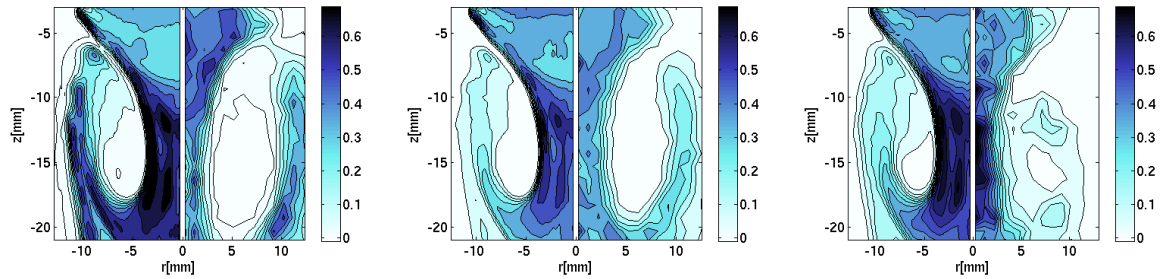

Figure 29: Comparison between IPI experimental measurements - averaged field obtained from 120 instantaneous phase-locked samples with a reduced field of view of 27×20 mm^2 (right half) and numerical simulations on a 400×400 grid (left half): total droplet concentration at phase π in droplet/mm^3; from left to right: decane (non evaporating reference liquid), methanol and heptane (evaporating liquids).

map obtained for decane (left), methanol (middle) and heptane (right) in the focused area under consideration. For the three liquids, droplets concentrate between the two vortices along the central jet axis and are ejected around the vortices to form external arms. The concentration reaches, in decane case, 0.4 droplet/mm^3 inside the arm which nearly catches up the central part of the jet. For the methanol spray, the pulsated jet structure is modified: the external arm concentration decreases to 0.2 droplet/mm^3. For the heptane spray, droplets are present inside the vortex core and concentration reaches 0.2 droplet/mm^3. The presence of evaporation thus changes the structure of the spray localization in both the vortex core and in the arms; such a phenomenon is well reproduced by the numerical simulations at a global level.

In order to further investigate the polydisperse nature of the spray and its evaporation, we focus on the first two liquids and investigate the dynamics conditioned by droplet size. Decane concentration maps corresponding to four size ranges are presented in Figure 30-top. For the classes of bigger droplets, the experimental results are noisy due to a poorer statistic, since the droplet number density is rather low. However, it is clear from experiments that the ejection of the droplets from the vortex core follow different dynamics depending on the inertia of the droplets. As size increases, the zone without droplets widens. Such a behavior is well captured by the numerical simulations, where the structure of the arm is found to be very different depending on the droplet size, thus exhibiting differential dynamics conditioned by size.

In the evaporating configuration, methanol concentration maps divided into in the same four classes are presented in Figure 30-bottom. The differential dynamics observed in the previous case is maintained in such a case, even if the repartition of droplet number density is very different in terms of level due to evaporation. Let us underline that droplets in the arms have

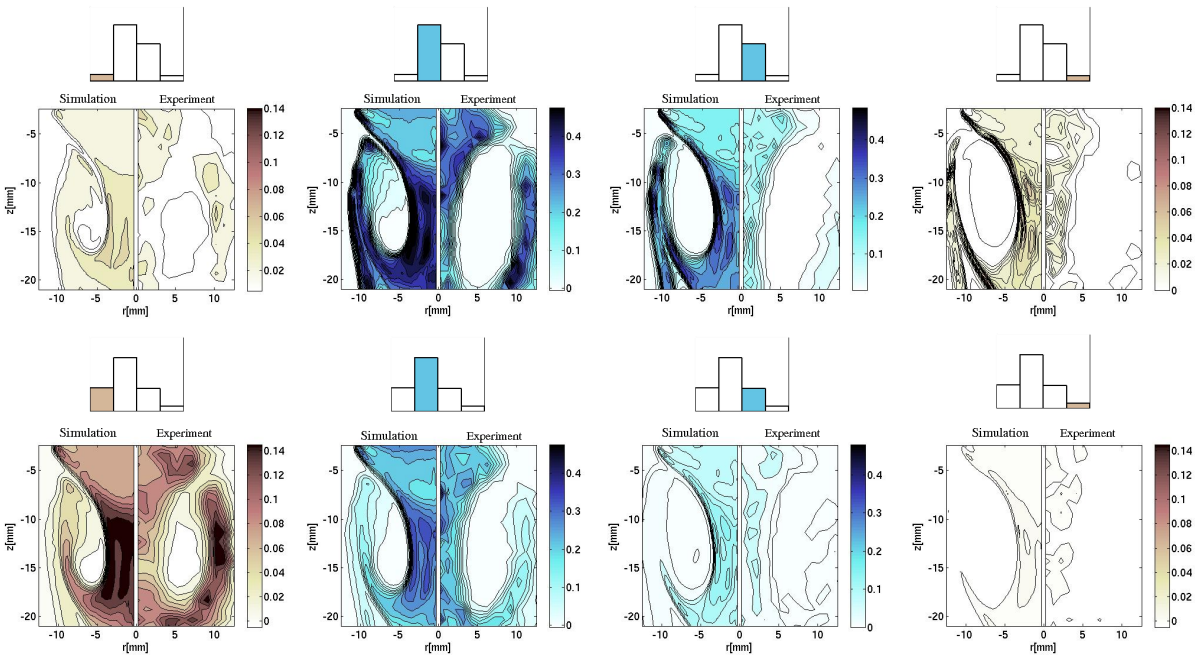

Figure 30: Comparison of size-conditioned decane (top) and methanol (bottom) droplet number density (droplet/mm^3) between 120 phase-locked IPI experimental measurements with a reduced field of view of 27×20 mm^2 (right half) and numerical simulations on a 400 × 400 grid (left half) at phase π. Four size ranges are presented from left to right, range [6,15] [15,30] [30,45] [45,60] in μm. Small histograms represent the droplet number repartition among the four size ranges. Two scales are used. Very small and big droplets have low concentration level and are presented in ochre, whereas the high concentration levels of droplets of inter size are presented in blue.

travelled about along one eddy along its turn over, thus corresponding to a time of about $2\tau_f$ and showing an important role of evaporation. However, evaporation yields additional differences. We can note a large amount of small droplets due to the evaporation phenomena and as the size increases, even if the area without droplet is enlarged, the structure of the created arm is rather different since the small droplets present in this arm have had various dynamics during the evaporation history and followed different paths from the small decane droplet. Such a phenomenon is captured by the numerical simulation, however, the statistics level is not high enough to capture it in the experiments. Once again, experimental and numerical results present very good agreement, thus demonstrating the ability of the Eulerian model to capture the differential dynamics of droplets of various size in a Eulerian manner. Let us also underline the robustness of the numerical methods used for the simulations since we were able to conduct a numerical simulation of the disperse liquid phase coupled to the gaseous flow fields obtained from experimental measurements.

In the present configuration, the spray dynamics leads to areas of preferential concentration of droplets which can eventually lead to a limitation of the IPI technique. Indeed IPI results rely on the processing of images and fringes counting, thus leading to a validation rate which can spatially vary depending on the droplet concentration. However, we have checked the total number of droplets present in the window of comparison is the same between experiments and numerical simulation, thus showing that the potential bias associated to higher droplet concentration does not have an important impact on the experimental measurement in these areas.

Eventually, let us emphasize that this contribution provides the first quasi-quantitative comparison of size-conditioned dynamics between experimental measurements and numerical simulation. This will be essential for more realistic configurations and for combustion chambers.

5.5 Conclusions

Experimental measurements of spray dynamics conditioned by droplet size obtained through the coupling of IPI and PIV diagnostics have been compared to numerical simulations using the Eulerian multi-fluid model. The configuration of a pulsated free jet with polydisperse droplet injection leading to the strong interaction of the spray with large vortical structures for three differently evaporating liquid fuels has been investigated. Generally, very good agreement is found between model and experiments, thus exhibiting various ejection time scales from the gaseous vortices depending on the droplet inertia and differential dynamics of droplets of various size. Such a phenomenon will be essential for combustion applications in more realistic configuration since it is responsible for the structure of the fuel vapor mass fraction topology. The physics of such two-phase flows is shown to be reproduced by the Eulerian model, eventually leading to its validation in a well-controlled 2D-axisymmetrical unsteady configuration.

6 Computational Multi-fluid dynamics

The description of the evolution of of the liquid density given by the multi-fluid model is validated in Section 3.4, through quantitative comparisons on simple configurations like Taylor-Green vortices and conical nozzle, and through qualitative comparison on a more realistic configuration of 2D-axisymetrical jet. It is also validated in the previous Section through comparison with experimental measurements.

The aim of this Section is to go further in such comparisons, showing the ability of such kind of method to describe the gaseous fuel mass fraction coming from evaporation and the corresponding flame, showing the influence of droplet crossing and finally, the feasibility of 3D

computations. The numerical tools are then first described, followed by the study of a 2D evaporating jet and a 3D computation of a homogeneous isotropic turbulence.

6.1 Numerical strategy

A new academical solver [81] has been created, coupling ASPHODELE solver, developed at CORIA by Julien Reveillon and collaborators [**?**], with the multi-fluid solver MUSES3D [81], using models developed in this paper. ASPHODELE solver couples a Eulerian description of the gas phase with a Lagrangian description of the spray. It allows for example, in the framework of one-way coupling, to compute simultaneously both spray descriptions with the same gas phase, within the same code run. This solver opens new possibilities of method evaluation in terms of dynamical comparisons and computational cost evaluation.

6.1.1 Eulerian-Lagrangian/Eulerian gas-liquid solver

The solver ASPHODELE, holds a DNS gas solver for low Mach (or incompressible) flows, coupled with a Lagrangian solver, computing, for non-colliding spray, Discrete Particle Simulation (DPS) or a Lagrangien Monte-Carlo method called Discrete Simulation Monte-Carlo (DSMC).

The low Mach solver for the gaseous phase is based on prediction correction method for the velocity evolution, as was introduced for incompressible flows in [96, 97] and extended for low Mach number flows in [98]. As far as numerical methods are concerned, the time resolution is provided by a third order explicit Runge Kutta scheme with minimal storage, [99]. Spatial evolution is done with a finite difference scheme, the derivatives are computed with a Pade 6^{th} order scheme, [100]. The boundary conditions are handled through the NSCBC method, [101]. The physical space solver is available for 2-D, 2-D axisymmetric, and 3-D configurations. A spectral solver is also available in the context of incompressible flows, for Homogeneous Isotropic Turbulence (HIT) computations done in Section 6.4.

The Lagrangian solver use a deterministic approach, with ODE on the position, the size and the velocity of each particle (DPS) [102, 103, 104], or a statistical approach (DSMC), using stochastic particles tracked into the flow and representing a discretization of the NDF [25]. These two methods are equivalent for non-colliding spray in a sense given in [81]. The Lagrangian numerical particles ODE are then solved within ASPHODELE with an explicit third order Runge Kutta solver. Therefore, the coupling between the gas and the liquid takes place at each Runge Kutta sub-step. Two main difficulties arise when coupling Eulerian and Lagrangian descriptions in two-phase flows. First, the gaseous quantities have to be computed at the position of the droplets in order to obtain the influence of the gas on the droplets : drag force, heat transfer, etc. It is done with a third-order interpolation algorithm [105] first developed for Particle Image Velocimetry. Moreover, in the framework of dispersed liquid phase, the influence of the liquid on the gas is modeled by source terms obtained from the Lagrangian tracking of the droplets and thus needing to be projected on the Eulerian gaseous grid. The projection used here is described in [106]. These two drawbacks are linked to different issue. The first one leads to a significant cost increase, while the second one is related to an approximation issue.

As far as time evolution is concerned, the coupling of Eulerian multi-fluid method (MUSES3D solver) with the gaseous phase differs from the one used for the Eulerian/Lagrangian coupling. Indeed, due to the kinetic scheme used for the multi-fluid (Section 3.3), a simple “Euler-like” time step is enough to obtain the second order in time and space and a Runge Kutta scheme will not improve the global order of the method. Furthermore, a unity CFL for the physical transport is needed in order to limit the numerical diffusion. Several time steps for the gas can then be computed during one time step for the spray and the constant gas assumption, valid

for a Runge Kutta sub-step, can not be used for the whole time step. However, the coupling with the gas only appears in the phase transport. A time interpolation of the gaseous fields is then used to compute the corresponding ODE with the radau method. Moreover, for a two-way coupling, the source terms for the gaseous phase are also computed during this phase transport and can the be 'transmitted' to the gas equations at each gaseous time step.

6.1.2 Gaseous fuel vapor prediction and burning

Taking two-way effects, i.e., influence of the spray on the gaseous carrier phase, may be of great importance for several applications, like for combustion where it is necessary in order to take into account the vaporization of the droplets into the gaseous phase before burning. Nevertheless, we restrict ourselves to one-way coupling since our objective is to evaluate multi-fluid models and compare them to Lagrangian methods on the same gas computation.

A first way to see the influence of the droplet evaporation on the gas is to compute the evolution of the resulting fuel mass fraction, without tacking into account its influence on the gaseous properties. This fuel mass fraction is then seen like a passive scalar, advected and diffused by the flow and the gas composition is not affected by the spray evaporation. This procedure has two advantages. First, it allows to have an insight of the fuel mass fraction evolution, without dealing with two-way coupling difficulties. Second, as this "virtual" evaporation does not modify the gas phase dynamics, it is possible to compare the evaporation produced by the two different spray methods with the same gas phase simulation, allowing to derive precise comparisons focusing only on the spray methods aspects.

We also are interested in taking combustion into account. To do so, we use a simple model with a global one-step non-reverible reaction between the fuel and an oxidizer. The important point that has to be noticed is that we want to develop this simple combustion model in a one-way coupling framework. Therefore, the mass fractions of fuel, oxidizer and burnt gases are not taking part of the gaseous phase composition. They all can be seen as passive scalars, with formation or destruction source terms, not taking part into account in the thermodynamics computation. The reaction rate is given by an Arrhenius like law, but at a temperature extrapolated from the burnt gases mass fraction [81]. Then we do not compute any heat release or gas dilatation; we only consider a "virtual" fuel and oxidizer consumption and "virtual" products formation. The gas phase is not modified by this combustion, that is called here Coldflame.

Numerically, we have to compute source term of fuel coming from evaporation, and the evolution of this "virtual" fuel, as well as oxidizer and product in the case of the Coldflame, are computed by the gaseous solver. The coupling between ASPHODELE and MUSES3D, allows to compute the fuel mass fraction obtained from the Lagrangian, $Y_{F'}^{Drop}$ and from the Eulerian multi-fluid method, $Y_{F'}^{MF}$. In the case of the Lagrangian spray description, the time evolution of $Y_{F'}^{Drop}$ is resolved through a Runge Kutta algorithm, and is thus easily introduced within the coupling algorithm. In the case of the Eulerian multi-fluid spray description, the insertion of the fuel mass fraction in the coupling algorithm is not so natural. Indeed, we want to use the same Runge Kutta algorithm for the evolution of the scalar, nevertheless, the spray being only resolved within a Euler time step, we can only compute the mass source term at time t_{n+1}, and not at the intermediate times of the Runge Kutta algorithm. We therefore decide to resolve the evolution of the fuel mass fraction using an operator splitting : solving first the evolution due to transport, diffusion and reaction through a Runge Kutta algorithm. The evolution due to spray evaporation is solved in a second time through a one-step Euler method.

6.2 2D evaporating jets with MF method

The studied configuration is designed to enable the evaluation of the Eulerian multi-fluid method. Turbulence is injected to destabilize the gasesous jet. Furthermore a polydisperse spray is injected to study the multi-fluid size distribution description. The Lagrangian reference is not taken as a converged Direct Simulation Monte-Carlo method in this study, in order to be closer to industrial concern. Given the DNS configuration used, we perform a Discrete Particle Simulation. Indeed there is no need to use Stochastic Parcel method, since all the droplets contained in the computational domain can be tracked. In order to focus on the Eulerian method evaluation, a one-way coupling is considered, and simple droplet models, are used.

This work was done during the Summer Program 2008, in collaboration with J. Reveillon and R. O. Fox [50].

6.2.1 Configuration

In order to assess the Eulerian methods we focus on a 2D cartesian free jet. A polydisperse spray is injected in the jet core with a log-normal size distribution (Figure 31-right).The simulations are conducted with a code that couples a gas solver to a Lagrangian solver (both developed at CORIA) and to a Eulerian solver (developed at EM2C) wherein the multi-fluid and multi-fluid multi-velocity methods are implemented.

As far as the gas phase is concerned, we used a 2D cartesian low Mach number compressible solver. The gas jet is computed on a 400×200 grid. To destabilize the jet, we inject turbulence thanks to the Klein method with 10% fluctuations, [107]. The Reynolds number based on u^0, ν_0 and L is 1000, where u^0 is the injection velocity, L is the jet width and ν_0 is a typical kinematic viscosity of the gas. We will eventually provide dimensional quantities for illustration purposes. These will be based on an estimated velocity of $u^0 = 1$ m/s and $L = 1.5 \times 10^{-2}$ m, as well as a typical value of 1.6×10^{-5} m^2/s for ν_0. Finally we have $d_0 = L/300$, where d_0 is the diameter corresponding to the typical droplet surface s^0. The gas vorticity is presented in Figure 31-left. Since we aim at validating the Eulerian models through comparisons to a Lagrangian simulation, and at providing an evaluation of the relative computational cost, we restrict ourselves to one-way coupling. We inject in this jet a polydisperse spray, with an initial log-normal size distribution, see Figure 31-right. We take as a reference solution for the liquid phase a Lagrangian Discrete

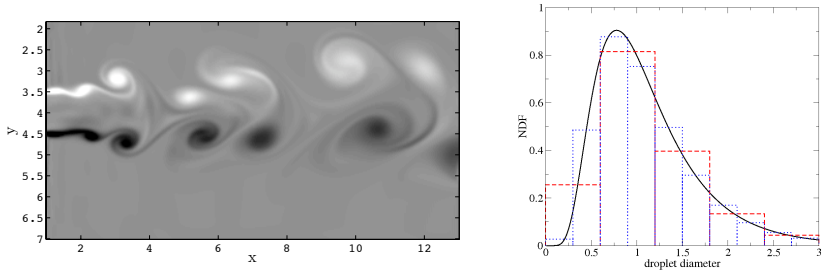

Figure 31: Free jet configuration: (left) gaseous vorticity at time t=20, obtained on a 400×200 grid; (right) polydisperse log-normal distribution discretized with 5 (dashed lines) to 10 (dotted lines) sections.

Particle Simulation with 10,000 up to 70,000 particles in the computational domain depending on the cases. The number of droplets is determined by stoichiometry. We provide comparisons between this Lagrangian reference and the Eulerian multi-fluid and multi-fluid multi-velocity computations plotting the Lagrangian particle positions versus the Eulerian number density.

Thanks to the multi-fluid polydispersion resolution, we perform the comparisons for different ranges of sizes and thus for various inertia, in the evaporating and non-evaporating cases.

6.2.2 Lagrangian vs. multi-fluid for evaporating and non-evaporating sprays

Non-evaporating spray injection For the non-evaporating case we use five sections for the Eulerian multi-fluid simulation. We have 70,000 Lagrangian particles in the computational domain at the considered time. We first present the results for the whole spray, regardless of the droplet sizes. These results are plotted on Figure 32. Taking advantage of the multi-fluid model

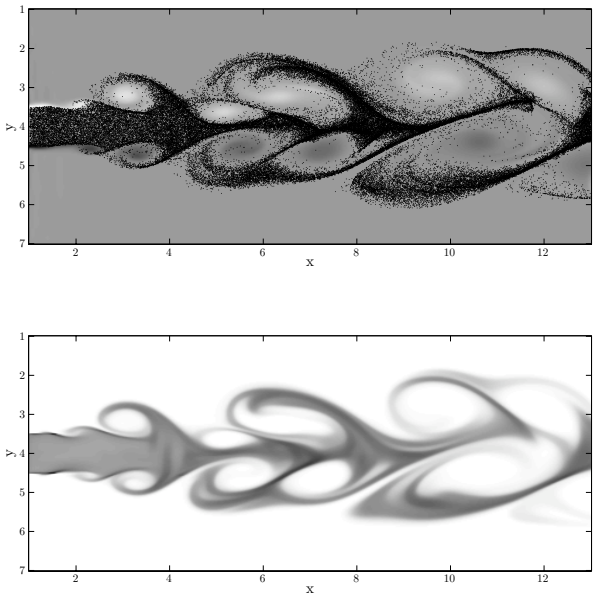

Figure 32: Non-evaporating polydisperse spray, Stokes 0.011 to 1.1 corresponding to diameters $d = 9\,\mu m$ to $d = 90\,\mu m$, at time t=20, : (top) Lagrangian particle positions with 70000 particles, (bottom) Eulerian total number density with a $400 \times 200 \times 5$ grid.

polydispersion description, we are able to present size-conditioned dynamics. We then present a comparison for low inertia droplets and find a very good agreement for the droplets with a Stokes range from 0.011 to 0.12 corresponding to diameters from 9 μm to 30 μm, as shown in Figure 33. The multi-fluid method is thus shown to simulate the dynamics of a polydisperse spray where droplet crossings are limited. Droplet dynamics are close to the gas dynamics for this range of sizes, and the model remains therefore in its validity domain (see Section 3.2). For higher Stokes number, the droplets are ejected from the vortices and crossing trajectories are likely to occur, breaking the monokinetic multi-fluid assumption described in Section 3.1. Nevertheless, the dynamics is still very well reproduced for higher inertia droplets. The results are plotted in Figure 33-right for Stokes number from 0.48 to 1.1 corresponding to diameters from $60\,\mu m$ to $90\mu m$.

Evaporating spray : Lagrangian versus multi-fluid The free jet is also assessed with an evaporating spray. For the d^2 law, we take a constant mass transfer number $B_M = 0.1$. The results are presented the same way as for the non-evaporating case. In order to describe

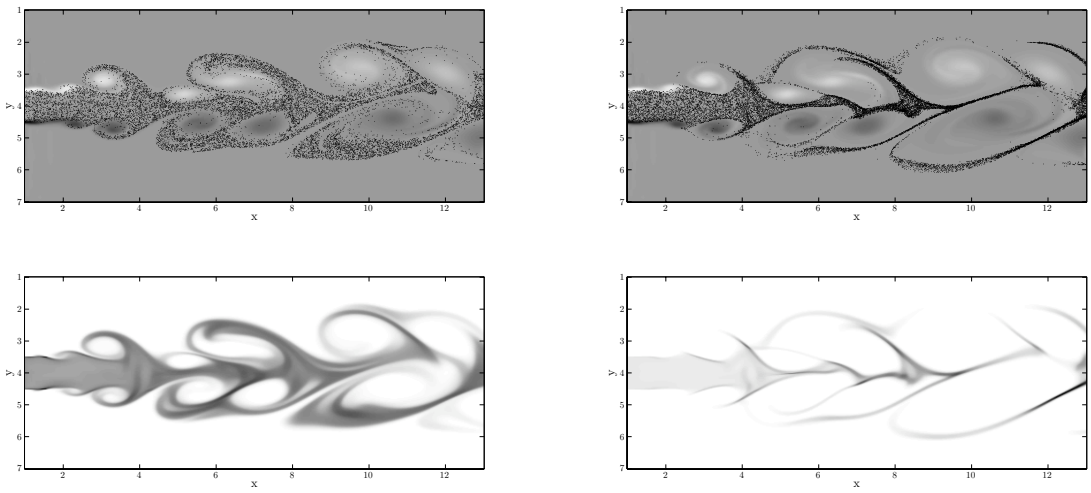

Figure 33: Non-evaporating polydisperse spray at time t=20 : (left) low inertia droplets, Stokes 0.011 to 0.12 corresponding to diameters $d = 9$ μm to $d = 30$ μm, (right) high inertia droplets, Stokes 0.48 to 1.1 corresponding to diameters $d = 60$ μm to $d = 90$ μm; (top) Lagrangian particle positions with 40,000 particles over gas vorticity, (bottom) Eulerian number density on a $400 \times 200 \times 5$ grid.

accurately the evaporation process, we take ten sections for the Eulerian multi-fluid simulation, whereas 30,000 Lagrangian particles are present in the domain at the considered time. As in the non-evaporating case, we found a very good agreement between the Eulerian multi-fluid and the Lagrangian descriptions, for low inertia droplets in Figure 35-left, with Stokes numbers from 0.011 to 0.12 and for high inertia droplets in Figure 35-right, with Stokes number from 0.48 to 1.1. These more inertial droplets are ejected from the vortices and crossing trajectories are likely to occur, breaking the monokinetic multi-fluid assumption described in Section 3.1. Nevertheless, the dynamics are still very well reproduced for higher Stokes numbers. One can notice that the number density is concentrated in a few cells in this case and the numerical method does not encounter any problem to capture it, illustrating again the method's robustness and accuracy.

This polydisperse evaporating free jet shows the ability of the multi-fluid method to treat more complex cases, closer to realistic configurations. From these comparisons, we demonstrate that the Eulerian method captures size-conditioned dynamics that carry droplets of different size to different locations. It is then essential to evaluate the ability of the Eulerian model to capture the evaporation process as a whole.

Gaseous fuel mass fraction : Lagrangian versus multi-fluid Our interest being in combustion applications, a key issue of evaporating spray modeling is the gaseous fuel mass fraction prediction. We thus present comparisons between this gaseous fuel mass fraction, obtained from the Lagrangian and the Eulerian multi-fluid descriptions of the spray. These results are obtained within the same coupled code run, the spray being described on one hand by the Lagrangian method and on the other hand by the Eulerian multi-fluid model. This simulation is still done using a one-way coupling. Indeed, the evaporated fuel is not added as a mass source term in the gaseous equations, but is stored in two passive scalars, one for each description of the spray, that are transported by the flow. The Lagrangian gaseous fuel mass fraction is obtained through

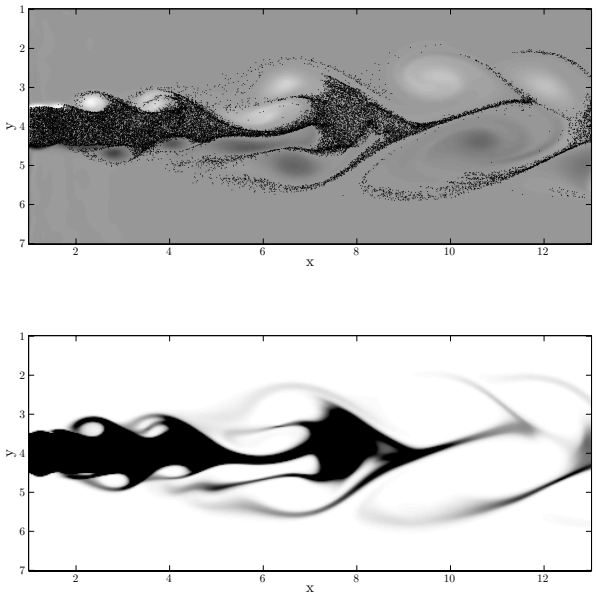

Figure 34: Evaporating polydisperse spray, Stokes 0.011 to 1.1 corresponding to diameters $d = 9\,\mu m$ to $d = 90\,\mu m$, at time t=20, : (top) Lagrangian particle positions with 30000 particles, (bottom) Eulerian total number density with a $400 \times 200 \times 5$ grid.

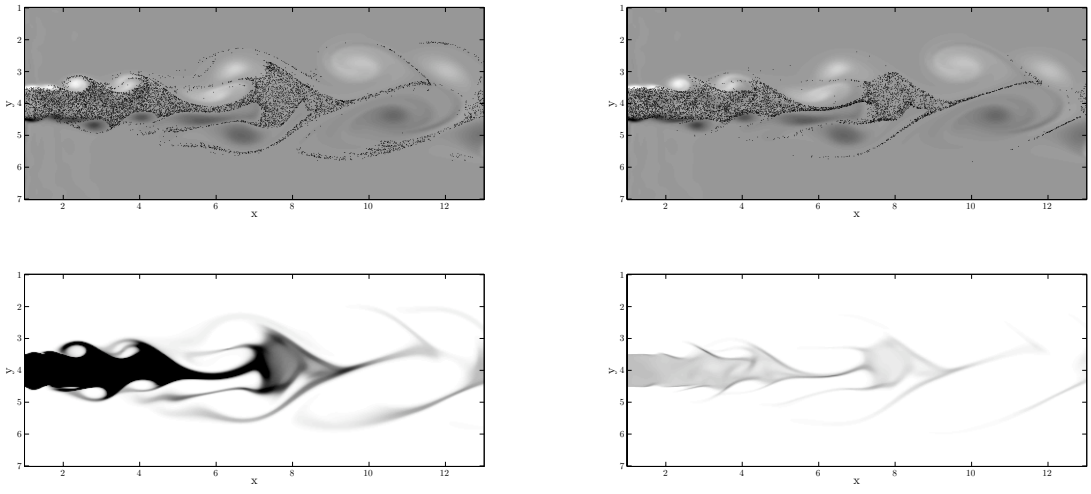

Figure 35: Evaporating polydisperse spray at time t=20 : (left) low inertia droplets, Stokes 0.011 to 0.12 corresponding to diameters $d = 9$ μm to $d = 30$ μm, (right) high inertia droplets, Stokes 0.48 to 1.1 corresponding to diameters $d = 60$ μm to $d = 90$ μm; (top) Lagrangian particle positions with 7,000 particles over gas vorticity, (bottom) Eulerian number density with a $400 \times 200 \times 10$ grid.

a projection of the droplet evaporation over the neighbor cells of the gaseous mesh. These two

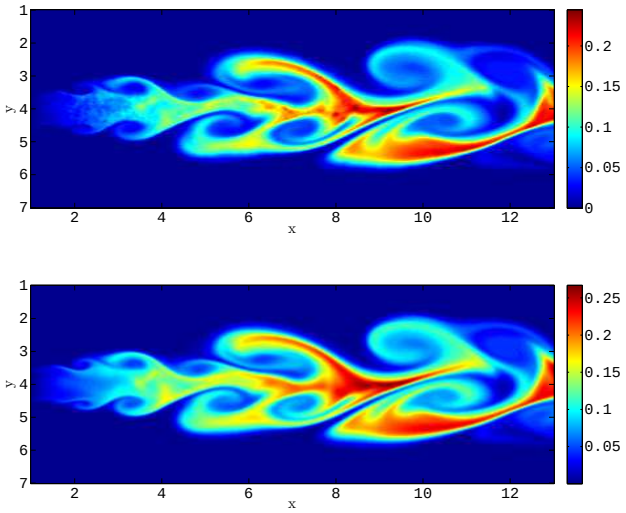

Figure 36: Comparison of the gaseous fuel mass fraction at time $t = 20$, obtained from evaporation using (top) a Lagrangian method with 30,000 droplets at the considered time and (bottom) a Eulerian multi-fluid model with a $400 \times 200 \times 10$ mesh.

fields are plotted in Figure 36. One can see the very good agreement of both descriptions for spray evaporation. This comparison underlines the efficiency of the Eulerian multi-fluid model in describing polydisperse evaporating sprays. Furthermore, as we can see in Figure 36, the Eulerian description provides a smoother field than the Lagrangian one. It illustrates the difficulties arising when coupling the Lagrangian description of the liquid to the Eulerian description of gas and underlines the advantage of the Eulerian description of the spray for the liquid-gas coupling. These results are a first step towards combustion computations.

A first combustion case : coldflame computation In order to assess a first combustion case, we study the gaseous combustion of the evaporated fuel. As it is aimed to conserve an approach devoted to spray resolution method evaluation, the combustion should not modify the gas phase thermodynamics. A peculiar framework is thus defined for combustion, given in details in [81], and referred to as coldflame. Therefore, as for the gaseous fuel mass fraction, the burnt gases and the oxidizer are defined in scalars that are not taken into account in the gas thermodynamics. The burnt gases mass fraction sets the temperature of the coldflame. The reaction is taken as a global one-step non-reversible reaction. The reaction rate is given by an Arrhenius law modified by GKAS technique. The ignition is done at the chemical equilibrium.

The fuel vapor fraction field obtained with the Eulerian multi-fluid description, Figure 36, can be burnt using the coldflame framework. In this configuration, the only information available about combustion process is the burnt gases mass fraction. It is represented in Figure 37-bottom, as well as the resulting fuel vapor mass fraction, Figure 37-top. This achievement provides a first step toward multi-fluid description of two-phase combustion applications, in multi-dimensional configurations.

The results obtained for the fuel vapor mass fraction description and for the coldflame computation demonstrate three main points in the study of the multi-fluid model:

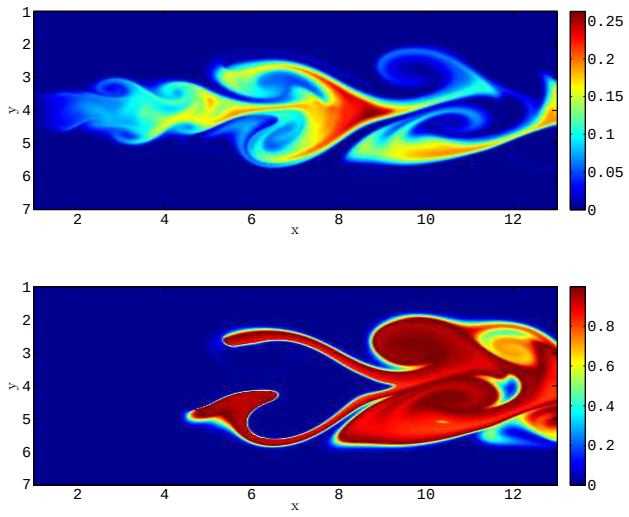

Figure 37: Coldflame at time t=20 using a Eulerian multi-fluid model with a $400 \times 200 \times 10$ mesh : (top) gaseous fuel mass fraction; (bottom) burnt gas mass fraction.

- the efficiency of the multi-fluid size distribution description as well as the size-velocity correlations;
- the global efficiency of the multi-fluid monokinetic formulation in turbulent jet configurations;
- the relevance of the multi-fluid model for combustion applications.

6.3 2D evaporating jets with MF-MV

For the simulations with multi-velocity model, the first step is to show the good level of agreement between the Eulerian model and the Lagrangian simulation. Thus, Figure 38-left presents a fair comparison, similar to the level obtained in previous simulations. In order to quantify the ability of the method to capture droplet crossing, we have also plotted in the right part of the figure the half trace of the covariance matrix, which amount to a "temperature" in the case of isotropic velocity distributions. However, since this is also present in areas of very small mass due to numerical diffusion, we have also plotted the absolute value of the difference of the two eigenvalues of this matrix, thus showing areas where there is strong anisotropy and corresponding to crossing "in progress". This very beautifully fits with the plots in Figure 38-left.

Finally, we have plotted the results of the multi-velocity model with evaporation in the case of the polydisperse spray jet in Figure 39. Once again, this figure demonstrates the ability of the proposed method to capture the dynamics conditioned by size as well as evaporation for a range of small to finite Stokes numbers.

6.4 Frozen Homogeneous Isotropic Turbulence

The study of a polydisperse spray dispersion in a 3-D Homogeneous Isotropic turbulence represents a first step for 3-D multi-fluid evaluation. It completes the evaluation of its applicability to industrial scale computations.

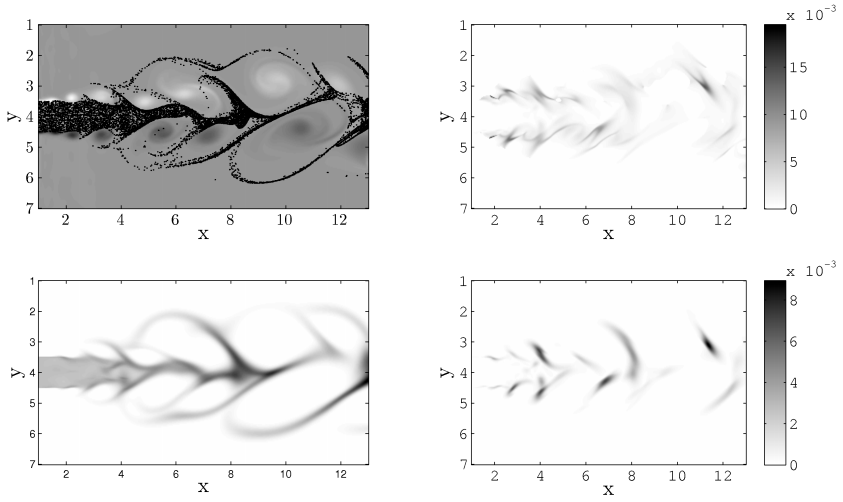

Figure 38: Non-evaporating polydisperse spray, high inertia droplets, Stokes from 0.48 to 1.1 corresponding to diameters $d = 60$ μm to $d = 90$ μm, at time t=20: (left-top) Lagrangian particle positions with 20,000 particles over gas vorticity, (left-bottom) Eulerian number density with a $400 \times 200 \times 5$ grid. Evaluation of the trace of the covariance matrix (right-top) as well as the absolute value of the difference between the two eigenvalues highlighting the zones of droplet crossing (right-bottom).

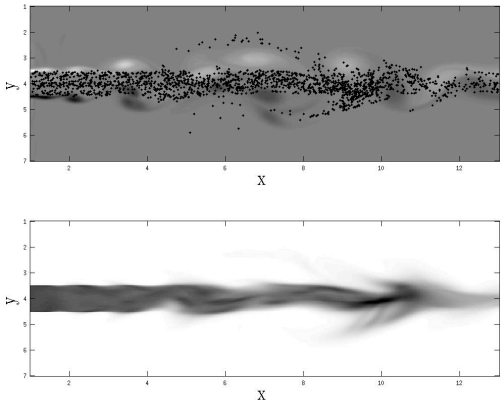

Figure 39: Evaporating polydisperse spray, high inertia droplets, Stokes from 0.48 to 1.1 corresponding to diameters $d = 60$ μm to $d = 90$ μm, at time t=15: (top) Lagrangian particle positions with 7,000 particles over gas vorticity, (bottom) Eulerian number density with a $400 \times 200 \times 10$ grid.

The key point in this computation is to illustrate its feasibility of a 3D simulation.multi-fluid description of the spray. This computation represents a challenge concerning scientific computing issues. Indeed, due to the size phase space discretization performed in the multi-fluid, this computation is 4-D. Therefore, MUSES3D solver has been parallelized with the help of MPI (Message Passing Interface) library. The gas phase computation, as well as the Lagrangian one, used to provide a validation of the multi-fluid, were done at CORIA, [106, 108]. Eulerian results

are compared to the Lagrangian ones for the description of the spray dynamical equilibrium arising in HIT flows.

These recently obtained results provide an interesting basis to study the physics of the spray in HIT through a Eulerian size-conditioned description, that should be done in future works.

The Homogeneous Isotropic Turbulence configuration appears to be interesting to assess 3-D multi-fluid for three reasons:

- a spray dynamical equilibrium with the turbulence is reached, that corresponds to a stationary slip velocity standard deviation, [106]. This equilibrium leads to a stationary repartition of the spray density in the flow, conditioned by droplet size. This equilibrium is thus very interesting to compare the Eulerian and Lagrangian descriptions of the spray. This result can be linked with the work done in [109] showing the existence of an equilibrium velocity conditioned by size.
- HIT configuration provides very interesting points to assess Eulerian spray description, as crossing trajectories that can occur for inertial droplets. Furthermore, the study of the Eulerian velocity field of the spray conditioned by size is also a relevant issue. Although these points are not studied here, the required basis are provided.
- Thanks to the use of a spectral solver, associated to a relatively low computational cost, the HIT configuration is also interesting for practical reasons.

6.4.1 3-Dimensional DNS configuration

The Eulerian multi-fluid description of the spray dynamics are presented for two Stokes number, based on the Kolmogorov length scale:

- St= 0.17, corresponding to droplet with diameter d= 20μm.
- St= 1.05, corresponding to droplet with diameter d= 48μm;

These two different inertia allows to study a spray ejected from the center core and segregated in weak vorticity areas, [106]. They are thus well suited for robustness evaluation of the multi-fluid method. Indeed high density regions, as well as vacuum, are created, that represent a challenging issue for a Eulerian method. Higher Stokes number are not tackled here since [106] shows that for Stokes number greater than unity, the droplets are inertial enough to cross high-vorticity areas, leading to a less segregated spray. In this case droplet trajectory crossings have a strong impact on the spray repartition and the monokinetic assumption of the multi-fluid might not allow to describe it. A precise study extending the notion of critical Stokes number, introduced in Section 3.2.2, to this 3-D HIT configuration would be needed to analyze precisely the impact of the monokinetic assumption on the spray modeling. Nevertheless, our aim here is only to provide a first realization of 3-D multi-fluid spray computation as well as a first validation. The number density of the spray is plotted in planes at the edges and inside the domain, Figure 40 and Figure 41 respectively to provide a global comprehension of the spray repartition. Both Stokes number St= 0.17 and St= 1.05 are plotted in each figure.

Figures 40 and 41 show, as expected, two different dynamics, with a higher segregation for the Stokes St= 1.05, and thus with high concentration regions and vacuum.

6.4.2 Parallel multi-fluid computation for 3-D spray

As far as the grid is concerned, the same Cartesian grid as the gas phase is chosen. One has to note that the gas is resolved through a cell-vertex finite-difference scheme, whereas the multi-fluid method uses a cell-center finite-volume method. Therefore the gas cell vertexes are taken

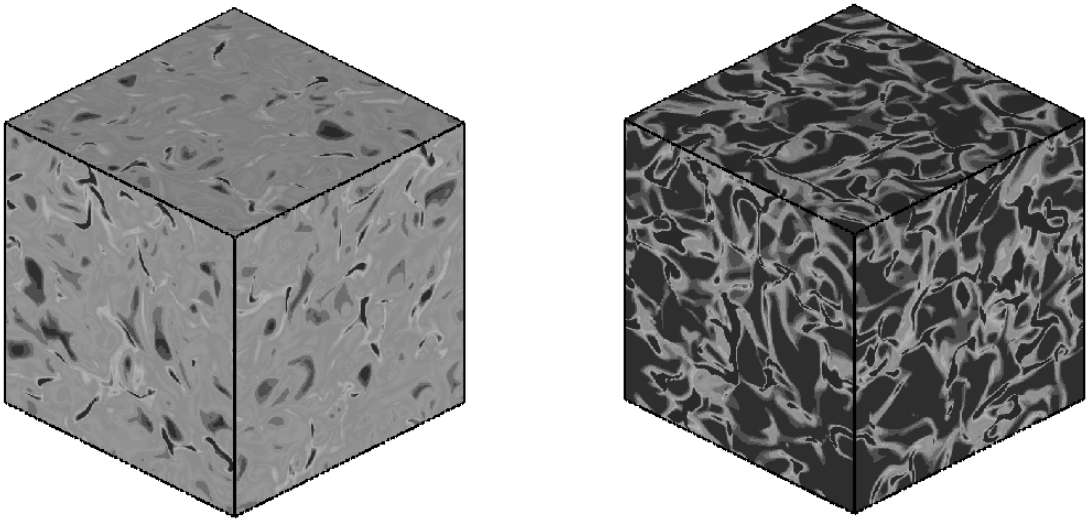

Figure 40: Eulerian spray number density at the edges of the domain, obtained with the multi-fluid method on a 129^3 Cartesian grid : (left) St= 0.17, (right) St= 1.05.

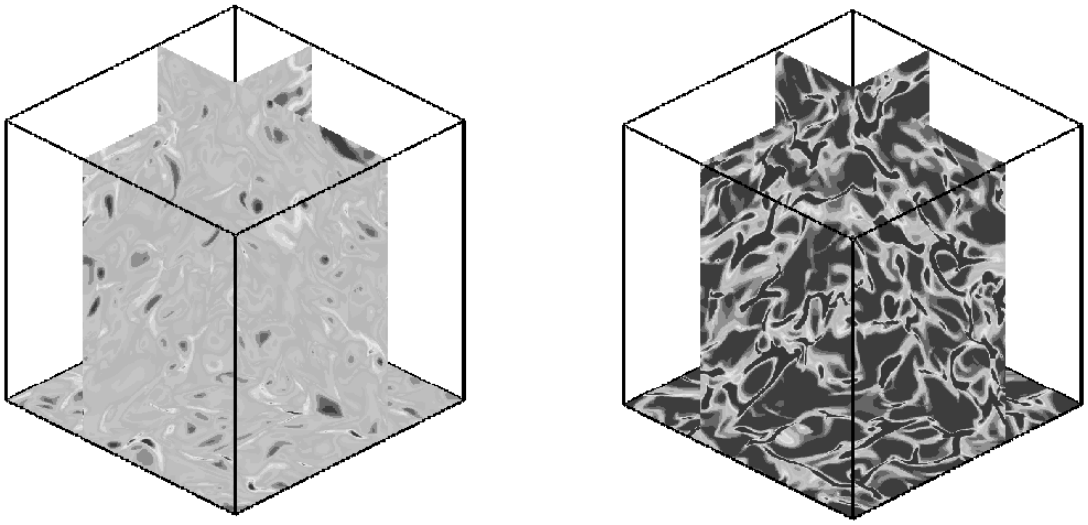

Figure 41: Eulerian spray number density in perpendicular planes inside the domain, obtained with the multi-fluid method on a 129^3 Cartesian grid : (left) St= 0.17, (right) St= 1.05.

as the multi-fluid cell centers. This choice was made for practical reason, in order to avoid spatial interpolation, nevertheless it is possible to use a more refined grid for the multi-fluid. A space domain decomposition is chosen for the multi-fluid. Therefore each process of the parallel computation has a domain Nx $\times$Ny $\times$Nz $\times$Ns, where Nx $\times$Ny $\times$Nz is the number of grid points of the process sub-domain and Ns is the number of multi-fluid size sections.

The best efficiency for MUSES3D solver in this configuration is obtained for 100 MPI parallel processes. This setup has been obtained with MADNESS EM2C cluster. expliciter les caractérisitques de madness. The domain decomposition minimizing the communication time is obtained for (N_{px},N_{py},N_{pz})=(5,5,4), where N_{pi} is the number of processes in the i^{th} direction.

6.4.3 3-D multi-fluid Lagrangian validation

A Lagrangian DPS computation with two Million droplets uniformly distributed in the domain is used to perform comparisons. This computation has been done at CORIA laboratory, [106, 108].

Global qualitative comparisons with a Lagrangian description of the spray are provided in order to assess the multi-fluid description in the range of Stokes number studied. Comparisons are carried out in two planes $x = 1.75$ and $z = 1.75$. In the chosen inertial range, the spray is ejected from the vortex cores and accumulated in low vorticity areas. In order to link the spray dispersion given by both methods, to the gas vorticity structure, the square norm of the gas vorticity is given in Figure 42 in the considered plane. The comparisons are provided for the low

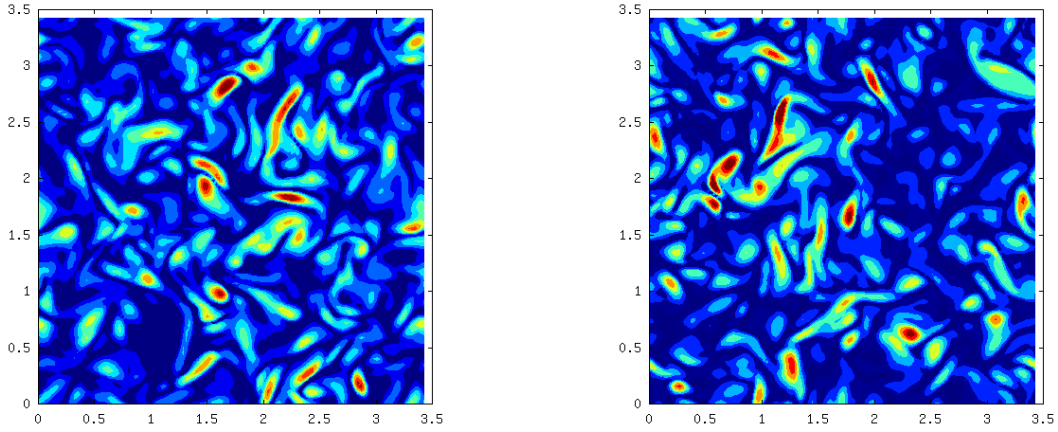

Figure 42: Gas vorticity square norm in the $(y - z)$ plane at $x = 1.75$ and in the $(x - y)$ plane at $z = 1.75$.

Stokes droplets, St= 0.17, in Figures 43 and 44 for planes $x = 1.75$ and $z = 1.75$ respectively. For higher Stokes droplets, St= 1.05, comparisons are given in Figure 45 and 46.

Qualitative comparisons between both approach can be done focusing on the vacuum zones description. These zones correspond to the gas vortex cores, that can be identified from the vorticity representation provided in Figure 42. The repartition of these vacuum zones and their evolution with droplet inertia is described with a good qualitative agreement by the Lagrangian and the Eulerian method.

Interesting perspectives can be thought of from these results. Indeed, they provide the basis for physical studies on Eulerian description of spray ejection in 3-D vortices. The analysis of the Eulerian velocity field, will enable to assess the existence of an equilibrium velocity variety, introduced in [39]. The study of this attracting velocity field will provide comprehension of droplet ejection dynamics. Furthermore, droplet trajectory crossings can be studied, in order to

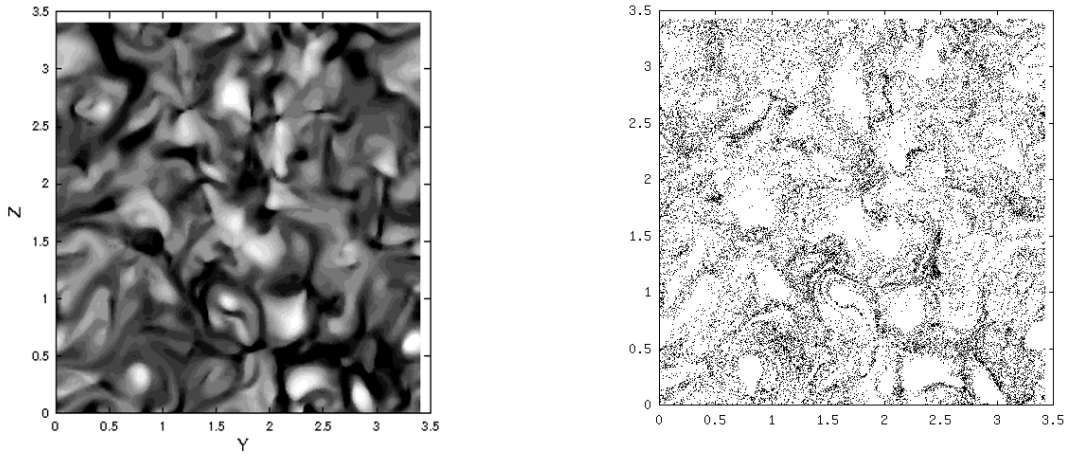

Figure 43: Eulerian-Lagrangian comparisons in the plane $(y-z)$ at $x = 1.75$ for low inertia droplets, St= 0.17: (left) Eulerian multi-fluid number density, (left) Lagrangian droplet positions.

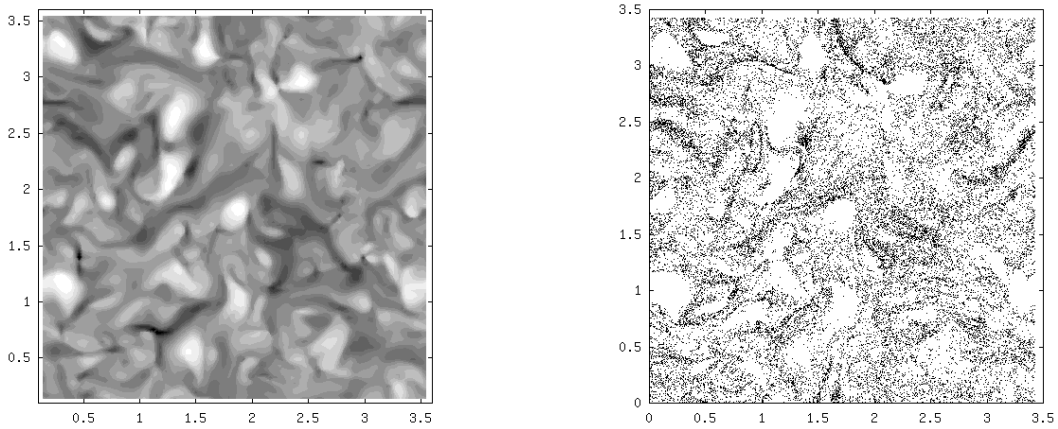

Figure 44: Eulerian-Lagrangian comparisons in the plane $(x-y)$ at $z = 1.75$ for low inertia droplets, St= 0.17: (left) Eulerian multi-fluid number density, (left) Lagrangian droplet positions.

provide a Stokes criteria to foresee their formation. This study could also assess the interest of Eulerian method describing out of equilibrium velocity distribution, [50, 82, 51].

7 Conclusion and Directions

In this contribution we have tried to provide a global picture about the status of Eulerian multi-fluid models for the description of polydisperse evaporating sprays, an important issue as far as a lot of industrial applications are concerned. Its main advantage as compared to the usual two-fluid approaches is the ability to describe the dynamics, evaporation and heating conditioned by droplet size without having to cope with the difficult task of retrieving for example the size/velocity correlation from mixed global moments.

After having described the derivation of the semi-kinetic system of conservation, we have identified the underlying assumptions at the kinetic level, which are equivalent to a closure of

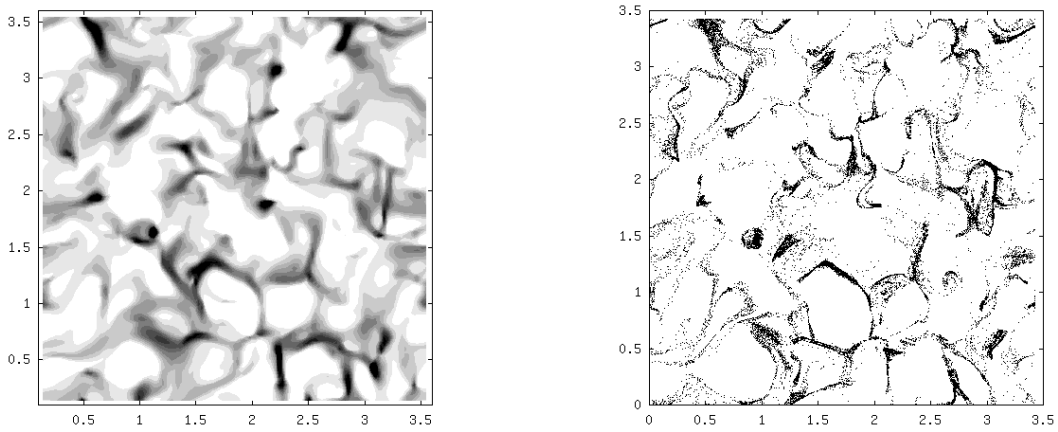

Figure 45: Eulerian-Lagrangian comparisons in the plane $(y-z)$ at $x = 1.75$ for higher inertia droplets, St= 1.05: (left) Eulerian multi-fluid number density, (left) Lagrangian droplet positions.

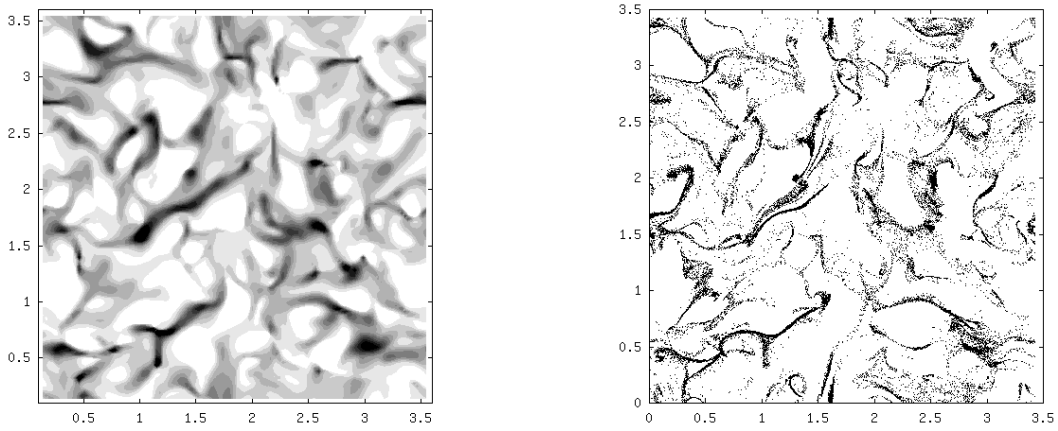

Figure 46: Eulerian-Lagrangian comparisons in the plane $(x-y)$ at $z = 1.75$ for higher inertia droplets, St= 1.05: (left) Eulerian multi-fluid number density, (left) Lagrangian droplet positions.

the system of "fluid" or macroscopic equations. As for many of the moment methods, there is a loss of information; however, we are able to characterize it and to determine the mathematical singularities stemming from such assumptions. This is a major advantage in order to design efficient and robust numerical methods in order to solve the resulting systems of conservations equations. We have also proposed a dedicated algorithm as well as a series of validations cases in order to study the accuracy and computational cost of the method, as well as its limitations in terms of droplet crossing. Even though this approach has recently been extended to higher order, the necessity to discretize the size phase space too finely because of numerical diffusion in the size discretization shows the necessity to create some new schemes in the field.

Thus, in Chapter 4, we have presented natural extensions of the original method based on high order moment methods and shown how its usual limitations can be overcome. Such a direction of research is currently very active and will probably lead to interesting new tools; however, as far as nanoparticles are concerned, only the new tools devoted to the size phase

space will be useful since most of the time, the particles will not have sufficient inertia to initiate particle crossing.

Another way around is to use the recently developed direct quadrature method of moments (DQMOM) [88] to treat Williams equation in a Eulerian framework. As its name implies, DQMOM is a moment method that closes the non-linear terms using weighted quadrature points (abscissas) in phase space. The method distinguishes itself from other quadrature methods (e.g., QMOM [28, 29]) by solving transport equations for the weights and abscissas directly (instead of transport equations for the moments). We have recently compared the two approaches on several test cases and the advantages and drawbacks of both approaches are analyzed in [32]. Where the multi-fluid experiences some numerical diffusion in the size phase space, the principle of the DQMOM allows to avoid such a problem. However, the question of droplet evaporation and the associated flux of disappearing droplets is difficult to accurately tackle in the framework of moment methods, whereas it is an easy task for the multi-fluid. We then believe that one way to really improve the capability of the actual methods would be to use the proposes new multi-fluid multi-moment method which combines the flexibility of multi-fluid models to the efficiency of DQMOM methods.

Finally, we have presented another set of validation through comparisons with experimental measurements obtained with coupled Laser diagnostics on a dedicated well-controlled configuration of an acoustically pulsated free jet with polydisperse spray injection in Chapter 5. To our knowledge, this is the first time such comparisons have been conducted.

One of the key issues in developing a new model for applications such as two-phase combustion, as well as the associated numerical methods and algorithm is its capabilities in terms of accuracy and high performance computing in order to tackle complex configurations. The last chapter has shown that we can perform "Computational Multi-fluid Dynamics", that it leads to a Eulerian description which suffers from very reasonable numerical diffusion and provides numerical solution very close to the solution obtained with a Lagrangian solver. Besides, the scalability of the algorithms is such that it leads to an efficiency of almost one so that problems which are three-dimensional in space and one-dimensional in size can be resolved within a day of computation. Such results allow to envision that such a method has a lot of potential for mode complex applications in order to better resolve the complex physics of polydisperse evaporating sprays in turbulent gaseous flow fields.

These results have initiated new directions of research among which three main directions are currently under investigation. The first one is the extension of the presented results to the two-way coupling with the related difficulties, especially in the configuration where there exists some zone of high droplet concentrations. Besides, in terms of modeling and numerical methods, it is very important to extend the capability of the code to LES. Two stumbling blocks have to be overcome in order to obtain an efficient code, the first one is related to the detailed modeling of the influence of the small unresolved scales and the derivation of the related semi-kinetic model and multi-fluid model, the second one being the design of a new numerical scheme and related algorithm which allows to reach the same level of accuracy and optimization as the one presented in these Notes; the second direction is related to the design of a new experimental configuration and the related diagnostics in order to be able to validate the models and methods. These directions are actual hard scientific challenges.

8 Ackowledgements

The present research was done thanks to a Young Investigator Award from the French Ministry of Research (New Interfaces of Mathematics - M. Massot, 2003-2006), to an ANR (National Scientific Research Agency - France) Young Investigator Award (ANR-05-JCJC-0013, M. Massot,

2006-2009) and to the support of European Commission through the project "Towards Innovative Methods for Combustion Prediction in Aeronautic Engines" (TIMECOP-AE, project N : AST5-CT-2006-030828). The authors also acknowledge the support from IDRIS-CNRS (Institut de Developpement et de Ressources en Informatique Scientifique, Centre National de la Recherche Scientifique) where some of the computations were performed. The authors acknowledge support from two scientific departments of CNRS (French Center for Scientific Research): MPPU (Mathmatiques, Physique, Plante et Univers) and ST2I (Sciences et Technologies de l'Information et de l'Ingnierie), through a PEPS project entitled: "Analyse et simulation de problmes multi-chelles : applications aux plasmas froids, la combustion et aux coulements diphasiques" (F. Laurent, 2007-2008). Part of the present work, conducted during the Ph.D. Thesis of S. de Chaisemartin (Laboratory EM2C -UPR CNRS 288), was supported by a Ph.D. grant from both DGA and CNRS and has received the support of the INCA project (National Initiative for Advanced Combustion) which is gratefully acknowledged. We also acknowledge the precious help of our collaborators : R.O. Fox and J. Reveillon for the modelling and numerical simulations and D. Durox, C. Lacour for the experimental part of the studies. Part of the material was also achieved during the Summer Program 2008 thanks to the support from the Center for Turbulence Research at Stanford University and we would like to thank Prof. P. Moin and Prof. H. Pitsch for their hospitality.

References

[1] J. Hylkema. *Modélisation cinétique et simulation numérique d'un brouillard dense de gouttelettes. Application aux propulseurs à poudre.* PhD thesis, ENSAE, 1999.

[2] J. Hylkema and P. Villedieu. A random particle method to simulate coalescence phenomena in dense liquid sprays. In *Lecture Notes in Physics*, volume 515, pages 488–493, Arcachon, France, 1998. Proc. 16th Int. Conf. on Num. Meth. in Fluid Dyn.

[3] Y. Tsuji, T. Tanaka, and S. Yonemura. Cluster patterns in circulating fluidized beds predicted by numerical simulation (discrete particle versus two-fluid models). *Powder Technology*, 95:254–264, 1998.

[4] A. Bracco, P. H. Chavanis, A. Provenzale, and A. Spiegel. Particle aggregation in a turbulent keplerian flow. *Phys. Fluids*, 11:2280–2286, 1999.

[5] P. H. Chavanis. Trapping of dust by coherent vortices in the solar nebula. *Astron. Astrophys.*, 356:1089–1111, 2000.

[6] D. Ramkrishna and A. G. Fredrickson. *Population Balances: Theory and Applications to Particulate Systems in Engineering.* Academic Press, 2000.

[7] R. J. Hall, M. D. Smooke, and M. B. Colket. Predictions of soot dynamics in opposed jet diffusion flames, a tribute to irvin glassman. In *Physical and Chemical Aspects of Combustion*, chapter 8, pages 189–230. Gordon and Breach Science Publishers, 1997.

[8] A. Zucca, D. L. Marchisio, A. A. Barresi, and R. O. Fox. Implementation of the population balance equation in CFD codes for modelling soot formation in turbulent flames. *Chemical Engineering Science*, 61, 2006.

[9] E. Aulisa, S. Manservisi, R. Scardovelli, and S. Zaleski. A geometrical area-preserving volume-of-fluid method. *J. Comput. Phys.*, 192:355–364, 2003.

[10] M. Herrmann. A Eulerian level set/vortex sheet method for two-phase interface dynamics. *J. Comput. Phys.*, 203(2):539–571, 2005.

[11] C. Josserand, L. Lemoyne, R. Troeger, and S. Zaleski. Droplet impact on a dry surface: triggering the splash with a small obstacle. *J. Fluid Mech.*, 524:47–56, 2005.

[12] S. Tanguy and A. Berlemont. Development of a level set method for interface tracking: application to droplet collisions. *Int. J. Multiphase Flow*, 31(9):1015–1035, 2005.

[13] F. A. Williams. Spray combustion and atomization. *Phys. Fluids*, 1:541–545, 1958.

[14] F. A. Williams. *Combustion Theory (Combustion Science and Engineering Series)*. ed F A Williams (Reading, MA: Addison-Wesley), 1985.

[15] R. O. Fox. Introduction and fundamentals of modeling approaches for polydisperse multiphase flows. In *Computational Models for Turbulent Multiphase Reacting Flows*, volume 492 of *CISM Courses and Lectures*, pages 1–40. SpringerWienNewYork, Vienna, 2007. Editors D.L. Marchisio and R. O. Fox, Udine, July 2006.

[16] S. K. Friedlander. *Smoke, Dust, and Haze, Fundamental of Aerosol Dynamics*. Topics in Chemical Engineering. Oxford University Press, second edition, 2000.

[17] C. Cercignani, R. Illner, and M. Pulvirenti. *The mathematical theory of dilute gases*. Springer-Verlag, New York, 1994.

[18] J. K. Dukowicz. A particle-fluid numerical model for liquid sprays. *J. Comput. Phys.*, 35(2):229–253, 1980.

[19] P. J. O'Rourke. *Collective drop effects on vaporizing liquid sprays*. PhD thesis, Princeton University, 1981.

[20] A. A. Amsden, P. J. O'Rourke, and T. D. Butler. Kiva II, a computer program for chemically reactive flows with sprays. Technical Report LA-11560-MS, Report Los Alamos National Laboratory, Los Alamos, New Mexico, 1989.

[21] P.-A. Raviart and L. Sainsaulieu. A nonconservative hyperbolic system modeling spray dynamics. I. Solution of the Riemann problem. *Math. Models Methods Appl. Sci.*, 5(3):297–333, 1995.

[22] K. Domelevo and L. Sainsaulieu. A numerical method for the computation of the dispersion of a cloud of particles by a turbulent gas flow field. *J. Comput. Phys.*, 133(2):256–278, 1997.

[23] F. Laurent and M. Massot. Multi-fluid modeling of laminar poly-dispersed spray flames: origin, assumptions and comparison of sectional and sampling methods. *Comb. Theory and Modelling*, 5:537–572, 2001.

[24] M. Rüger, S. Hohmann, M. Sommerfeld, and G. Kohnen. Euler/Lagrange calculations of turbulent sprays: the effect of droplet collisions and coalescence. *Atomization and Sprays*, 10(1):47–81, 2000.

[25] G. A. Bird. *Molecular gas dynamics and the direct simulation of gas flows*, volume 42 of *Oxford Engineering Science Series*. Oxford University Press, 1994.

[26] Marta Garca Martinez. *Development and validation of the Euler-Lagrange formulation on a parallel and unstructured solver for large-eddy simulation.* PhD thesis, Institut National Polytechnique de Toulouse, France, 2009.

[27] D. L. Wright, R. McGraw, and D. E. Rosner. Bivariate extension of the quadrature method of moments for modeling simultaneous coagulation and sintering of particle populations. *J. of Colloid and Interface Sci.*, 236:242–251, 2001.

[28] R. McGraw. Description of aerosol dynamics by the quadrature method of moments. *Aerosol Science and Technology*, 27:255–265, 1997.

[29] D. L. Marchisio, R. D. Vigil, and R. O. Fox. Quadrature method of moments for aggregation-breakage processes. *J. of Colloid and Interface Sci.*, 258(2):322–334, 2003.

[30] J.B. Greenberg, I. Silverman, and Y. Tambour. On the origin of spray sectional conservation equations. *Combustion and Flame*, 93:90–96, 1993.

[31] C. McEnally, A. Shaffer, M. B. Long, L. Pfefferle, M.D. Smooke, M.B. Colket, and R.J. Hall. Computational and experimental study of soot formation in a coflow laminar ethylene diffusion flame. *Proceedings of the Combustion Institute*, 27:664–672, 1998.

[32] R. O. Fox, F. Laurent, and M. Massot. Numerical simulation of spray coalescence in an Eulerian framework: direct quadrature method of moments and multi-fluid method. *J. Comput. Phys.*, 227(6):3058–3088, 2008.

[33] D. A. Drew and S. L. Passman. Theory of multicomponent fluids. *Applied Mathematical Sciences*, 135, 1999.

[34] J. Reveillon, C. Péra, and M. Massot. Lagrangian/Eulerian analysis of the dispersion of vaporizing polydispersed sprays in turbulent flows. Proceedings of the Summer Program 2002, Center for Turbulence Research, Stanford University, 2002.

[35] Henning Struchtrup. *Macroscopic transport equations for rarefied gas flows.* Interaction of Mechanics and Mathematics. Springer, Berlin, 2005. Approximation methods in kinetic theory.

[36] M. Massot and P. Villedieu. Modélisation multi-fluide eulérienne pour la simulation de brouillards denses polydispersés. *C. R. Acad. Sci. Paris Sér. I Math.*, 332(9):869–874, 2001.

[37] F. Laurent, M. Massot, and P. Villedieu. Eulerian multi-fluid modeling for the numerical simulation of coalescence in polydisperse dense liquid sprays. *J. Comput. Phys.*, 194(2):505–543, 2004.

[38] G. Dufour, M. Massot, and P. Villedieu. Étude d'un modèle de fragmentation secondaire pour les brouillards de gouttelettes. *C. R. Math. Acad. Sci. Paris*, 336(5):447–452, 2003.

[39] G. Dufour. *Modélisation multi-fluide eulérienne pour les écoulements diphasiques à inclusions dispersées.* PhD thesis, Université Paul Sabatier Toulouse III, 2005.

[40] M. Massot, R. Knikker, C. Péra, and J. Reveillon. Lagrangian/Eulerian analysis of the dispersion of evaporating sprays in non-homogeneous turbulent flows. In *International Conference on Multiphase Flows, Japan*, 2004.

[41] M. Massot. Eulerian multi-fluid models for polydisperse evaporating sprays. In *Multiphase reacting flows: modelling and simulation*, volume 492 of *CISM Courses and Lectures*, pages 79–123. SpringerWienNewYork, Vienna, 2007. Editors D.L. Marchisio and R. O. Fox, Udine, July 2006.

[42] S. de Chaisemartin, F. Laurent, M. Massot, and J. Reveillon. Evaluation of Eulerian multi-fluid versus Lagrangian methods for the ejection of polydisperse evaporating sprays by vortices. *J. Comput. Phys.*, 2009. Submitted, available on HAL http://hal.archives-ouvertes.fr/hal-00169721/.

[43] Stéphane de Chaisemartin. *Eulerian models and numerical simulation of the turbulent dispersion of polydisperse evaporating sprays.* PhD thesis, Ecole Centrale Paris, France, 2009.

[44] F. Laurent. *Modélisation mathématique et numérique de la combustion de brouillards de gouttes polydispersés.* PhD thesis, Université Claude Bernard, Lyon 1, 2002.

[45] Ya. B. Zel′dovich. Gravitational instability : an approximate theory for large density perturbations. *Astron. Astrophys.*, 5:84–89, 1970.

[46] F. Bouchut. On zero pressure gas dynamics. In *Advances in kinetic theory and computing*, volume 22 of *Ser. Adv. Math. Appl. Sci.*, pages 171–190. World Sci. Publ., River Edge, NJ, 1994.

[47] F. Laurent. Numerical analysis of Eulerian multi-fluid models in the context of kinetic formulations for dilute evaporating sprays. *M2AN Math. Model. Numer. Anal.*, 40(3):431–468, 2006.

[48] F. Laurent, V. Santoro, M. Noskov, A. Gomez, M.D. Smooke, and M. Massot. Accurate treatment of size distribution effects in polydispersed spray diffusion flames: multi-fluid modeling, computations and experiments. *Combust. Theory and Modelling*, 8:385–412, 2004.

[49] Damien Kah. *Prise en compte des aspects polydispersés dans le contexte d'une approche couplée Eulérienne-Lagrangienne pour la modélisation d'un jet de carburant dans les moteurs à combustion interne (Modelling polydispersity in the numerical simulation of fuel jets in internal combustion engines through a coupled Euler-Lagrange solver).* PhD thesis, Ecole Centrale Paris, France, 2010.

[50] S. de Chaisemartin, L. Freret, D. Kah, F. Laurent, R. O. Fox, J. Reveillon, and M. Massot. Eulerian models for turbulent spray combustion with polydispersity and droplet crossing : modeling and validation. Proceedings of the Summer Program 2008, Center for Turbulence Research, Stanford University, 2009.

[51] L. Freret, S. de Chaisemartin, F. Laurent, P. Vedula, R. O. Fox, O. Thomine, J. Reveillon, and M. Massot. Eulerian moment models for polydisperse weakly collisional sprays : model and validation. Proceedings of the Summer Program 2008, Center for Turbulence Research, Stanford University, 2009.

[52] S. de Chaisemartin, L. Fréret, D. Kah, F. Laurent, R.O. Fox, J. Reveillon, and M. Massot. Eulerian models for turbulent spray combustion with polydispersity and droplet crossing. *Comptes Rendus Mécanique*, In Press:–, 2009. Special Issue 'Combustion for Aerospace Propulsion'.

[53] L. Fréret, C. Lacour, S. de Chaisemartin, S. Ducruix, D. Durox, F. Laurent, and M. Massot. Pulsated free jets with polydisperse spray injection: Experiments and numerical simulations. *Proceedings of the Combustion Institute*, 32(2):2215 – 2222, 2009.

[54] B. Abramzon and W. A. Sirignano. Droplet vaporization model for spray combustion calculations. *Int. J. Heat Mass Transfer*, 32(9):1605–1618, 1989.

[55] P. Villedieu and J. Hylkema. Une méthode particulaire aléatoire reposant sur une équation cinétique pour la simulation numérique des sprays denses de gouttelettes liquides. *C. R. Acad. Sci. Paris Sér. I Math.*, 325(3):323–328, 1997.

[56] P. R. Brazier-Smith, S. G. Jennings, and J. Latham. The interaction falling water drops : coalescence. *Proceedings of the Royal Society*, 326:393–408, 1972.

[57] N. Ashgriz and J. Y. Poo. Coalescence and separation in binary collisions of liquid droplets. *J. Fluid Mech.*, 221:183–204, 1990.

[58] P. Achim. *Simulation de collisions, coalescence et rupture de gouttes par une approche lagrangienne: application aux moteurs à propergol solide.* PhD thesis, Faculté des Sciences de l'Université de Rouen, 1999.

[59] R.I. Nigmatulin. *Dynamics of multiphase media.* Hemisphere, Washington D.C., 1991.

[60] L.-P. Hsiang and G. M. Faeth. Drop properties after secondary breakup. *Int. J. Multiphase Flow*, 19(5):721–735, 1993.

[61] P. J. O'Rourke and A. Amsden. The tab method for numerical calculation of spray droplet breakup. Technical Report 87545, Los Alamos National Laboratory, Los Alamos, New Mexico, 1987.

[62] K. L. Wert. A rationally-based correlation of mean fragment size for drop secondary breakup. *Int. J. Multiphase Flow*, 21(6):1063–1071, 1995.

[63] Andre Kaufmann. *Vers la simulation des grandes échelles en fomulation Euler-Euler des écoulements réactifs diphasiques.* PhD thesis, Institut National Polytechnique de Toulouse, France, 2004.

[64] Riber Eleonor. *Développement de la méthode de simulation aux grandes échelles pour les écoulements diphasiques turbulents.* PhD thesis, Institut National Polytechnique de Toulouse, France, 2007.

[65] Matthieu Boileau. *Simulation aux grandes échelles de l'allumage diphasique des foyers aéronautiques.* PhD thesis, Institut National Polytechnique de Toulouse, France, 2007.

[66] M. W. Reeks. On a kinetic equation for the transport of particles in turbulent flows. *Phys. Fluids*, 3:446–456, 1991.

[67] J. Reveillon, C. Péra, M. Massot, and R. Knikker. Eulerian analysis of the dispersion of evaporating polydispersed sprays in a statistically stationary turbulent flow. *Journal of Turbulence*, 5(1):1–27, 2004.

[68] S. B. Pope. *Turbulent flows.* Cambridge University, 2000.

[69] O. A. Druzhinin and S. E. Elghobashi. A Lagrangian-Eulerian mapping solver for direct numerical simulation of bubble-laden turbulent shear flows using the two-fluid formulation. *J. Comput. Phys.*, 154:174–196, 1999.

[70] F. Bouchut, S. Jin, and X. Li. Numerical approximations of pressureless and isothermal gas dynamics. *SIAM J. Numer. Anal.*, 41(1):135–158, 2003.

[71] R. J. LeVeque. *Finite volume methods for hyperbolic problems*. Cambridge Texts in Applied Mathematics. Cambridge University Press, Cambridge, 2002.

[72] A. N. Volkov, Yu. M. Tsirkunov, and B. Oesterle. Numerical simulation of a supersonic gas-solid flow over a blunt body : The role of inter-particle collisions and two-way coupling effects. *Int. J. Multiphase Flow*, 31(12):1244–1275, 2005.

[73] P.-E. Jabin. Various levels of models for aerosols. *Math. Models Methods Appl. Sci.*, 12(7):903–919, 2002. Special issue on kinetic theory.

[74] G. Strang. On the construction and comparison of difference schemes. *SIAM J. Num. Anal.*, 5:507–517, 1968.

[75] A. V. Bobylev and T. Ohwada. The error of the splitting scheme for solving evolutionary equations. *Applied Mathematics Letters*, 14:45–48, 2001.

[76] S. Descombes and M. Massot. Operator splitting for nonlinear reaction-diffusion systems with an entropic structure: singular perturbation and order reduction. *Numer. Math.*, 97(4):667–698, 2004.

[77] S. de Chaisemartin, F. Laurent, L. Fréret, M. Massot, A-L. Birbaud, C. Lacour, S. Ducruix, and D. Durox. Pulsated free jets with spray injection : Eulerian Multi-Fluid modelling and simulation versus experimental measurements. In *International Conference on Multiphase Flows, Leipzig*, 2007.

[78] E. Hairer and G. Wanner. *Solving ordinary differential equations. II*, volume 14 of *Springer Series in Computational Mathematics*. Springer-Verlag, Berlin, second edition, 1996. Stiff and differential-algebraic problems.

[79] S. de Chaisemartin, F. Laurent, M. Massot, and J. Reveillon. LES multi-fluid formulation and applied mathematical issues. Technical report, CRSA-EM2C, Deliverable 1.3.1a, European Project TIMECOP-AE, 2006.

[80] M. Massot, F. Laurent, D. Kah, and S. de Chaisemartin. A robust moment method for evaluation of the disappearance rate of evaporating sprays. *SIAM J. Appl. Math.*, 2008. submitted for publication.

[81] S. de Chaisemartin. *Modèles eulériens et simulation numérique de la dispersion turbulente de brouillards qui s'évaporent*. PhD thesis, Ecole Centrale Paris, 2009.

[82] R. O. Fox. A quadrature-based third-order moment method for dilute gas-particle flow. *J. Comput. Phys.*, 227(12):6313–6350, 2008.

[83] D. L. Wright. Numerical advection of moments of the particle size distribution in Eulerian models. *Journal of Aerosol Science*, 38(3):352 – 369, 2007.

[84] H. Dette and W. J. Studden. *The theory of canonical moments with applications in statistics, probability, and analysis*. Wiley Series in Probability and Statistics: Applied Probability and Statistics. John Wiley & Sons Inc., New York, 1997. A Wiley-Interscience Publication.

[85] L. R. Mead and N. Papanicolaou. Maximum entropy in the problem of moments. *J. Math. Phys.*, 25(8):2404–2417, 1984.

[86] R. J. LeVeque. *Numerical methods for conservation laws*. Birkhäuser Verlag, Basel, second edition, 1992.

[87] R. McGraw. Numerical advection of correlated tracers: preserving particle size/composition moment sequences during transport of aerosol mixtures. *J. Phys.: Conf. Ser.*, 78(012045):5p, 2007.

[88] D. L. Marchisio and R. O. Fox. Solution of population balance equations using the direct quadrature method of moments. *Journal of Aerosol Science*, 36(1):43–73, 2005.

[89] O. Desjardins, R. O. Fox, and P. Villedieu. A quadrature-based moment method for dilute fluid-particle flows. *J. Comput. Phys.*, 227(12):6313–6350, 2008.

[90] S. C. Crow and F. H. Champagne. Orderly structure in jet turbulence. *J.Fluid Mech*, 48:547, 1971.

[91] A. L. Birbaud, D. Durox, S. Ducruix, and S. Candel. Dynamics of free jets submitted to upstream acoustic modulations. *Phys. Fluids*, 19(1), 2007.

[92] C. Pichard, D. Durox, and S. Ducruix. Effects of acoustic modulations on a spray flame. In *20th ILASS, Annual Meeting of the Institute of Liquid Atomization and Spray System*, Orléans, France, 2005.

[93] G. König, K. Anders, and A. Frohn. A new light scattering technique to measure the diameter of periodically generated moving droplets. *I.Aerosol Sci*, 17:157–167, 1986.

[94] A. R. Glover, S. M. Skippon, and R. D. Boyle. Interferometric laser imaging for droplet sizing: a method for droplet size measurement in sparse spray system. *Appl.Opt*, 34:8409–8421, 1995.

[95] S. de Chaisemartin, F. Laurent, M. Massot, and J. Reveillon. Evaluation of Eulerian Multi-Fluid versus Lagrangian methods for the ejection of polydisperse evaporating sprays by vortices. In *International Conference on Multiphase Flows, Leipzig*, 2007.

[96] A. J. Chorin. Numerical solution of the Navier-Stokes equations. *Math. Comp.*, 22:745–762, 1968.

[97] R. Temam. Une méthode d'approximation de la solution des équations de Navier-Stokes. *Bull. Soc. Math. France*, 96:115–152, 1968.

[98] F. Nicoud. Conservative high-order finite-difference schemes for low-mach number flows. *J. Comp. Phys.*, 158:71–97, 2000.

[99] A. A. Wray. Minimal storage time-advancement schemes for spectral methods. Technical report, Center for Turbulence Research, Stanford University, 1990.

[100] S. K. Lele. Compact finite difference schemes with spectral like resolution. *J. Comput. Phys.*, 103:16–42, 1992.

[101] T. Poinsot and S. K. Lele. Boundary conditions for direct simulations of compressible viscous flows. *J. Comput. Phys.*, 101(1):104–129, 1992.

[102] F. Mashayek. Direct numerical simulations of evaporating droplet dispersion in forced low mach number turbulence. *Int. J. Heat Mass Transfer*, 41:2601–2617, 1998.

[103] J. Reveillon and L. Vervisch. Analysis of weakly turbulent diluted-spray flames and spray combustion regimes. *J. Fluid Mech.*, 537:317–347, 2005.

[104] R. S. Miller and J. Bellan. Direct numerical simulation and subgrid analysis of a transitional droplet laden mixing layer. *Phys. Fluid*, 12(3):650–671, 2000.

[105] B. Lecordier, D. Demare, L. Vervisch, J. Reveillon, and M. Trinite. Estimation of the accuracy of piv treatments for turbulent flow studies by direct numerical simulation of multiphase flow. *Meas. Sci. Technol.*, 12:1382–1391, 2001.

[106] J. Reveillon and F.-X. Demoulin. Effects of the preferential segregation of droplets on evaporation and turbulent mixing. *J. Fluid Mech.*, 583:273–302, 2007.

[107] M. Klein, A. Sadiki, and J. Janicka. A digital filter based generation of inflow data for spatially developing direct numerical or large eddy simulations. *J. Comput. Phys.*, 186:652–665, 2003.

[108] H. Meftah. *Simulation numérique directe d'un spray en évaporation : Analyse et modélisation du mélange turbulent et des transferts thermiques.* PhD thesis, INSA de Rouen, 2008.

[109] G. Dufour and P. Villedieu. A second-order multi-fluid model for evaporating sprays. *M2AN Math. Model. Numer. Anal.*, 39(5):931–963, 2005.